technische universität
dortmund

Broadband Excitation and Quantum Control of Single Electron-Spins of Diamond NV-Centers

Dissertation

presented to the Faculty of Physics of the
TU Dortmund University, Germany
in partial fulfilment of the requirements for the degree of

Doctor rerum naturalium

by

Ingo Oliver Niemeyer

– April 2013 –

Accepted by the Faculty of Physics of the TU Dortmund University, Germany.

Day of the oral examination: 21.06.2013

Examination board:
Prof. Dr. Dieter Suter (first referee)
Prof. Dr. Fedor Jelezko (second referee)
Prof. Dr. Götz S. Uhrig
Dr. Catalin Gainaru

CONTENTS

1 INTRODUCTION

1.1 QUANTUM COMPUTATION AND DIAMOND

In 1982 Richard Feynman [1] proposed an idea of a computer based on quantum systems which takes advantage of quantum phenomena to perform simulations of other quantum systems. While the bits of a classical computer can take one of two states 0 or 1, the bits of a quantum computer, called qubits, can take arbitrary superpositions of the eigenstates $|0\rangle$ and $|1\rangle$. Moreover a qubit of a quantum register can be entangled with the other qubits. This entanglement can be regarded as a global superposition among the eigenstates of the participating qubits. It is expected that for some mathematical issues quantum algorithms exploiting quantum mechanics will be faster than their classical counterparts. For example for Grover's algorithm, which is meant for searching in unsorted databases, a quadratic speedup is expected. Other quantum algorithms are expected to be exponentially faster than their classical counterparts. The development of quantum computers is a very ambitious target. To this end, the most challenging task would be the coherent control of an ensemble of qubits and the measurement of its quantum states, meaning the extraction of quantum information from the microscopic quantum world into the macroscopic classical world with a high fidelity. By today, a lot of effort has been spent on improving the understanding of quantum mechanical effects and the development of possible quantum processor architectures. That a quantum system can be used for computation tasks has been shown in 2001 by a group at IBM [2] where 15 was factorized into $5 \cdot 3$ by implementing Shor's quantum factoring algorithm. In this work, molecules in solution with seven distinguishable spins (qubits) were excited and readout by the method of nuclear magnetic resonance (NMR). In 2012, the factorization of 15 was repeated by using superconducting circuits [3], and the factorization of 21 was achieved [4].

A set of requirements, which has to be fulfilled by a quantum system to be used as a quantum computer, was defined by DiVincenzo [5]. But so far, no system has been found which fulfills all requirements. It fact, it arises that there will not be *that* perfect system but rather hybrid systems combining the advantages of different systems in one [6]. For example the Nitrogen-Vacancy (NV) centers in diamond can be regarded as a natural semi-hybrid system. A NV-center possesses an electron spin, which can be excited conveniently by irradiation of oscillating electromagnetic fields in a microwave range,

and it is optically active. Since the fluorescence emission depends on the electron spin state, an optical detection of the electron paramagnetic resonance signal of a single NV-center is possible. This makes NV defect centers in diamond promising candidates for quantum information processing [7]. By isotopical engineering it is possible to create ^{12}C enriched diamond samples which show very long transverse coherence times T_2^* for solid state quantum systems. T_2^* of the ^{12}C enriched sample used in this thesis was > 200 μs. NV-centers can occur naturally in diamonds but can also be implanted artificially by irradiation with nitrogen ions [8, 9]. It was shown that laser induced desorption occurs by irradiation with a short-pulse ultraviolet laser below the threshold for ablation which allows smooth etching of the diamond surface [10] and could be used to create structures on the diamonds surface after the implantation and creation of NV-centers. Due to couplings to other NV-centers or impurities like ^{13}C's and ^{14}N's multipartite hybrid quantum registers can be realized in diamond [11, 12, 13].

Besides the application in the field of quantum computation, further schemes exist to use NV-centers for applications like magnetometry [14, 15, 16], electrometry [17] and for spatial scanning applications with nanometer resolution [18]. The recently measured temperature dependence of the zero-field splitting constant [19, 20, 21] indicates that it may also be used as a nanoscale temperature sensor. Overall, NV-centers in diamond provide powerful test-grounds for examining quantum protocols which might be used in quantum computation as well as for improving the understanding of solid state physics and quantum mechanics in general.

1.2 THESIS OVERVIEW

This thesis is subdivided into the following chapters. In chapter 2 I give an introduction to NV-centers in diamond. This chapter contains the presentation of the NV-center in the diamond lattice, a short overview of the samples used in this thesis, a simplified model of the electronic level structure, an introduction to the spin dependent fluorescence emission of the NV-center, an introduction to the NV's electronic ground state spin Hamiltonian and the electron paramagnetic resonance spectrum which can be detected optically. It is also discussed how to manipulate single as well as double-quantum transitions, the issue of relaxation of the electron spin coherence is broached and sequences to extend the transverse coherence time are introduced.

In chapter 3 the electronic and optical setups, which I built up during the work of my thesis, are introduced. Chapter 4 presents the measurements of a broadband excitation sequence by chirped microwave pulses which we introduced to the NV-center community. Part of this

chapter was published in Ref. [22]. Chapter 5 shows the results of measurements which were aimed to extend the transverse coherence time of single as well as double-quantum coherences. The first part of chapter 5 was published in Ref. [23]. In chapter 6, I present measurements of two-pulse electron spin echo envelope modulations of single NV-centers. It is shown that the modulations are also observable by the application of CPMG sequences. Ramsey measurements indicate that the modulations are attributed to hyperfine coupled ^{13}C's which were in the close proximity to the NV-centers. In chapter 7, I present analyses which show that the nuclear spin of the ^{14}N atom of the NV-center can be controlled via the NV electron spin by applying a strongly modulating pulse.

2 NITROGEN-VACANCY CENTER IN DIAMOND

Diamond is a condensed phase of carbon. Its lattice is formed by strong covalent bonds between carbon atoms, which leads to the highest hardness among natural crystals and makes diamond chemically inert. A pure diamond is optically transparent and colorless, but it becomes colored by defects or contamination with impurities substituting carbon atoms of the lattice. Among various kinds of color centers, the nitrogen-vacancy (NV-) center has drawn much attentions in the quantum information community due to its unique features, such as spin-dependent fluorescence and optical stability. This chapter gives an introduction to basic optical and spin properties of NV-centers.

2.1 DIAMOND AND THE NV-CENTER

Diamond is one possible solid state in which pure carbon can occur in nature. Other forms are for example graphite, fullerenes etc. In the diamond lattice the carbon atoms are covalently bonded by sp^3 hybrid-orbitals with tetrahedral geometry. Diamond is a naturally occurring material with the largest known hardness. The hardness of a diamond crystal is anisotropic which makes it possible to use diamonds for grinding diamonds. Diamond's ignition point in air is 700 - 800 °C. In air diamond converts to graphite at $\approx$ 700 °C in vacuum at $>$ 1700 °C. In the case of graphite the carbon atoms are bonded by sp^2 hybrid-orbitals with layers (transverse direction) of covalent bonds. In longitudinal direction the layers are connected by *Van-der-Waals* forces. Thus the hardness of graphite is more anisotropic than of diamond. Diamonds are very robust with respect to chemical reactions. Pure diamonds are optically transparent and colorless. Due to defects in the lattice and impurity atoms, diamonds can gain colors. Among all known diamond impurities the NV defect center is one with the most interesting optical and electronic properties. An introduction to the optical and electronic properties of the diamond NV-center is given in the following.

2.1.1 *Crystal Structure and Types*

The lattice constant of diamond is 0.357 nm. Eight atoms are located in a unit cell. The distance between adjacent atoms is 0.154 nm. The atomic density of the diamond lattice is with an atomic packing factor of approximately 0.34 relatively small. The diamond crystal structure is face-centered cubic with a basis of two carbon atoms located along

the direction $\langle 1,1,1\rangle$ and separated by $1/4$ of the unit cell length. This is equivalent to two face-centered cubic crystal lattices which are displaced by $1/4$ of the unit cell length along the same direction $\langle 1,1,1\rangle$. Each carbon atom is covalently bonded to four adjacent carbon atoms resulting in a tetrahedral geometry. One of the most often occurring natural impurities in diamond is nitrogen. In case of the nitrogen-vacancy (NV) defect center a nitrogen atom substituting a carbon atom is coupled to an adjacent vacancy site. The NV-center is of C_{3v} symmetry. In fig. 1 a scheme of the diamond crystal with a NV-center is shown. The *gray* spheres denote carbon atoms while the red sphere shows the location of the nitrogen atom. The *green* spheres represent the four possible locations of the vacancy. The solid *black* lines indicate bonds to the next neighbors. Figure 46 in section A.1 of the appendix shows a CW-ODMR spectrum of two different orientated NV-centers.

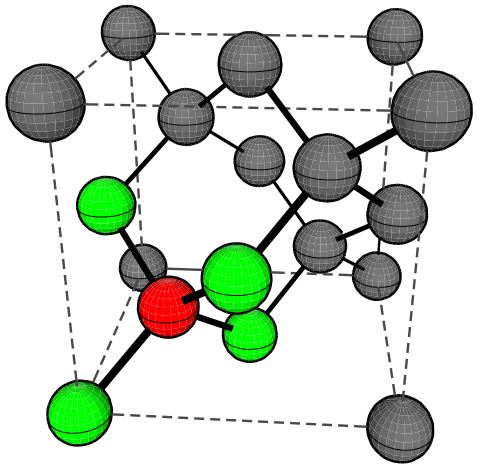

Figure 1: Nitrogen-Vacancy center and Diamond crystal structure. **Gray:** Locations of the carbon atoms. **Green:** Four possible locations of the vacancy. **Red:** Location of the nitrogen atom. The solid *black* lines indicate bonds to the next neighbors. The line thickness is varied for visual purposes and reduces for atoms farther away.

Depending on the concentration of the nitrogen impurities and the distribution in the crystal, diamonds are classified as different types. An overview of this classification is given in tab. 1 [24, 25]. For this thesis single NV-centers in artificially grown diamond crystals with low nitrogen concentrations were used. Since nitrogen was the only significant impurity in diamond, our samples were of type IIa.

2.2 SYNTHESIS METHOD AND SAMPLES

For the measurements presented in this thesis we used two different samples, both are single crystals of type IIa (cf. tab. 1). One is an artificially grown diamond with a natural abundance of ^{13}C (concentration

Type	N Content	Sub-Type	Feature	[N] in ppm
I	high	Ia	aggregates of N	< 3000
		Ib	single substitutional N	< 500
II	low	IIa	very low N content	<~ 1
		IIb	significant boron content $\rightarrow$ p-type semiconductor	<~ 1

Table 1: Classification of diamonds.

$\approx$ 1.1 %) the other is a ^{12}C enriched (concentration $\approx$ 99.995 %) artificially grown crystal. The natural abundance diamond sample had a N concentration of $<$ 5 ppb . We received this sample from our collaboration partner Prof. Fedor Jelezko from the University of Stuttgart respectively Ulm (Germany). The enriched sample was prepared by our Japanese collaboration partners Prof. Isoya Junichi from the University of Tsukuba (Japan). It was grown at 5.5 GPa and 1400 °C from Co-Ti-Cu alloy by using a temperature gradient method. As a solid carbon source, polycrystalline diamond plates synthesized by chemical vapor deposition (CVD) utilizing ^{12}C enriched methane were used [26]. Secondary ion mass spectrometry (SIMS) analysis has shown that typically a ^{12}C concentration of 99.995 % in the grown crystals was achieved. The crystal was irradiated at room temperature with 2 MeV electrons and a total flux intensity of $10^{11}/cm^2$. Subsequently it was annealed at 1000 °C for 2 hours in vacuum.

2.3 SPIN STATE DEPENDENT FLUORESCENCE

Electron paramagnetic resonance measurements showed that the electronic ground state of the NV-center is a triplet state with an electron spin $S = 1$. As nitrogen has 5 valence electrons, but an electron spin of $S = 1$ requires an even number of electrons, it is assumed that NV-centers are negatively charged[27]. Adjacent impurities like other nitrogen atoms are supposed to donate the additional electron. The negative charge state is the most likely charge state (probability $\approx$ 70 %) of the NV-center but the neutral charge state does also occur (probability $\approx$ 30 %) [28, 29]. The conversion between the different charge states is induced by optical excitation. In case of the neutral NV-center the total number of electrons is 5 and the electron-spin is S $= 1/2$. The charge state of the nitrogen defect affects also the photon-emission spectrum of the center as shown in fig. 2. The blue curve shows the photon emission of the neutrally charged NV-center and the red curve those of the negatively charged center. The wavelengths of the zero-phonon lines are 575 nm for the neutrally charged

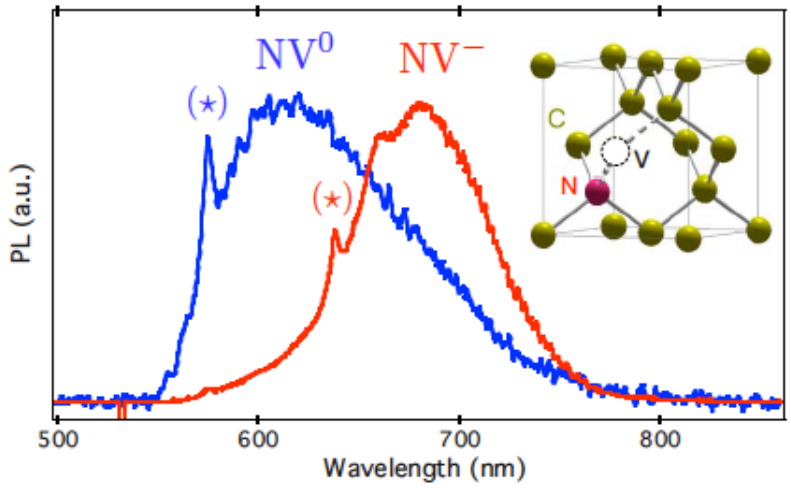

Figure 2: Emission Spectrum of NV^0 and NV^-. The *blue* curve shows the emission spectrum of the neutral and the *red* of the negatively charged NV-center. The asterisks denote the zero-phonon lines of the corresponding NV-center. The inset shows the location of the NV-center in the diamond lattice [30].

NV-center (marked by the *blue* asterisk) and 637 nm for the negatively charged center (marked by the *red* asterisk). The inset shows the NV-center in the diamond lattice. Unless otherwise mentioned, we use 'NV-center' by meaning the negatively charged defect center.

The electron ground and excited state of the NV-center are triplet states. It is assumed that the NV-center has two (newer theories predict three [31]) intermediate singlet states. Here, we will use a simplified picture and proceed with the assumption of a single intermediate singlet state. Figure 3 shows a scheme of the electronic level structure. After an optical excitation the electrons can either relax directly into the electronic ground state by photon emission, which is a spin conserving process, or indirectly by an inter-system crossing process, which is not spin conserving. By transition into the intermediate state the electrons relax via infrared photon emission [32] and phonon scattering. The probability of an inter-system crossing depends on the electron spin and is for the $|m_s = \pm 1\rangle$ spin states higher than for $|m_s = 0\rangle$. Electrons, which are in the spin state $|m_s = 0\rangle$, relax mainly due to spin conserving photon emission. Relaxation from the intermediate state to the electronic ground state is not spin conserving and occurs mainly into the $|m_s = 0\rangle$ spin state. Via this relaxation path no or at least only infrared photons, which are usually filtered out by the detection system, are emitted [33]. Since less photons will be detected when the electrons are in the spin states $|m_s = \pm 1\rangle$ (the infrared photons are not detected from the detection system), theses states are called *dark states* while $|m_s = 0\rangle$ is called *bright state*. As a result of the spin selective relaxation process a polarization of the $|m_s = 0\rangle$ spin state is achieved under optical excitation which reaches a maximum

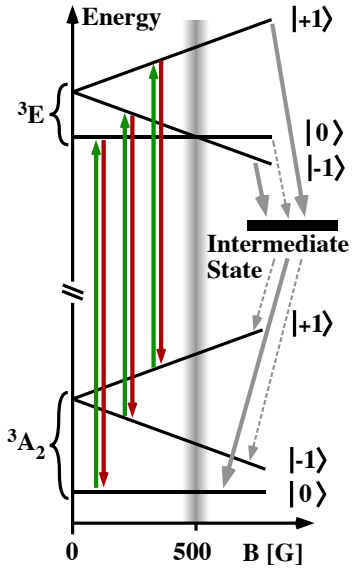

Figure 3: Electronic energy levels of NV-center (based on [35]). ${}^3A_2$ is the electronic ground and ${}^3E$ the excited state. For the sake of simplicity only one intermediate state is shown. The *green* arrows indicate an optical excitation with green laser light. The *red* arrows indicate direct relaxation via photon emission. The *gray* solid arrows indicate strong and the dotted *gray* arrows weak inter-system transitions. The *gray* vertical line at 500 G marks a level anti-crossing of the electron excited state, another anti-crossing (which is not shown here) occurs at $\approx$ 1030 G for the electronic ground state [36, 37, 35]. The lifetime for electrons trapped in the intermediate state is $\sim 150 - 450$ ns [33].

of $\approx$ 90 % [34]. Any population change by resonant excitation with microwave pulses between the $|m_s = 0\rangle \leftrightarrow |m_s = \pm 1\rangle$ spin levels can thus be detected via the photon scattering rate [7].

2.4 SPIN HAMILTONIAN

The two stable nitrogen isotopes ^{15}N and ^{14}N are known to occur in NV-centers in diamond. Because ^{15}N has a nuclear spin $I = 1/2$ and ^{14}N of $I = 1$ the corresponding NV-centers can be distinguished by their spectrum which show different number of lines due to hyperfine interaction. Since the measurements presented in this thesis were performed with ^{14}NV-centers only, ^{15}NV-centers will not be further discussed. For the sake of simplicity we abbreviate ^{14}NV by NV in the following. A theoretical analysis about the spin states of the NV electronic ground state is given in Ref. [38]. In this chapter we introduce the theoretical framework which is relevant for the description of the NV electron and the nuclear spin in this thesis.

2.4.1 *Quadrupole Interaction*

The nuclear spin of the ^{14}N in the NV-center is $I_{14N} = 1$. A nucleus with spin $I \geq 1$ is exposed to electric field gradients, generated by surrounding electrons and nuclei, which interact with the charge distribution of the nucleus and partially lifts its spin level degeneracy. This interaction is called *nuclear quadrupole interaction* and is independent of the external magnetic field. The relevant nuclear quadrupole interaction of the ^{14}N nuclear spin of the NV-center is given by:

$$H_{nq} = P_0 \left[I_z^2 - \frac{1}{3} I (I+1)^2 \right] ,$$

with $P_0 = -5.04$ MHz.

2.4.2 *Zero Field Splitting*

For a system of electron spin $S \geq 1$, the individual electrons produce a permanent internal field which partly removes the spin degeneracy. This energy splitting is independent of any external magnetic field and is called *zero-field-splitting*. Due to the rotational symmetry of the NV-center the Hamiltonian of the zero-field splitting is given by:

$$H_{zf} = D \left[S_z^2 - \frac{1}{3} S (S+1) \right] ,$$

with $D = 2.872$ GHz [39].

2.4.3 *Hyperfine Interaction*

A *hyperfine interaction* describes the coupling between an electron spin and a nuclear spin. It consists of two coupling components, an orientation dependent (*anisotropic*) part which is usually given by a dipolar coupling and an orientation independent (*isotropic)* part which is given by the Fermi contact interaction. The hyperfine interaction can be expressed in operator form which includes the isotropic and anisotropic parts. It is given by:

$$H_{hf} = H_{hf,\,aniso} + H_{hf,\,iso} = \mathbf{SAI} \, . \tag{1}$$

The hyperfine coupling tensor $\mathbf{A}$ is given by:

$$\mathbf{A} = \begin{pmatrix} A_{xx} & A_{xy} & A_{xz} \\ A_{yx} & A_{yy} & A_{yz} \\ A_{zx} & A_{zy} & A_{zz} \end{pmatrix} . \tag{2}$$

The hyperfine terms of Eq. (1) can be divided into groups with respect to the Cartesian coordinates of the spin operators:

- Secular terms:

$$A_{zz}S_zI_z \ .$$

- Pseudo-secular terms:

$$A_{zx}S_zI_x \text{ and } A_{zy}S_zI_y \ .$$

- Non-secular terms:

$$A_{xz}S_xI_z,\ A_{yz}S_yI_z,$$
$$A_{xy}S_xI_y,\ A_{yx}S_yI_x,$$
$$A_{xx}S_xI_x \text{ and } A_{yy}S_yI_y \ .$$

Since the tensor $\mathbf{A}$ is symmetric ($A_{ij} = A_{ji}$) it can be transformed into diagonal form with:

$$\mathbf{A} = \begin{pmatrix} A_{xx} & 0 & 0 \\ 0 & A_{yy} & 0 \\ 0 & 0 & A_{zz} \end{pmatrix} \ .$$

The isotropic part is now expressed by the isotropic mean-value:

$$A_{iso} = \frac{1}{3}\left(A_{xx} + A_{yy} + A_{zz}\right) \ ,$$

the anisotropy is given by:

$$\Delta A = A_{zz} - A_{iso} \ ,$$

and an asymmetry parameter is defined with:

$$\eta = \frac{A_{yy} - A_{xx}}{\Delta A} \ .$$

The diagonal elements have to be ordered appropriately to get the minimal positive value for η ($0 \leq \eta \leq 1$).

2.4.3.1 ^{14}N *Hyperfine Interaction*

Because of the axial symmetry of the NV-center, the principal coordinate systems of the hyperfine interaction tensor and the zero-field splitting are equal and the hyperfine tensor is given in diagonal form:

$$\mathbf{A}_{14N} = \begin{pmatrix} A_{\perp_{14N}} & 0 & 0 \\ 0 & A_{\perp_{14N}} & 0 \\ 0 & 0 & A_{||_{14N}} \end{pmatrix} \ .$$

Thus the hyperfine Hamiltonian can be written as:

$$H_{HF_{14N}} = \underbrace{A_{||_{14N}} S_z I_{z,14N}}_{sec.} + \underbrace{A_{\perp_{14N}} \left(S_x I_{x,14N} + S_y I_{y,14N} \right)}_{nonsec.} . \quad (3)$$

The value of the secular term is $A_{||_{14N}} = 2.15$ MHz and of the non-secular term is $A_{\perp_{14N}} = 2.3$ MHz [40][1].

2.4.3.2 ^{13}C *Hyperfine Interaction*

Carbon has two stable isotopes ^{12}C and ^{13}C. The natural abundance of ^{12}C, which is spinless, is 98.9 %. ^{13}C, which has a nuclear spin $I = 1/2$, has a natural abundance of 1.1 %. The precise form of the hyperfine interaction between ^{13}C and the NV electron spin is still under research [41]. The relevant parts of the hyperfine Hamiltonian, which were used within the simulations shown in this thesis, are:

$$\begin{aligned} H_{HF_{13C}} = & \underbrace{A_{||_{13C}} S_z I_{z,13C}}_{sec.} + \underbrace{A_{\perp_{13C}} \left(S_x I_{x,13C} + S_y I_{y,13C} \right)}_{nonsec.} + \\ & \underbrace{A_{ps_{13C}} \left(S_z I_{x,13C} + S_z I_{y,13C} + S_x I_{z,13C} + S_y I_{z,13C} \right)}_{pseudosec.} . \end{aligned} \quad (4)$$

The coefficients $A_{||_{13C}}$, $A_{\perp_{13C}}$ and $A_{ps_{13C}}$ are the secular, non-secular and pseudo-secular hyperfine coupling constants. It was assumed that the hyperfine interaction is symmetric $\eta = 0$ such that $A_{\perp_{13C,xx}} = A_{\perp_{13C,yy}} = A_{\perp_{13C}}$. The values of the hyperfine parameters depend on the distance between the NV-center and the ^{13}C. The size of the secular contribution $A_{||_{13C}}$ has been measured for several ^{13}C with different separations [42, 43]. It reaches a maximum of ≈ 130 MHz for a ^{13}C in a nearest-neighbor lattice site [7, 39]. In this thesis a coupling strength of $A_{||_{13C}} \approx 126.5$ MHz in a chirped Ramsey experiment at a weak external magnetic field strength was measured [22] (cf. section 4.2.5). The results of a chirped Ramsey measurement at a 'higher' magnetic field strength (cf. section 4.2.6) and the corresponding simulations (cf. section 4.2.7) indicate that the hyperfine tensor for the nearest-neighbor ^{13}C is even more complex. Here, we obtained for the components of the hyperfine Hamiltonian given by Eq. (4): $A_{||_{13C}} = 123.5$ MHz, $A_{\perp_{13C}} = 127$ MHz and $A_{ps_{13C}} = -4$ MHz. More details are given in sec. 4.2.7.

2.4.4 *Total Spin Hamiltonian*

Including all terms introduced in the sections above the entire NV Hamiltonian is:

1 In the reference the secular hyperfine term is $A_{||} = 2.1$ MHz. Here we will proceed with the value given in the text since it corresponds to what we have measured.

$$H_{tot} = H_e + (H_{^{14}N} + H_{HF_{^{14}N}}) + (H_{^{13}C} + H_{HF_{^{13}C}}) \ . \tag{5}$$

$$H_e = D\left(S_z^2 - \frac{2}{3}1\right) + g_e\mu_B \mathbf{BS} \tag{6}$$

$$H_{^{14}N} = P\left(I_{z,^{14}N}^2 - \frac{2}{3}1\right) - g_{^{14}N}\mu_{^{14}N}\mathbf{BI}_{^{14}N} \tag{7}$$

$$H_{^{13}C} = -g_{^{13}C}\mu_{^{13}C}\mathbf{BI}_{^{13}C} \ . \tag{8}$$

The values of the zero-field splitting D and the ^{14}N nuclear quadrupole interaction have been introduced in sections 2.4.2 and 2.4.1. The second terms of Eq. (6) to (8) are Zeeman interactions and the gyromagnetic ratios are for the electron: $g_e\mu_B = 2.8$ MHz/G, for the ^{14}N: $g_{^{14}N}\mu_{^{14}N} = 0.31$ kHz/G and for the ^{13}C: $g_{^{13}C}\mu_{^{13}C} = 1.07$ kHz/G. The hyperfine interaction Hamiltonians $H_{HF_{^{14}N}}$ and $H_{HF_{^{13}C}}$ are given by Eq. (3) and (4).

2.5 EPR SPECTRUM

The fluorescence emission of the NV-center depends on the spin state of the electron which allows the optical detection of the electron paramagnetic resonance (EPR) spectrum. Depending on the experimental conditions the EPR spectrum contains frequencies which can be attributed to transitions with different transition probabilities. The transition frequencies and the spin energy levels as well as the transition probabilities depend on experimental conditions, for example like the orientation of an external magnetic field. This dependency is shown in section 2.5.1 where we give analytical expressions for the energy levels of the electron spin which were gained from the *perturbation theory*. We compare these results with numerically gained results. In section 2.5.2 we show the optically detected EPR spectrum. In section 2.5.3 the formalism to calculate the transition probability for a given excitation operator is introduced.

2.5.1 *Perturbation Analysis*

The Hamiltonian given by Eq. (5) can easily be diagonalized by numerical means. But to get more insights, for example in how an external magnetic field influences the eigenvalues of the Hamiltonian, analytical expressions are needed. As the analytical diagonalization of a Hamiltonian is not an easy task and sometimes not feasible, approximation methods like the *perturbation theory* can be used to gain the eigenfunctions and eigenvalues of the Hamiltonian. To apply this approach the system Hamiltonian is split into a non-perturbed (secular) and a perturbed (non-secular) part. Here, the non-perturbed

part is given by H_0 and the perturbed part by V. In the case of non-degenerated eigenvalues the following expressions can be used to calculate the first and second order corrections for the eigenvalues of H_0 [44]:

$$\begin{aligned} \Delta_n^{(1)} &= \left\langle n^{(0)}|V|n^{(0)}\right\rangle = V_{nn} \\ \Delta_n^{(2)} &= \left\langle n^{(0)}|V|n^{(1)}\right\rangle = \sum_{k\neq n} \frac{|V_{nk}|^2}{E_n^{(0)} - E_k^{(0)}} . \end{aligned} \tag{9}$$

$E_n^{(0)}$ is the n-th eigenvalue of the non-perturbed Hamiltonian H_0 and $\left|n^{(0)}\right\rangle$ denotes the n-th non-perturbed eigenstate. $\Delta_n^{(i)}$ denotes the i-th order correction of $E_n^{(0)}$ and $\left|n^{(1)}\right\rangle$, which is given by:

$$\left|n^{(1)}\right\rangle = \sum_{k\neq n} \frac{V_{nk}}{E_n^{(0)} - E_k^{(0)}} \left|k^{(0)}\right\rangle ,$$

is the first order corrections of the n-th eigenstate. To apply the perturbation theory approach the contributions of the perturbation V to the system have to be small compared to H_0 (i.e. $|V_{nn}| \ll \left|E_n^{(0)} - E_k^{(0)}\right|$). For the results shown in this section we used the Hamiltonian given by Eq. (5) neglecting the coupling to any ^{13}C. We assumed that the NV-center is exposed to an external magnetic field of an arbitrary orientation with respect to the NV symmetry axis. The secular H_0 and non-secular parts V of the NV Hamiltonian are given by:

$$H_0 = H_e^{sec.} + H_{14N}^{sec.} + H_{HF_{14N}}^{sec.} \tag{10}$$

$$V = H_e^{nonsec.} + H_{14N}^{nonsec.} + H_{HF_{14N}}^{nonsec.} . \tag{11}$$

For details regarding the components of the Hamiltonians compare section 2.4. The unperturbed eigenvalues of H_0 given in unit of frequency are:

$$\begin{aligned} |-1,-1\rangle : \quad E_1 &= \frac{D+P}{3} + A_{\parallel_{14N}} - (c_e + c_{14N})\, B_z \\ |-1,\ \ 0\rangle : \quad E_2 &= \frac{D-2P}{3} - c_e B_z \\ |-1,+1\rangle : \quad E_3 &= \frac{D+P}{3} - A_{\parallel_{14N}} - (c_e - c_{14N})\, B_z \end{aligned}$$

$$
\begin{aligned}
|\ 0,-1\rangle: \quad E_4 &= -\frac{2D-P}{3} - c_{14N}B_z \\
|\ 0,\ \ 0\rangle: \quad E_5 &= -\frac{2}{3}(D+P) \\
|\ 0,+1\rangle: \quad E_6 &= -\frac{2D-P}{3} + c_{14N}B_z \\
|+1,-1\rangle: \quad E_7 &= \frac{D+P}{3} - A_{\parallel_{14N}} + (c_e - c_{14N})\,B_z \\
|+1,\ \ 0\rangle: \quad E_8 &= \frac{D-2P}{3} + c_e B_z \\
|+1,+1\rangle: \quad E_9 &= \frac{D+P}{3} + A_{\parallel_{14N}} + (c_e + c_{14N})\,B_z\ ,
\end{aligned}
$$

with $c_e = g_e\mu_B$ and $c_{14N} = g_{14N}\mu_{14N}$. The expressions $|m_S = 0, \pm 1, m_I = 0, \pm 1\rangle$ to the left of the above equations denote the spin quantum numbers corresponding to the eigenvalues. The first and second order corrections to the unperturbed eigenvalues are:

$$
\begin{aligned}
\delta E_1 &= \frac{1}{2}\left(B_x^2 + B_y^2\right)\left[\frac{c_{14N}^2}{A_{\parallel_{14N}} - P + B_z c_{14N}} + \frac{c_e^2}{A_{\parallel_{14N}} + D - B_z c_e}\right] \\
\delta E_2 &= \frac{A_{\perp_{14N}}^2}{D + P - B_z c_{14N} - B_z c_e} + \\
&\quad \frac{1}{2}\left(B_x^2 + B_y^2\right)\left[\frac{c_{14N}^2}{A_{\parallel_{14N}} + P + B_z c_{14N}} - \frac{c_{14N}^2}{A_{\parallel_{14N}} - P + B_z c_{14N}} + \frac{c_e^2}{D - B_z c_e}\right] \\
\delta E_3 &= -\frac{A_{\perp_{14N}}^2}{A_{\parallel_{14N}} - D + P + B_z c_{14N} + B_z c_e} - \\
&\quad \frac{1}{2}\left(B_x^2 + B_y^2\right)\left[\frac{c_{14N}^2}{A_{\parallel_{14N}} + P + B_z c_{14N}} + \frac{c_e^2}{A_{\parallel_{14N}} - D + B_z c_e}\right] \\
\delta E_4 &= -\frac{A_{\perp_{14N}}^2}{D + P - B_z c_{14N} - B_z c_e} - \\
&\quad \frac{1}{2}\left(B_x^2 + B_y^2\right)\left[\frac{c_{14N}^2}{P - B_z c_{14N}} + \frac{c_e^2}{A_{\parallel_{14N}} + D - B_z c_e} + \frac{c_e^2}{D - A_{\parallel_{14N}} + B_z c_e}\right] \\
\delta E_5 &= A_{\perp_{14N}}^2\left[\frac{1}{A_{\parallel_{14N}} - D + P + B_z c_{14N} + B_z c_e} - \frac{1}{D - A_{\parallel_{14N}} - P + B_z c_{14N} + B_z c_e}\right] - \\
&\quad \frac{1}{2}\left(B_x^2 + B_y^2\right)\left[\frac{c_e^2}{D + B_z c_e} + \frac{c_e^2}{D - B_z c_e} - \frac{c_{14N}^2}{P + B_z c_{14N}} - \frac{c_{14N}^2}{P - B_z c_{14N}}\right] \\
\delta E_6 &= -\frac{A_{\perp_{14N}}^2}{D + P + B_z c_{14N} + B_z c_e} - \\
&\quad \frac{1}{2}\left(B_x^2 + B_y^2\right)\left[\frac{c_{14N}^2}{P + B_z c_{14N}} + \frac{c_e^2}{A_{\parallel_{14N}} + D + B_z c_e} - \frac{c_e^2}{A_{\parallel_{14N}} - D + B_z c_e}\right]
\end{aligned}
$$

$$
\begin{aligned}
\delta E_7 &= \frac{A^2_{\perp_{14N}}}{D - A_{\parallel_{14N}} - P + B_z c_{14N} + B_z c_e} - \\
&\quad \frac{1}{2}\left(B_x^2 + B_y^2\right)\left[\frac{c^2_{14N}}{A_{\parallel_{14N}} + P - B_z c_{14N}} - \frac{c_e^2}{D - A_{\parallel_{14N}} + B_z c_e}\right] \\
\delta E_8 &= \frac{A^2_{\perp_{14N}}}{D + P + B_z c_{14N} + B_z c_e} + \\
&\quad \frac{1}{2}\left(B_x^2 + B_y^2\right)\left[\frac{c_e^2}{D + B_z c_e} + \frac{c^2_{14N}}{A_{\parallel_{14N}} + P - B_z c_{14N}} + \frac{c^2_{14N}}{P - A_{\parallel_{14N}} + B_z c_{14N}}\right] \\
\delta E_9 &= -\frac{1}{2}(B_x^2 + B_y^2)\left[\frac{c^2_{14N}}{\left(P - A_{\parallel_{14N}} + B_z c_{14N}\right)} - \frac{c_e^2}{\left(A_{\parallel_{14N}} + D + B_z c_e\right)}\right] .
\end{aligned}
$$

To visualize the dependency of the calculated eigenvalues on the field orientation, we performed simulations for a magnetic field constant field strength $B_0 = 70$ G but different orientations. For the simulations shown in fig. 4.a the field was rotated in the xz-plane with:

$$
\begin{aligned}
B_x &= \sin(\theta) \cdot B_0 \\
B_y &= 0 \\
B_z &= \cos(\theta) \cdot B_0 .
\end{aligned}
$$

θ is the angle enclosed by the vector of the magnetic field $\mathbf{B}_0$ and the z-axis of the laboratory coordinate system. Since the Hamiltonian is of axial symmetry one can safely make B_y zero. In fig. 4.b results of a numerical diagonalization of the Hamiltonian $H_0 + V$ are shown for comparison. For field angles $\theta < 90°$ the result of the perturbation approach is equal to the numerical approach but it deviates for θ approaching 90°. This is because the energy levels are degenerated at this field orientation and the degenerated perturbation theory must be applied. For our purpose the non-degenerated approach is sufficient because we are only interested in the region below 90°. Since the energy levels can be attributed to the non-perturbed eigenvalues we will use these results in section 7 where the transition frequencies and transition probabilities of the NV-center in a tilted magnetic field are analyzed numerically.

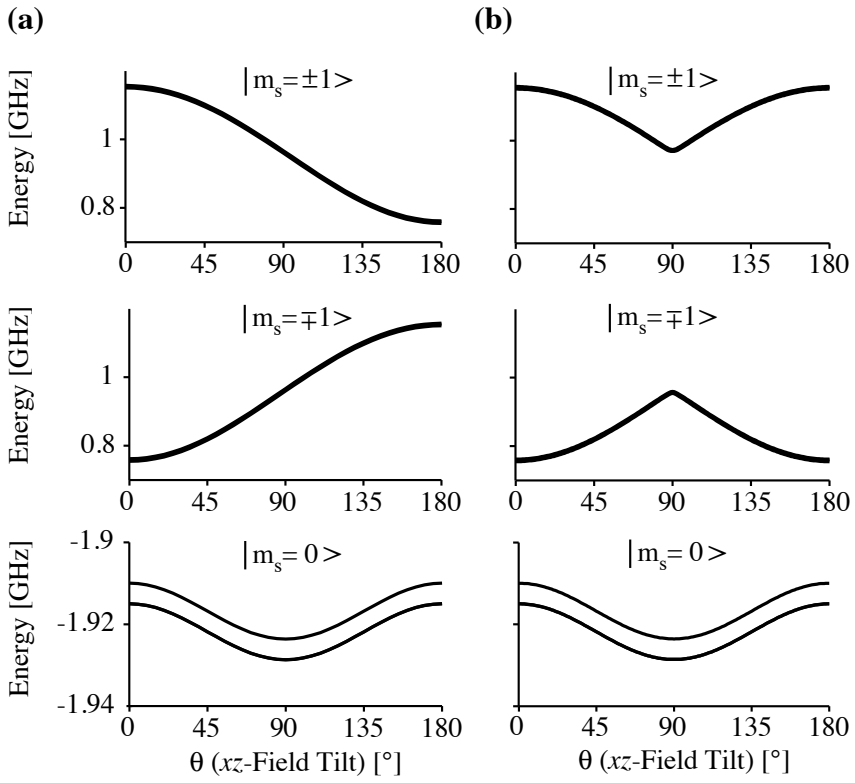

Figure 4: Dependency of the energy levels of the NV electron spin on the magnetic field orientation in the xz-plane. The field tilt angle varies from 0° to 180° with respect to the NV symmetry axis. No field was applied in y direction. In a) the results from the non-degenerated perturbation theory are shown and in b) from the numerical diagonalization. The quantum numbers of the spin states, which are given with respect to the aligned case, are shown in the figures. Due to the scale of the y-axis the level splitting caused by the hyperfine interaction is not visible. The splitting shown for the $|m_s = 0\rangle$ state is caused by the nuclear quadrupole splitting of the ^{14}N. For field orientations $< 90°$ both methods deliver equal results. For θ approaching 90° the results deviate because the energy levels cross. In this case the degenerated perturbation theory must be applied.

2.5.2 *Electron Spin Spectrum*

The spectrum of the NV electron spin under an external magnetic field consists of three triplet bundles. These are: two single-quantum coherence triplets and one double-quantum coherence triplet. Figure 5 shows a simplified electron spin scheme and an experimental spectrum of the electronic ground state of a single NV-center measured in the ^{12}C enriched diamond sample (cf. section 2.2). The solid double-arrows mark allowed magnetic dipole transitions while the dotted double-arrow indicates a 'forbidden' double-quantum transition. The dotted single-arrows assign the transitions to the corresponding lines of the measured spectrum. Due to the hyperfine coupling to the NV

nuclear spin the energy levels shown in the scheme split up and give rise to the triplet bundles as can be seen in the spectrum. For the outer bundles (single-quantum coherences) the line splitting is 2.15 MHz and for the central bundle (double-quantum coherence) the splitting is 4.3 MHz.

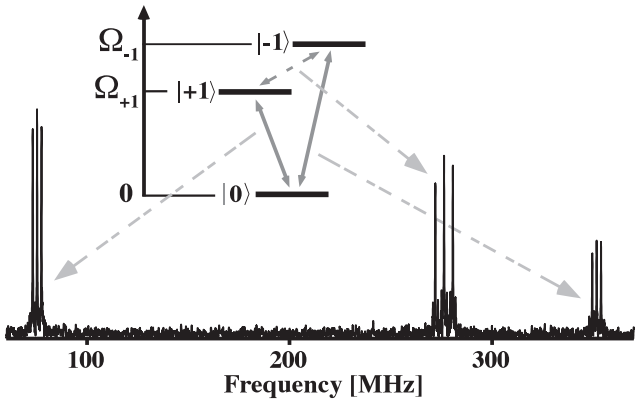

Figure 5: Relevant three-level system of the S=1 electron spin, together with an experimental spectrum. The full arrows indicate allowed magnetic dipole transitions. For experimental conditions under which the spectrum was recorded see section 4.1.3.

2.5.3 *State mixing and transition probabilities*

If the system Hamiltonian H_0 of the NV-center and the electron spin matrix S_z commute, then the state of the spin system can be described by the eigenvalues $m_S = 0, \pm 1$ of S_z which are called in this case *good quantum numbers*. A resonant microwave field can induce transitions between spin levels which change the spin quantum number by $\Delta m_S = 1$. If the system Hamiltonian contains outer diagonal elements, for example due to a tilted external magnetic field, H_0 and S_z do not commute anymore. In this case a microwave field can induce transitions between spin levels which were forbidden in the non-perturbed case and the eigenvalues of S_z are no longer good quantum numbers. The transition probability between two eigenstates $\mathbf{e}_i$ and $\mathbf{e}_j$ of the system Hamiltonian due to an excitation Hamiltonian $H_1 \propto M \cdot B_1 \cos(\omega t)$ is given by [45]:

$$P_{ij} \propto \left| \langle \mathbf{e}_i | M | \mathbf{e}_j \rangle \cdot B_1 \cos(\omega t) \right|^2 \delta(\omega_{ij} - \omega) \ ,$$

with magnetic moment operator $M = a \cdot S_x + b \cdot S_y + c \cdot S_z$. The matrix $\langle \mathbf{e}_i | M | \mathbf{e}_j \rangle$ contains all relevant information regarding the transition probabilities and can be obtained by transforming M into the eigenbase of H_0. Giving the eigenstates $\mathbf{e}_i$ in form of a matrix $\mathbf{V}$ the transition amplitude matrix results from:

$$\mathbf{T} = \mathbf{V}^{+} \cdot M \cdot \mathbf{V}\,. \tag{12}$$

2.6 SPIN CONTROL

Coherent control of an electron spin is achieved by application of resonant and near-resonant oscillating electromagnetic fields at the location of a spin. The fields could either be applied continuously or in a pulsed scheme. Usually linearly polarized fields are used for excitation which can be considered as a superposition of two counter rotating circular polarized fields. In the excitation process only one circular field component, whose rotation direction is equal to that of the spin, induces a transition. The contribution of the other circular field component can be neglected. Usually this is included in the *rotating wave approximation* by which a transformation into a rotating reference frame is performed. In the rotating frame the system and excitation Hamiltonians are time-independent.

To visualize the dynamics of a spin (or pseudo-spin) $S = 1/2$ the *Bloch sphere* can be used. Here, the spin is represented by a vector pointing from the center of the sphere to its surface. The radius of the Bloch sphere is normalized and given without units. The $+z$ and $-z$ axes of the sphere correspond to the two eigenstates of the spin which are denoted here as $|0\rangle$ (ground state) and $|1\rangle$ (excited state). Superpositions of eigenstates can be created by rotating the state vector along the sphere's surface. By projection of the vector onto the z-axis the probability to find the spin in one of its eigenstates is obtained.

In the following sections fundamental pulse sequences to control the NV electron spin are introduced. In the first section sequences are shown which are applied to single-quantum transitions. In the next section sequences of pulse are shown which create double-quantum coherences.

2.6.1 *Single-Quantum Transition*

Quantum transitions can be defined by the difference of the quantum numbers of the participating states. In case of a spin $1/2$ the quantum numbers of the eigenstates are $|m_s = +1/2\rangle$ and $|m_s = -1/2\rangle$. The difference is $\Delta m_s = 1$ and the transition is called *single-quantum transition*. The NV electron spin is a spin 1. If only one transition is excited, for example $|0\rangle \leftrightarrow |+1\rangle$, the dynamics of the spin can be described as a pseudo-spin $1/2$. Before a microwave sequence is applied to the NV electron spin usually a laser pulse has to be applied first to initialize the electron spin. In the diagrams of the sequences shown here, this laser pulse is not shown for the sake of simplicity.

RABI OSCILLATION A very simple sequence to control the NV electron spin is to apply a rectangular pulse of resonant microwaves to a spin transition. Due to the microwave pulse the electron spin oscillates periodically between two eigenstates. The number of oscillation periods increases with the duration of the pulse. This oscillation is called Rabi oscillation and the corresponding frequency is the Rabi frequency. The Rabi oscillation of the NV electron spin can be measured by successively increasing the duration of the pulse and reading out the bright state population after every increment as shown in fig. 6.a. Figure 6.b shows measured Rabi oscillations of the left

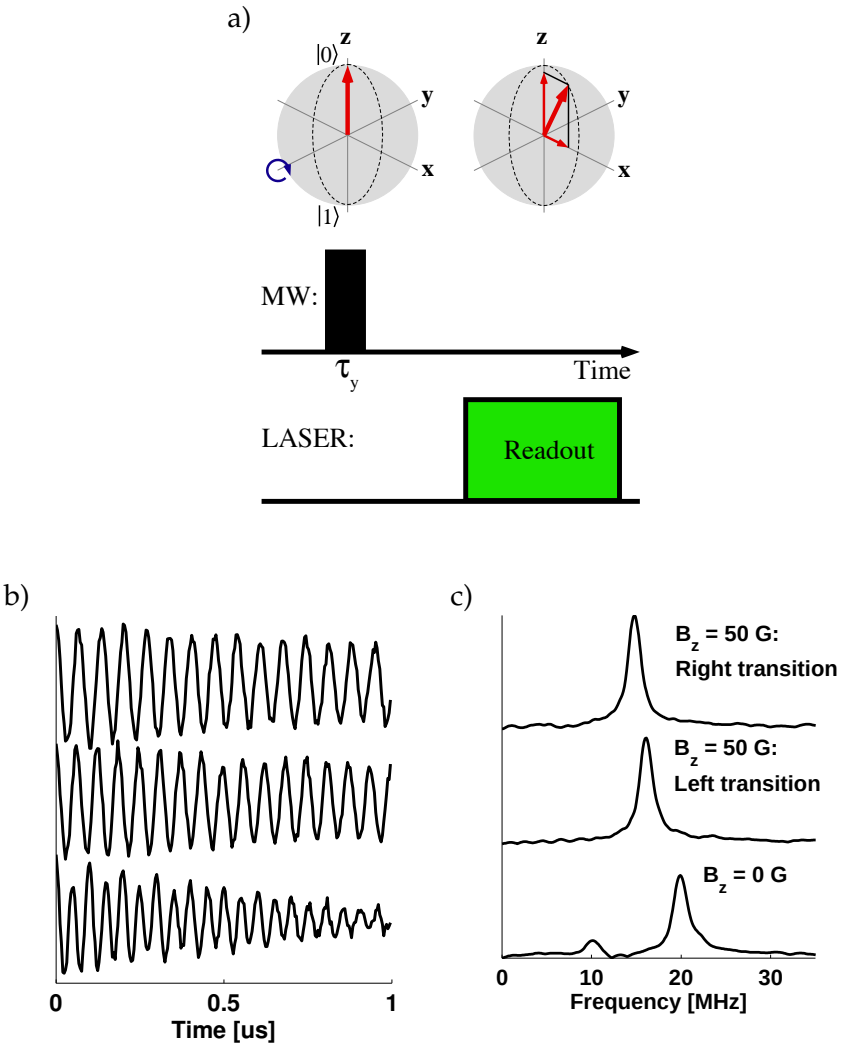

Figure 6: Rabi sequence: a) The upper diagram shows the evolution of the electron spin in the Bloch sphere. The bended arrow (blue) shows the direction of rotation of the spin vector. In b) time-domain signals of Rabi oscillations are shown. The upper two traces belong to the right and left transition (compare spectrum of fig. 5) of the electron spin for a projected field strength of $B_0 \approx 50$ G. The lower trace shows the Rabi oscillation for a field strength of $B_0 \approx 0$ G. In c) the spectra of the Rabi oscillations are shown.

(low frequency (for notation cf. fig. 8.b)) and right (high frequency) electron spin transition for an external magnetic field $B_z > 0$ (upper two traces) and for $B_z = 0$ (bottom trace). Figure 6.c shows the corresponding spectra of the Rabi oscillations. The Rabi frequency for the degenerated case ($B_z = 0$ G) is by a factor of approximately $\sqrt{2}$ larger compared to the non-degenerated case ($B_z > 0$ G). This is explained by considering the absorption of both field components, the left and right rotating circular fields of the excitation field in the degenerated case. In the non-degenerated case only one component of the excitation field contributes to the excitation. A gaussian window function was multiplied to the time-domain signal prior to a zero-filling. The small peak at around 10 MHz might indicate that the external magnetic field was not exactly equal to zero and tilted with respect to the symmetry axis of the NV-center which was supported by numerical simulations.

RAMSEY FRINGES The Ramsey sequence is a simple pulse sequence consisting of two $\pi/2$-pulses separated by a delay time. Figure 7.a shows a scheme of the Ramsey sequence and the spin evolution. Starting with polarization along the z-axis, the power and duration of a $\pi/2$-pulse matches the condition to flip the spin vector into the xy-plane. The condition for the parameter values to achieve a precise spin rotation depends on the oscillator strength of the spin transition. The created state is a coherent superposition of the two eigenstates. During the subsequent delay time the spin state freely evolves in the xy-plane. The last pulse transforms the coherence to population, which is readout by applying a laser pulse as discussed in 2.3. Figures 7.b and 7.c show the time-domain signal and the corresponding spectrum of a Ramsey fringe pattern.

CHIRPED RAMSEY Depending on its duration an excitation pulse covers some frequency bandwidth which is obtained by the Fourier transformation of the pulse. The spectrum of a rectangular pulse is given by the sinc-function ($\mathrm{sinc}(x) = \sin(x)/x$). As a first approximation the bandwidth is given by the inverse of the pulse duration $f_{\mathrm{bdw}} = \tau^{-1}$. All transitions within the range of the bandwidth are excited. The different evolution frequencies superimpose and result in a modulated time-domain signal as shown by fig. 7.b. By Fourier transformation the spectrum is obtained which contains the frequencies of the excited transitions.

To excite multiple transitions in a broader frequency range shorter pulses with higher power are needed, which is not always feasible. Another method to perform a broad frequency range excitation is to use frequency-chirped pulses [46, 47, 48]. The advantage of chirped pulses is that there is theoretically no limit in bandwidth and no in-

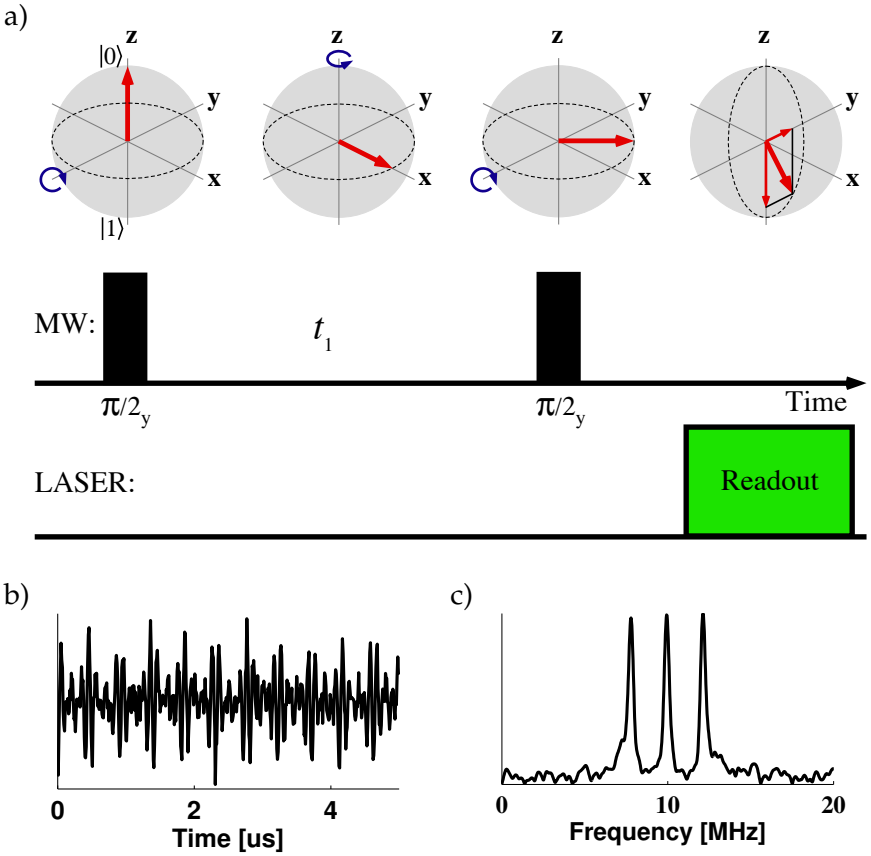

Figure 7: In a) the Ramsey sequence and the spin evolution in the Bloch sphere are shown: The upper part of the diagram shows the result of the microwave pulses and the free evolution of the spin state. The bended arrows show the direction of rotation of the spin vector. In b) a Ramsey fringe pattern and in c) the corresponding spectrum are shown. The spectrum shows three lines with a separation of 2.15 MHz of the outer from the central line. This line triplet is due to the hyperfine interaction of the electron spin with the ^{14}N nuclear spin.

crease of the pulse power is needed. The time-signal of a chirp can be written as:

$$s(t) = \sin\left(2\pi \int f(t)\, dt\right) .$$

The function $f(t)$ contains the frequency dependence and, for a linear chirp, is given by:

$$f(t) = f_0 + f_{inc} t .$$

f_0 is the starting frequency of the chirp and f_{inc} is the frequency increment per time. The time-domain signal of the pulse then becomes:

$$s(t) = \sin\left(2\pi \left(f_0 + \frac{f_{inc}}{2} t\right) t\right) .$$

In this thesis we used a modified Ramsey-sequence where the $\pi/2$-pulses were replaced by chirped pulses and applied it to NV-centers in diamond. Details of this measurement are given in chapter 4.

2.6.2 *Double-Quantum Transition*

For a double-quantum transition the quantum numbers of the two involved eigenstates differ by $\Delta m_s = 2$. The electron spin of the NV-center in diamond is $S = 1$. The quantum numbers of the electron spin eigenstates are $m_s = -1, 0, +1$. Thus there is one double-quantum transition (i.e. $|-1\rangle \leftrightarrow |+1\rangle$) where a coherence can be created. Resonant excitation of double-quantum transitions are forbidden because the photons which are the driving particles of the excitation field have a spin quantum number of 1. By absorption of a single resonant photon the spin quantum number of the qubit has to change by $\Delta m_s = \pm 1$. To drive a double-quantum transition two photons have to be absorbed. This can be achieved by using composite pulses exciting both transitions $|0\rangle \leftrightarrow |-1\rangle$ and $|0\rangle \leftrightarrow |+1\rangle$ successively. Figure 8 shows composite pulses corresponding to $\pi/2$- and π-pulses on the double-quantum transition.

These pulses can be incorporated into the sequences introduced in section 2.6.1 for measuring e.g. the Ramsey-fringe pattern of the double-quantum coherence. In chapter 5.2 measurements are shown where we have incorporated the composite pulses into sequences for performing dynamical decoupling on the double-quantum transition.

2.7 RELAXATION

The loss of information due to relaxation is a crucial issue in quantum information and computation. There are several sources which cause the loss of information in quantum systems and qubit registers. In the case of NV-centers in diamond this happens for example due to spin impurities like ^{13}C in the proximity of the qubits. By reducing

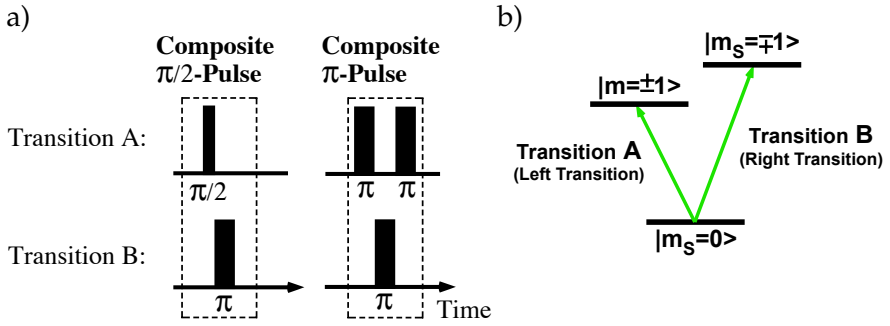

Figure 8: a) Composite pulses for exciting double-quantum transitions $\pi/2$- and π-pulse. b) Simplified electron spin level scheme.

the content of spin impurities or the temperature of the sample [49] a reduction of the relaxation processes can be achieved. Relaxation processes are separated in two groups: *longitudinal* and *transverse* relaxation. In the following these relaxation processes will be introduced briefly. More detailed descriptions can be found in [50].

2.7.1 *Longitudinal Relaxation:* T_1

Longitudinal relaxation is a process where energy between the crystal lattice and the spin system is exchanged, and so this relaxation is also called *spin-lattice relaxation*. Due to the longitudinal relaxation the spin reaches a state of thermal equilibrium where the population P_i of the eigenstate i is correlated with its energy E_i and is given by the Boltzmann distribution function $P_i \propto \exp\left(-\frac{E_i}{k_B T}\right)$. If the populations of the spin states are changed by application of microwave pulses the system relaxes back to the original population distribution on a time scale defined by the longitudinal relaxation time constant T_1. The difference of population between the spin states which is usually very small at room temperature, can be increased in case of NV-centers in diamond by irradiation with a green laser and reaches a maximum population of the electron spin ground state $|m_S = 0\rangle$ of ≈ 90 % [34]. The energy exchange between the spin and environment of the longitudinal relaxation is induced by phonon interactions with the crystal lattice. In general processes like the *direct*, *Raman* and *Orbach* process contribute to the longitudinal relaxation [50]. In the case of the NV-centers in diamond the spin-lattice relaxation is attributed to a two-phonon *Orbach* process which fits best to the experimentally observed relaxation [51].

2.7.1.1 T_1 *Relaxation of NV Electron Spin in Diamond*

For the natural abundance sample used in this thesis we measured longitudinal relaxation times, for the bright state, of $T_1^{Bright} \approx 4$ ms and, for the dark state, of $T_1^{Dark} \approx 10$ ms. Figure 9.a shows the sequence we used for measuring the longitudinal relaxation time constant of the bright state and fig. 9.b for the dark state.

The relaxation time constant of the bright state T_1^{Bright} is approximately half as big as that of the dark state T_1^{Dark}. This is explained by the number of relaxation paths of the states. If the spin population is initially in the bright state $|m_S = 0\rangle$, there are two relaxation paths (one for each dark state$|m_S = \pm 1\rangle$). On the other hand, if the spin is initially prepared in one of the dark states, there is only a single relaxation path (into the bright state).

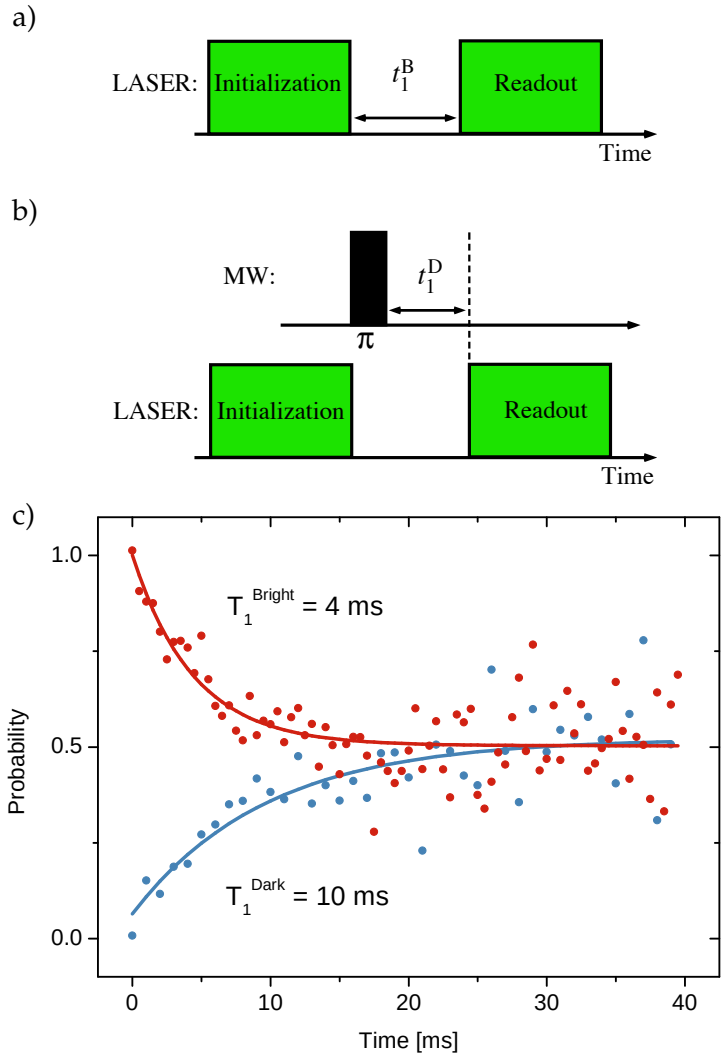

Figure 9: Measurement of longitudinal relaxation time constant: In a) and b) the sequence for measuring the longitudinal relaxation time constants of the bright and for the dark state are shown. t_1^B and t_1^D denote the delay times between initial state preparation and readout. In c) the results of the measurements are shown.

2.7.2 *Transverse Relaxation: T_2*

Transverse relaxation is a process where an ensemble of spins, which are initially in phase, evolve due to local field distortions with different Larmor frequencies, run out of phase (dephasing). Even if the measurements presented in this thesis were performed on single NV-centers, we had a temporal-ensemble of spins since we had to repeat a measurement multiple times to gain a suitable signal-to-noise level of the detected photons. The time scale of the transverse relaxation is given by the constant T_2^* which is also called *phase-memory time*. T_2^* can be obtained from the width of the lines of the spectrum of a Ramsey fringe pattern.

Due to the application of refocusing sequences like the Hahn echo sequence (cf. sec. 2.8) the coherence time can be extended and gives a relaxation time which is denoted by T_2 and is called *spin-spin-relaxation*. The T_2 relaxation is caused by interactions between the target spin and environmental spins like: dipolar interaction, exchange interaction, anisotropic hyperfine interaction, spin-flip and spin-flip-flop processes [52, 50]. Unlike the longitudinal relaxation, transverse relaxation can be energy conserving. Thus it can be refocused and the coherence time can be extended for example by application of *dynamical decoupling sequences* (cf. sec. 2.8). The T_2 relaxation time depends on the exchange rate τ_{en} between the spin and environment and the spin-lattice relaxation T_1. In extreme case it is either dominated by τ_{en} or T_1. By the application of a decoupling sequence the effective interaction strength with the environment is reduced and T_2 will approach T_1 as a limit.

2.7.2.1 *T_2 Relaxation of NV Electron Spin in Diamond*

The transverse relaxation of the NV electron spin coherence is not dominated by the longitudinal relaxation time T_1 but by the coupling to a bath of electron or nuclear spins of impurities surrounding the NV-center. The impurities can be substitutional ^{14}N or ^{13}C atoms. ^{14}N has an electron spin $1/2$ and a nuclear spin 1, and ^{13}C has a nuclear spin $1/2$ but no electron spin. In diamonds of type-Ib the main source of decoherence are the electron spins of the ^{14}N impurities which have a typical concentration of > 100 ppm [53]. In type IIa diamonds the transverse relaxation is attributed to the ^{13}C's which are coupled via hyperfine interaction to the NV electron spin [54]. It was shown that the T_2 relaxation time in isotopically engineered diamond, which are ^{12}C enriched, is increased compared to natural abundance samples [55]. For this thesis we used a natural abundance diamond sample with typical relaxation times in the order of $T_2^* \approx 1\ \mu$s and a ^{12}C enriched sample with $T_2^* > 200\ \mu$s. Theoretical models describing the relaxation process are for example the cluster-correlation expansion method [56] and the disjoint-cluster method [57].

2.8 DYNAMICAL DECOUPLING SEQUENCES

Sufficiently long coherence times (T_2) are amongst the most important criteria for the realization of scalable quantum information processors [58], since a short coherence time limits the maximal duration for sequences implementing quantum algorithms. In solid state systems it is often possible to extend the coherence time by removing sources of decoherence from the host material, e.g. by isotopic engineering [59, 55]. If it is not possible to further reduce the detrimental effects of a noisy environment, it is possible to use a series of control pulses applied to the qubits. This approach, termed *Dynamical Decoupling* (DD), refocuses the interaction between system and environment by applying a stroboscopic sequence of inversion pulses to the qubits. It has been tested on different systems with environments consisting of electronic or nuclear spin baths [60, 61, 62, 53, 63, 64]. This technique allows, for example to extend the coherence time T_2 or to increase the sensitivity of magnetic field sensors to measure *ac* magnetic fields [65, 63]. The overall effect of these sequences is a decoupling of a target spin from a spin environment. In the following sections some dynamical decoupling sequences will be introduced which have been used for this thesis. We applied some of these sequences to single- (cf. section 5.1) as well as double-quantum transitions (cf. section 5.2). Before a microwave sequence is applied to the NV electron spin a laser pulse has to be applied first to initialize the electron spin. In the diagrams of the sequences shown below this laser pulse is not shown for the sake of simplicity.

Basic Theory

Dynamical decoupling sequences consist of a series of inversion pulses which are separated by delay times. The dulse-delay schemes of DD sequences can be quite different, but the overall effect is the reduction of the influence of the system-environment interaction Hamiltonian which is responsible for the relaxation. In the following a brief introduction is shown of how the application of a dynamical decoupling sequence can be handled mathematically. A detailed theoretical analysis of the effect of a DD sequence is in general not trivial and depends on the used spin system, the environment and the system-environment interaction. The following derivations are based on the formalism used in [64].

It is assumed that there is a spin system (given by H_S^L) which is in contact with an environment (given by H_E^L) via a coupling Hamiltonian (given by H_{SE}^L). The Hamiltonian of the entire system in the laboratory frame can be written as:

$$H^L = H_S^L + H_{SE}^L + H_E^L \,.$$

In the case of NV-centers in diamond the spin system could be given by the NV-centers electron spin (neglecting the NV nuclear spin and the non-secular terms of the Zeeman interaction). It is assumed that the system-environment coupling is given by the secular component of dipole-dipole interaction alone. The environment could for example be a bath of ^{13}C nuclear spins or electron and nuclear spins of ^{14}N impurities [66]. The environment is coupled by Zeeman interaction to an external magnetic field and the bath spins are coupled to each other by dipole-dipole interaction. In the doubly rotating frame of $S_z + I_z$ the Hamiltonians can be written as:

$$\begin{aligned} H_S &= 0 \\ H_{SE} &= S_z \sum_j b_{Sj} I_z^j \\ H_E &= \sum_{i<j} d_{ij} \left[2 I_z^i I_z^j - \left(I_x^i I_x^j + I_y^i I_y^j \right) \right] . \end{aligned}$$

By changing into the interaction picture with respect to H_E it can be seen that the system-environment Hamiltonian H_{SE} becomes time-dependent due to the environment.

$$\begin{aligned} H_{SE}^E(t) &= S_z \cdot \exp(-iH_E t) \left(\sum_j b_{Sj} I_z^j \right) \exp(iH_E t) \\ &= S_z \cdot \gamma_{SE}(t) . \end{aligned}$$

If the DD sequence is set up of periodic blocks, its effect can be examined by calculating the propagator of the sequence, which is given by the unitary operation:

$$U_{DD}(\tau_c) = U_f(\tau_{N+1}) U_p^N(\tau_p) U_f(\tau_N) \cdot \ldots \cdot U_p^1(\tau_p) U_f(\tau_1) . \quad (13)$$

τ_c is the duration of a single cycle of the DD sequence. $U_f(\tau_i)$ is the i-th free evolution propagator of duration τ_i. For strong control pulses the free evolution Hamiltonian can be neglected while a pulse is applied and the i-th pulse propagator is given by:

$$U_p^i(\tau_p) = T \exp\left(-i \int_0^{\tau_p} H_p^i\left(t'\right) dt' \right) .$$

T is the Dyson time-ordering operator. It is assumed that $H_p^i\left(t'\right)$ is constant during the application of a pulse but it might change for different pulses. The overall effect of U_{DD} can be expressed by an effective Hamiltonian H_{eff}:

$$U_{DD}(\tau_c) = \exp(-iH_{eff}\tau_c) .$$

The effective Hamiltonian H_{eff} can be expressed as a series expansion according to the average Hamiltonian theory:

$$H_{eff} = H^{(0)} + H^{(1)} + H^{(2)} + \dots . \tag{14}$$

If the spin evolution is expressed in the interaction picture the effect of the decoupling sequence on H_{SE} can be obtained. The control pulses do not affect H_E since it commutes with the pulse Hamiltonians $H_p^i(t)$. Thus after the j-th control pulse the system-environment Hamiltonian is given by:

$$H'_{SE,j} = \left(\prod_{\alpha=1}^{j} U_p^\alpha\right)^+ \cdot H_{SE} \cdot \prod_{\alpha=1}^{j} U_p^\alpha$$

It is further assumed that the system-environment Hamiltonian is piecewise constant:

$$H'_{SE}(t) = \begin{cases} H'_{SE,1} & \text{for } 0 < t \leq t_1 \\ H'_{SE,2} & \text{for } t_1 < t \leq t_2 \\ \vdots & \\ H'_{SE,N} & \text{for } t_{N-1} < t \leq t_N \end{cases}$$

and

$$\tau_c = t_N .$$

Here, it was assumed that the durations of the control pulses are negligible small. The terms of the effective Hamiltonian of Eq. (14) can be calculated using the Magnus expansion, which yields for the first term of the effective Hamiltonian H_{eff}:

$$H^{(0)} = \frac{1}{\tau_c} \int_0^{\tau_c} \left[H'_{SE}\left(t'\right) + H_E\right] dt' .$$

For an ideal dynamical decoupling sequence the integral of the first term becomes zero, and thus the zero-order term of the effective Hamiltonian is given by:

$$H^{(0)} = H_E.$$

2.8.1 *Hahn Echo Sequence*

The *Hahn echo* or *primary echo* sequence [67] is the most basic pulse sequence, which can be used to extend the coherence time of a spin state. For the case of NV-centers an additional pulse has to be added to the end of the sequence to transform the created coherence back to population. The pulse-delay scheme of the sequence, as it has been used here, is:

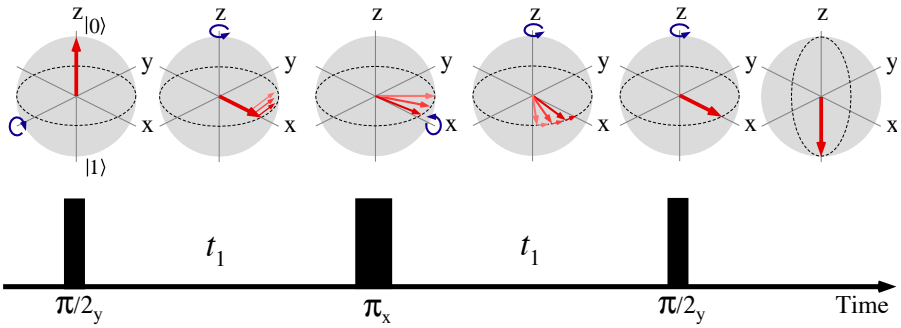

Figure 10: Hahn echo sequence. The upper part of the diagram shows the evolution of the spin vector and its state in the Bloch sphere at the times when the microwave pulses, which are shown in the lower part of the figure, are applied.

$$\pi/2_y - t_1 - \pi - t_1 - \pi/2_y \ .$$

π and $\pi/2$ stand for pulses with corresponding flip angles and t_1 stands for an evolution time. In fig. 10 a scheme of the Hahn echo sequence is visualized. The upper part of the figure shows the evolution of the spin state in the Bloch sphere, and the lower part shows the microwave pulses of the sequence. The initialization and the readout of the electron spin are done by a laser pulse at the very beginning and at the end of the sequence, which are not shown here. The red arrows indicate the state of the spin vectors at the beginning of the corresponding time segments. The bended blue arrows indicate the direction of the rotation of the spins due to the microwave pulses. Since the measurement has to be repeated several times to get a suitable signal-to-noise level, it might happen that the Larmor frequencies of the spin are different during the accumulation process of the measurement. This is indicated by the small red arrows which are perpendicular to the magnetization vector. As denoted in fig. 10, the π-pulse inverts the evolution of the temporal spin ensemble and refocuses all spins to the same time-point.

2.8.2 *CPMG Sequence*

The Hahn echo sequence performs well in refocusing dephasings which are caused by static magnetic field inhomogeneities or fluctuations which are slow compared to the inter-pulse evolution time t_1. By subdividing the evolution time into multiple segments separated by π-pulses, it is possible to further extend the transverse coherence time. If the phases of the $\pi/2$-pulse, which creates the coherence, and the inversion pulses are equal, the sequence is called *Carr-Purcell* (CP) sequence [68]. If the phase of the initial $\pi/2$-pulse and the inversion pulses is shifted by 90°, it is called *Carr-Purcell-Meiboom-Gill* (CPMG) sequence [69]. While CP shows strong susceptibility to pulse

imperfections, CPMG is very robust. The pulse-delay scheme of the sequences is:

$$\pi/2_{y,x} - \left[t_1 - \pi_y - 2t_1 - \pi_y - t_1\right]^N - \pi/2_{y,x} \ .$$

The last pulse transforms the coherence back into population. $N \geq 1$ gives the number of repetitions of the sub-sequence enclosed in the brackets. For CP the phases of the pulses, given by the indices, are equal. Here, it corresponds to rotations around the y-axis. For CPMG the $\pi/2$-pulse rotates the spin vector around the x-axis and the π-pulses induce rotations around y-axis. In fig. 11 the pulse-delay scheme of CPMG is visualized.

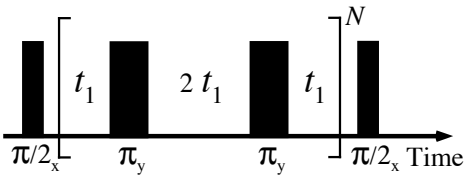

Figure 11: CPMG sequence.

2.8.3 *YX-4 Sequence*

The performance of the CPMG sequence is not symmetric and depends strongly on the orientation of the spin vector. As long as the spin vector points in the direction from which the microwaves are irradiated, the performance of the CPMG sequence is very good. But if the orientation of the spin vector deviates from the irradiation axis of the inversion pulses, the performance shrinks. It reaches a minimum for a perpendicular orientation between spin vector and irradiation direction of the inversion pulses. The condition of this case correspond to the CP sequence. The problem of this asymmetry is overcome by the XY-4 sequence which is a modification of the CP/CPMG sequence [70]. Figure 12 shows a visual scheme of the XY-4 sequence.

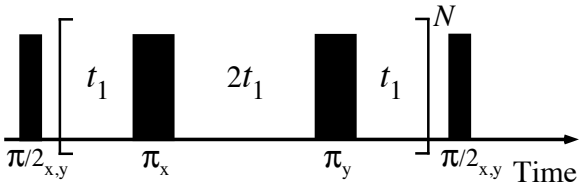

Figure 12: XY-4 sequence.

The pulse-delay scheme of XY-4 is:

$$\pi/2_{x,y} - \left[t_1 - \pi_x - 2t_1 - \pi_y - t_1\right]^{2N} - \pi/2_{x,y} \ .$$

$N \geq 1$ is the number of cycles. In contrast to CP and CPMG the refocusing pulses of XY-4 are applied alternating along the x and y

axes. XY-4 shows very good robustness against pulse imperfections and good performance in refocusing spin vectors with different orientations.

2.8.4 *KDD Sequence*

The KDD sequence was at first proposed by *Souza* et al. [71] and is based on a composite pulse which was originally used as a robust π-pulse in a CP sequence [72]. The components of the pulse, which was denoted by *Souza* et al. as *Knill-pulse*, are: $\pi_{\frac{\pi}{6}} - \pi_0 - \pi_{\frac{\pi}{2}} - \pi_0 - \pi_{\frac{\pi}{6}} = Z_{\frac{\pi}{3}}\pi_0$. The result of the Knill-pulse corresponds to a rotation around the z-axis by 60° and a 180° rotation around x-axis (the index 0 denotes a pulse phase of 0° which is equal to the *x*-axis). *Souza* et al. used the Knill-pulse as the fundamental building block for a new DD sequence, which they called KDD. A building block is given by the components of the Knill-pulse with additional delay-times separating the pulse components.

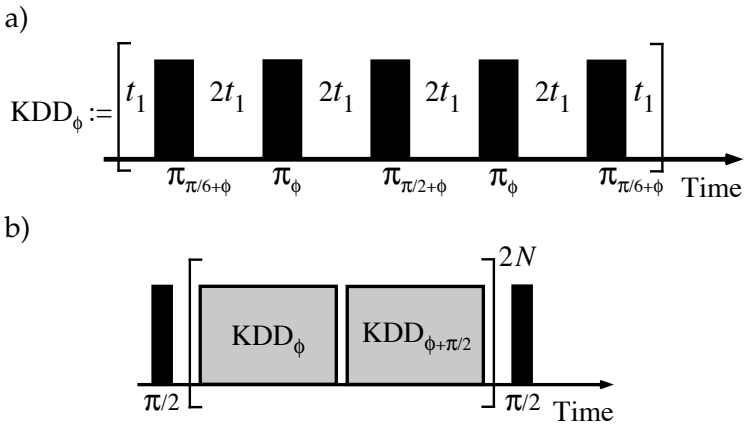

Figure 13: a) KDD building block and b) the KDD pulse sequence.

The pulse-delay scheme of the building block is:

$$\begin{aligned} \mathrm{KDD}_{\phi}^{BB} \quad = \quad & t_1 - \pi_{\frac{\pi}{6}+\phi} - 2t_1 - \pi_{\phi} - 2t_1 - \pi_{\frac{\pi}{2}+\phi} - 2t_1 - \pi_{\phi} - 2t_1 - \\ & \pi_{\frac{\pi}{6}+\phi} - t_1 \ . \end{aligned}$$

They further combined this block with a second block, whose components are shifted in phase by $\pi/2$, and the two blocks are repeated twice. The total sequence is given by:

$$\mathrm{KDD} = \left[\mathrm{KDD}_{\phi}^{BB} - \mathrm{KDD}_{\phi+\frac{\pi}{2}}^{BB}\right]^2 \ .$$

In fig. 13 a scheme of the KKD sequence is shown. The performance of the KDD sequence overcomes the performances of CPMG and XY-4 as is shown in section 5.1.

3

EXPERIMENTAL SETUP

In this section the experimental setup is described which has been used for the measurements presented in sections 4 and 5. The setup, which was built up within this thesis, consists of an optical and electronic part. The optical part is a home-built confocal microscope which is used for initialization and readout of the NV-centers electron spin. The electronic part, which is also home-built, is used for the excitation and control of the NV electron spin. Both parts are described in more detail in the following sections.

3.1 CONFOCAL MICROSCOPY

Because spatial resolution and selectivity are important elements of the work with single NV-centers, the basic features of a confocal microscope will be introduced first before the description of the optical setup follows in the subsequent section.

TRANSVERSE SELECTIVITY In a confocal microscope an optical emitter is placed in the focal point of a microscope objective (MO). The emitter is excited by a laser beam passing through the MO and being focused to its focal point. Only emitters in the focal point are excited by the laser beam and can emit photons. This yields a selective excitation and detection in transversal direction. Photons which are emitted into the direction of the MO are collected and guided to a photon detector. To get a 2-D image of the sample the microscope objective is moved step-by-step in the xy-plane and the excitation and detection procedure is repeated for every point in the xy-plane.

LONGITUDINAL SELECTIVITY The focal excitation and photon collection allows a transversal discrimination of the NV-centers. Since the laser beam might still excite emitters along its propagation direction, which are located in front of or behind the focal point, a longitudinal selection has to be performed to remove the out-of-focus photon emission. Here, a pinhole and a lens are placed in the optical detection path to suppress the contributions of emitters which are not in the focal point of the MO. As shown in fig. 15 the pinhole is placed in front of the photon detection system. The lens is placed in front of the pinhole with its focal point at the position of the pinhole. The lens focuses the collected photon emission to the pinhole and creates an image of the emitters, which had contributed to the photon emission, at the location of the pinhole. With the pinhole at the right position

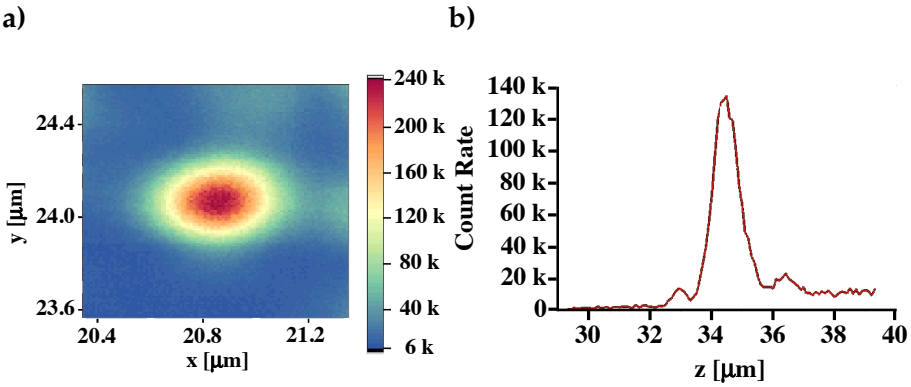

Figure 14: Confocal-Scan-Images: a) High resolution transversal and b) longitudinal scan of a NV-center.

only the photons of the emitter, which is located in the focal point of the MO, will pass through. This completes the *confocal* configuration of the microscope.

OPTICAL RESOLUTION The optical resolution d of the transverse selectivity is limited by the *diffraction limit* of the detection system and depends on the numerical aperture (NA) of the MO. We used an oil immersion MO in our setup which had a NA of 1.4 and we reached a theoretically limited transversal resolution of:

$$\begin{aligned} d &= \frac{\lambda}{2\,(n \sin(\alpha))} = \frac{\lambda}{2 \cdot \mathrm{NA}} \\ &= \frac{532\ \mathrm{nm}}{2 \cdot 1.4} \\ &= 190\ \mathrm{nm}\,, \end{aligned}$$

which is very well confirmed by the transversal scan shown in fig. 14.a. The longitudinal resolution of our setup can be extracted from the longitudinal scan shown in figure 14.b and yields a resolution of $\approx 1\ \mu$m. By using more sophisticated optical techniques like the *stimulated emission depletion* (STED) [73] spatial resolutions below the diffraction limit of down to 5.8 nm can be achieved [74].

3.2 OPTICAL SETUP

The experiments were performed with a home-built confocal microscope. A diode-pumped solid-state cw laser with an emission wavelength of 532 nm was used for excitation and readout. We used a *Hanbury Brown–Twiss* [75] interferometer (cf. fig. 15) to determine the occurrence of single NV-centers by measuring a photon-antibunching curve with a fast time-correlation card[1]. The typical time correlation signal of a single emitter is shown in fig. 16.

1 FastComTec P7889

The optical setup is explained in detail in the following. A scheme of the confocal microscope, which was set up and used in the work of this thesis, is shown in fig. 15. The laser has a maximal output power of 100 mW. The beam is passed trough an acousto-optical modulator (AOM) which diffracts the beam by applying a radio-frequency signal to it. The first order of the diffracted beam is used for the experiments while all other orders are blocked by a spatial filter. Here, the AOM acts as an optical switch which provides an extinction ratio of more than 57 dB. To ensure that the cross-section of the beam is of Gaussian shape, before it is focused to the diamond sample, the laser light is guided through a single mode fiber to remove other optical modes. The maximal laser power behind the fiber was $\approx$ 14 mW. We used a beam expander behind the fiber to increase the diameter of the laser beam to fully cover the entrance of the MO[2]. The diameter of the beam is increased up to $\approx$ 2 cm. In front of the MO a dichroic beam splitter [3] is placed. The beam splitter is reflective below 562 nm and transparent above. It is used to separate the excitation light of the laser (532 nm) and the emission from the NV-centers ($>$ 638 nm). The laser beam is passed on to the MO and focused to the diamond sample. We used an oil immersion MO (with NA $= 1.4$) mounted on a nano-positioning system to focus the laser light to the diamond sample. The microscope objective also collects light emitted by the NV-centers during readout. The nano-positioning system has a full traveling range of 70 μm x 70 μm in xy-direction (transveral direction) and 50 μm in z-direction (lateral direction). It has a spatial resolution of 150 pm in transveral direction and 100 pm in lateral direction. The MO is used to focus the excitation light to the sample as well as to collect the emitted photons. Due to the confocal configuration of the setup we can only excite and detect NV-centers in the focal point of the MO. To get a 2D image of the NV-centers in one xy-plane of the diamond crystal, the scanner moves the MO step-by-step transversal and the intensity of photon emission is recorded for every point. The photons, which are emitted into the direction of the MO, are collected, collimated and guided into the direction of the dichroic beam splitter. Since the wavelength of the emitted photons is $>$ 638 nm, they pass through the beam splitter and are guided to the photon-detectors. A lens and a pinhole in front of the detectors are used to achieve a longitudinal selectivity of the microscope, as explained above. A second lens focuses the emitted photons of the NV-centers to two single-photon-counting-modules [4] which are set up as a Hanbury Brown-Twiss interferometer.

2 CZJ Apochromat HI100x/1,40 – 00/0,17-A
3 Semrock: FF562-Di02-25x36
4 PerkinElmer, Single Photon Counting Module, SPCM-AQRH-15

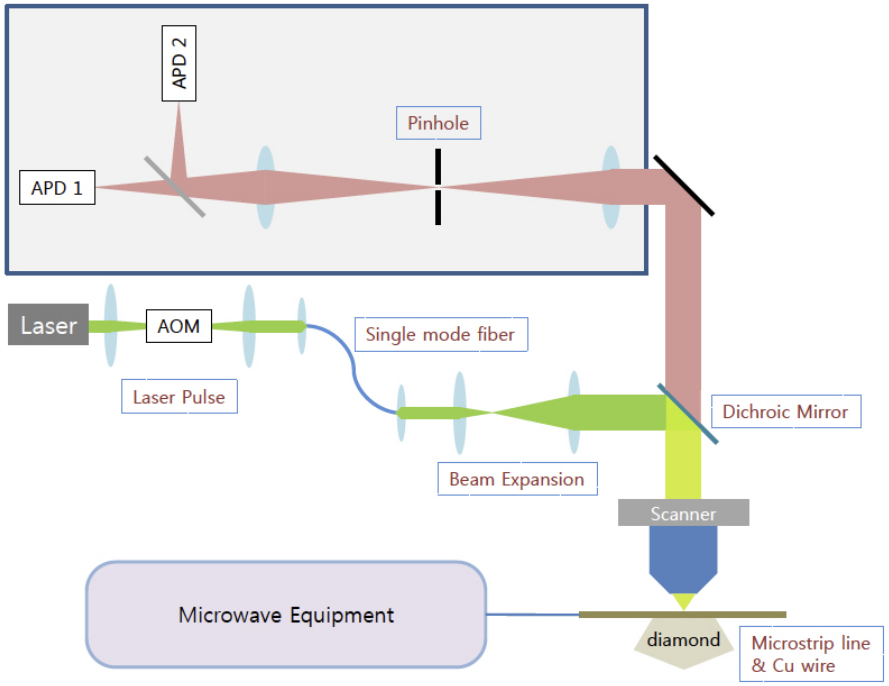

Figure 15: Layout of home-built confocal microscope. In the upper left corner the optical detection setup, which is configured as a *Hanbury Brown–Twiss* interferometer, is shown.

3.2.1 *Anti-Bunching*

Because of the diffraction limited optical resolution, it is possible that more than one NV-center is within the excitation respectively detection spot of the MO. To determine whether there are more than a single emitter in the spot, a *Hanbury Brown–Twiss* [75] interferometer can be used. A scheme of the interferometer is shown in fig. 15. The interferometer consists of a 50/50 beam splitter and two equidistant positioned photon-detectors. The photon-detectors, which are used in our setup, generate a TTL pulse for every detected photon. They have a dark-count rate of 50 counts/s and typically a maximal count rate of $29 \cdot 10^6$ counts/s. Both photon-detectors are connected to a fast-counting-card which has a time resolution of 100 ps. The first photon-detector is connected to the trigger port and is used to start a timer of the fast-counting-card. The second detector is connected to the counting port of the counting-card. The card counts the photons up to a preset time limit. Since only a few photons are emitted and detected for a single run (the photon emission depends among others on the laser intensity and the spontaneous emission rate of the emitter) the measurement has to be repeated multiple times.

The probability of detecting photons at times t and $t + \tau$ is given by the normalized second order correlation function [76]

$$g^{(2)}(\tau) = \frac{\langle I(t)\, I(t+\tau)\rangle}{\langle I(t)\rangle^2}.$$

It is assumed that the average detection intensities for both detectors is equal to $\langle I(t)\rangle$. $I(t)$ and $I(t+\tau)$ are the photon intensities at times t and $t+\tau$. Figure 16 shows an experimental result of an anti-bunching measurement on a single NV-center.

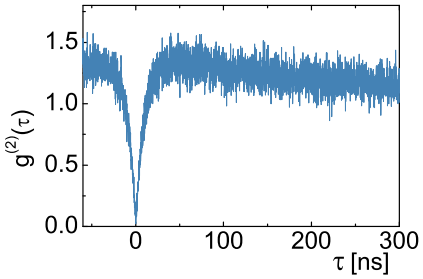

Figure 16: Measurement of the second order correlation function by a photon anti-bunching experiment. To gain the shown signal-to-noise, the measurement was repeated 10^7 times.

The shape of the anti-bunching curve shown in fig. 16 can be explained by a simple model. If a single emitter, which is continuously excited by a laser, relaxes into the its electronic ground state a photon is emitted which might be detected by the first detector. In this case the timer of the fast-counting-card is started and the photons detected by the second photon-detector are counted. Since the emitter is in the ground state at the very first beginning after starting the timer no additional photon can be emitted. It takes some time before the emitter has been excited again and is able to emit a second photon. Thus the probability for detecting a photon instantaneously after the start-trigger is equal to zero, but rises for increasing delay times τ and reaches 1 for long delay times. For short time delays the correlation function in fig. 16 reaches a value of > 1. This is due to the electronic level structure of the NV-center since it is an optical three level system as shown in fig. 3. The anti-bunching curve is given by a double exponential function [77]:

$$g^{(2)}(\tau) = 1 + c_2 e^{-\tau/\tau_2} + c_3 e^{-\tau/\tau_3},$$

with $\tau_{2,3}$ being the relaxation times of the two excited states. The coefficients $c_{2,3}$ depend of the decay times and the relaxation constants, details are given in Ref. [77]. The zero point of the x-axis in fig. 16 was time shifted by adding a delay line into the electronic connection between the second detector and the fast-counting-card to obtain the full shape of the anti-bunching dip.

3.3 ELECTRONIC SETUP

For the excitation of the NV electron spin we used a setup consisting of a microwave synthesizer and an arbitrary waveform generator (AWG), which were connected to a mixer and up-converted. We are able to control the phase as well as the frequency of the up-converted signal by changing the phase and the frequency of the AWG. The microwaves were guided through a Cu wire mounted on the surface of the diamond. We used a permanent magnet to apply a magnetic field to the sample. Unless otherwise mentioned, the orientation of the magnetic field with respect to the axis of the NV-center was not known. Figure 17 shows a scheme of the electronic setup. The numbers mark the different electronic components. The setup will be described in more detail in the following.

The main components of the microwave excitation system are the MW-synthesizer (1) and the arbitrary waveform generator (AWG) (5). The MW synthesizer has a maximum frequency of 3.3 GHz. The AWG has a sampling rate of 4 GS/s and a memory depth of 2 MS[5]. According to the Nyquist theorem the controllable frequency bandwidth by the AWG is < 2 GHz. The electronic setup can be operated in two modes: either in continuous wave (CW) or pulsed excitation. These modes are controlled by the switches (3) and (8). For experiments using CW excitation the output of the synthesizer is directly guided to the power amplifier (9). For pulsed experiments the output of the MW-synthesizer and the AWG are mixed by a double balanced mixer (4). In this case the synthesizer delivers the *carrier-frequency* and is connected to the local oscillator (LO) port of the mixer. The AWG is connected to the intermediate frequency (IF) port of the mixer. We control the phase as well as the frequency of the mixed signal via the AWG. The mixed signal is applied to the RF-port of the mixer and contains both the up-converted ($\omega_{LO} + \omega_{IF}$) and the down-converted ($\omega_{LO} - \omega_{IF}$) signals. The down-converted part is removed from the signal by subsequent filters (6). The overall pass-band of the filters is 2.6 to 3.2 GHz. Excitation with higher respectively lower frequency is possible but the efficiency is reduced. The filtered signal is pre-amplified before it is applied to the power amplifier (9). The maximal output power of the power amplifier is 39 dBm ($\approx$ 8 W). The damping of the microwaves at pulse-off time is < -60 dB with a leakage of microwave power of < 21 dBm. To protect the power amplifier from reflections at the sample due to impedance mismatches, an isolator (10) is connected at the amplifier's output. For diagnostic purposes a bi-direction coupler (11) is mounted between sample (14) and isolator (10). In pulsed mode the forward coupled (CPL-FWD) port is used to

5 In a prior version of the setup we also had an AWG with 2 GS/s sampling rate available for testing purposes which has been used for the measurements in chapter 5.1.

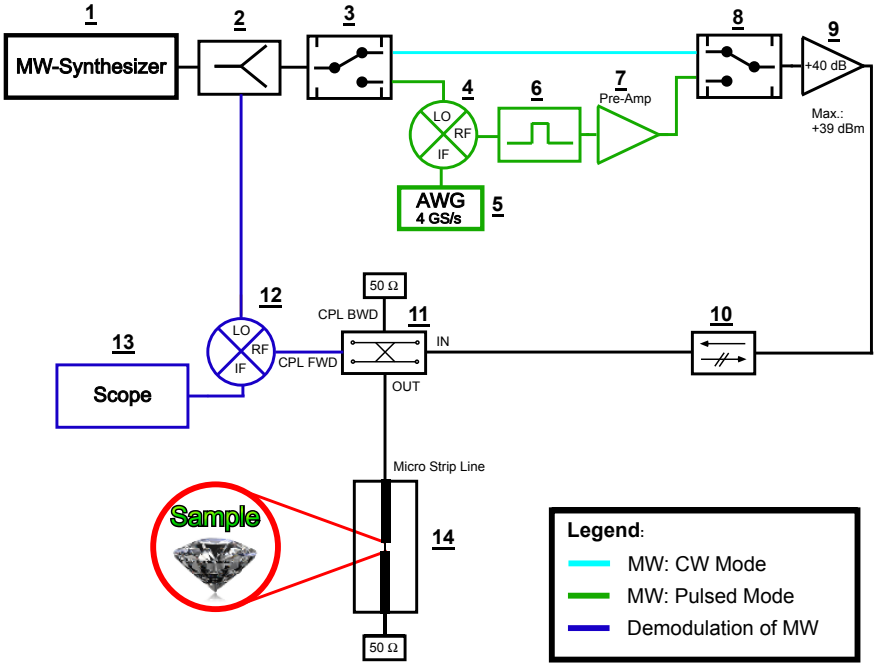

Figure 17: Schematic diagram of electronic setup.

visualize the applied pulses on an oscilloscope. Thus the CPL-FWD port is connected to the RF-port of a second mixer (12). The carrier-frequency signal, which follows from the power splitter (2), is connected to the LO-port . The IF port of the second mixer, which contains the down converted signal, is connected to the oscilloscope (13). The backward port of the bi-direction coupler is terminated by 50 Ω, but can be used to determine the level of the excitation power which is reflected at the micro-strip-line (14). To attach the diamond sample to the micro-strip-line, which was matched to an impedance of 50 Ω, a hole was drilled trough the micro-strip-line. Subsequently the diamond was glued into the hole, and a copper wire of 20 μm diameter covering the diamond sample was soldered to the micro-strip-line. Since the penetration of the strip-line due to the hole, the impedance changes and does not match exactly 50 Ω anymore. Thus the MW pulses are partly reflected and the efficiency of the excitation is reduced. Here, $\approx$ 20 % of the excitation power is reflected. Depending on the sample and the distance between wire and NV-center a maximal Rabi frequencies of $\approx$ 40 MHz was measured with this setup.

3.4 SPATIAL STABILITY

During our experiments it turned out that thermal stability of the setup as well as the environment and the laboratory is a crucial issue. Since the durations of our measurements sometimes take more

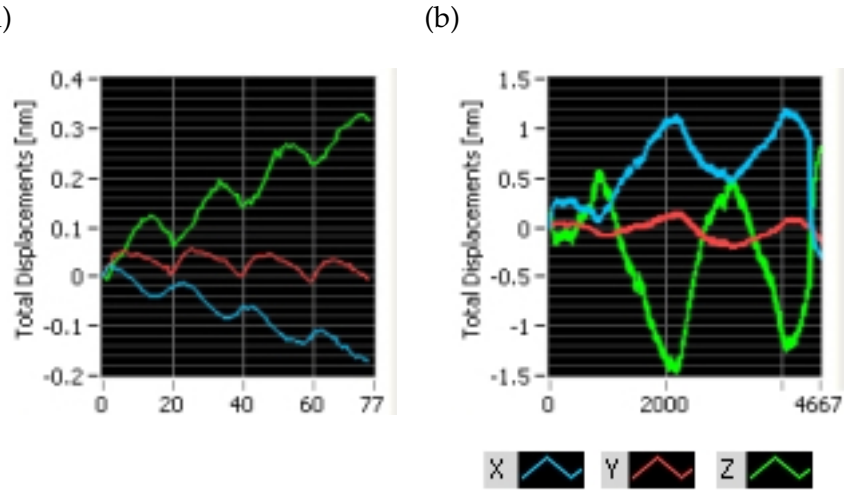

Figure 18: Spatial drift of NV-center due to thermal fluctuations: a) Short time drift and b) long time drift. The x-axis gives the number of refocusing. The refocusing period was 40 s. The legend at the lower right assigns the colors to the corresponding lab axes.

than a day, fluctuations of the temperature in the lab of several degrees of Celsius are possible. The temperature fluctuations cause a displacement of the MO's focal point and the sample. The spatial drift of a NV-center can be traced by continuously refocusing the MO to the point of maximal emission. In fig. 18.a the displacement of a short time tracing and in fig. 18.b of a long time tracing are shown. The y-axis shows the displacement along the x-, y- and z-axis. The x-axis gives the number of refocusing with a refocusing period of 40 s. The short time tracing (fig. 18.a) shows periodic modulations which are in the order of ~ 100 nm. It turned out that these are attributed to the air condition system of the lab which causes a short time temperature modulation of the order $\sim \pm 0.05$ °C. This was measured with a PT1000 temperature sensor in a four-point measurement. Most of the opto-mechanical components in the optical setup are made of aluminum which has a thermal expansion coefficient of $\alpha = 23.8 \cdot 10^{-6}/K$ [78], with α being defined by:

$$\alpha = \frac{1}{L_0}\frac{dL}{dT}.$$

For a typical length of $L_0 = 10$ cm of aluminum elements used in our setup a temperature modulation of $\Delta T = \pm 0.05$ °C causes a change in length of $\Delta L \approx \alpha \cdot L_0 \cdot \Delta T = \pm 119$ nm. Due to the refocusing of the NV-center this displacement can be compensated, but it is still a problem which has to be taken into account especially for long measurements.

4

CHIRPED RAMSEY

BROADBAND EXCITATION OF ELECTRON SPINS BY CHIRPED PULSES: APPLICATION TO SINGLE NV-CENTERS IN DIAMOND

Quantum computing with NV-centers can not only use the electron spin, but also hybrid quantum registers with additional nuclear spins. In particular, strongly coupled ^{13}C nuclear spins have attractive properties [11, 12, 79, 13, 42]. The strength of the hyperfine interaction depends on the position of the nuclear spin [42, 43] and reaches a maximum of 130 MHz for a ^{13}C in a nearest-neighbor lattice site [7, 39]. Measuring these couplings requires the recording of spectra that cover a frequency range larger than the sum of all hyperfine coupling constants. This can be done by CW-ODMR, which yields spectra with linewidths of several MHz under typical conditions. These linewidths are the result of power broadening by the laser and the microwave field. The effect of the laser is eliminated in the pulsed ODMR approach [80, 42], where the laser is switched off during the application of the microwave field. The remaining broadening from the microwave field is also eliminated in the Ramsey experiment [81, 82], which yields spectra with linewidths equal to the natural linewidth. The drawback of the Ramsey experiment is that it requires excitation pulses that cover the full bandwidth of the spectrum. This can be challenging for spectra with large hyperfine couplings.

Here, we present an experimental scheme that avoids power broadening by using the Ramsey approach of free precession and the requirement of strong microwave fields by using excitation pulses that cover the full bandwidth with very low power. Compared to the pulsed ODMR approach, this method does not suffer from a trade-off between signal intensity and resolution. We achieve this by scanning the frequency over the full spectral range. This type of pulses are known as chirped pulses [46, 47, 48].

Since the microwave field interacts with the different transitions sequentially, it excites not only the usual, magnetic-dipole allowed transitions between the $|m_S = 0\rangle \leftrightarrow |m_S = \pm 1\rangle$ states (single-quantum transitions), but also the 'forbidden' transition between the $|m_S = -1\rangle \leftrightarrow |m_S = +1\rangle$ states (double-quantum transition). These different types of transitions can be distinguished by appropriate shifts in the relative phases of the excitation and readout pulses. Some part of this section has been published in Ref. [22].

4.1 MATHEMATICAL DESCRIPTIONS

4.1.1 *Spin S=1/2 System*

We use chirped excitation pulses to excite transitions in a large frequency range. Figure 19 shows the basic idea: Assuming that we want to excite the transition between the $|m_S = 0\rangle$ and the $|m_S = 1\rangle$ state and that the system is initially in the ground state, we scan the frequency through resonance in such a way that the system has a 50 % transition probability to the $|m_S = 1\rangle$ state and ends up in the superposition state

$$\Phi_1 = \frac{1}{\sqrt{2}}\left(e^{-i\varphi_1/2}|0\rangle + e^{i\varphi_1/2}|1\rangle\right),$$

which maximizes the coherence between the two levels. To reach this state, the sweep must be non-adiabatic. The conditions for this are discussed in section 4.1.3. The relative phase φ depends on the phase, amplitude and scan rate of the microwave.

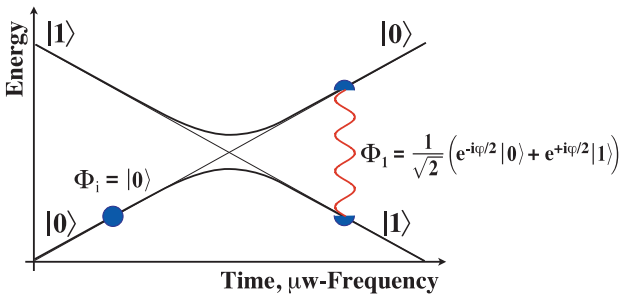

Figure 19: Excitation of a two-level system by non-adiabatic rapid passage. For an adiabatic passage the initial and final states of the system are equal to the non-perturbed eigenstate ($|0\rangle$, $|1\rangle$). After a non-adiabatic passage, the final state is a coherent superposition of the eigenstates $|0\rangle$ and $|1\rangle$. The conditions for the adiabaticity of a passage are discussed in section 4.1.3.

The effect of the chirped pulse can thus be described by an unitary operator [48]

$$U_{zy}\left(\varphi_1, \frac{\pi}{2}\right) = e^{-i\varphi_1 S_z} e^{-i\frac{\pi}{2}S_y}.$$

As shown in figure 20, the system is then allowed to evolve freely for a time t_1. If Ω_0 is the Larmor frequency of the system, the superposition state acquires an additional phase $\Omega_0 t_1$ during this time. The resulting state is

$$\begin{aligned}\Phi_2 &= e^{-i\Omega_0 t_1 S_z}\Phi_1 \\ &= \frac{1}{\sqrt{2}}\left(e^{-i(\Omega_0 t_1+\varphi_1)/2}|0\rangle + e^{i(\Omega_0 t_1+\varphi_1)/2}|1\rangle\right).\end{aligned}$$

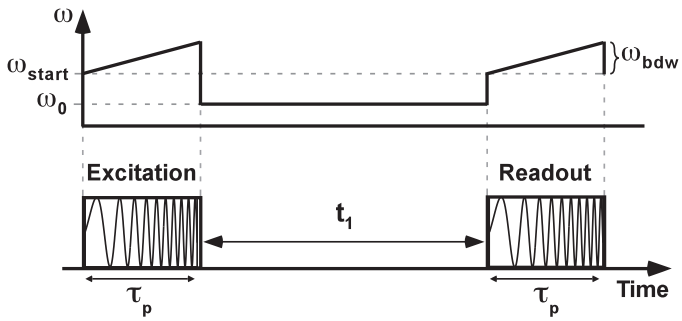

Figure 20: Pulse sequence for broadband Ramsey experiment with chirped excitation pulses. ω_{start} defines the start frequency of the scan and ω_{bdw} the width of the scan. ω_0 is the reference frequency that relates the phase of the two pulses; for details see text. τ_p is the pulse duration and t_1 the free evolution time which is incremented between experiments.

At this point, a second chirped pulse generates another transformation that we write as

$$U_{yz}\left(\frac{\pi}{2}, \varphi_2\right) = e^{-i\frac{\pi}{2}S_y} e^{-i\varphi_2 S_z},$$

thus converting the system into the final state

$$\begin{aligned}\Phi_3 &= i\sin\left(\frac{\Omega_0 t_1 + \varphi_1 + \varphi_2}{2}\right)|0\rangle \\ &\quad + \cos\left(\frac{\Omega_0 t_1 + \varphi_1 + \varphi_2}{2}\right)|1\rangle\end{aligned}$$

The population of the ground/bright state $|0\rangle$ is thus

$$\begin{aligned}P(|0\rangle) &= \left[\sin\left(\frac{\Omega_0 t_1 + \varphi_1 + \varphi_2}{2}\right)\right]^2 \\ &= \frac{1}{2}\left[1 - \cos\left(\Omega_0 t_1 + \varphi_1 + \varphi_2\right)\right].\end{aligned}$$

Clearly, this corresponds to a Ramsey-fringe pattern, which can be Fourier-transformed to obtain the spectrum (a single line at Ω_0 in this case).

4.1.2 *Spin S=1 System*

The NV-center in diamond is an electron spin $S = 1$ system. In this section, we neglect the nuclear spins and write the relevant Hamiltonian

$$\mathcal{H} = DS_z^2 + \Omega_0 S_z. \tag{15}$$

Here, $D = 2.8$ GHz is the zero-field splitting and Ω_0 the Larmor frequency due to the interaction with the magnetic field. Figure 5

(cf. section 2.5.2 on page 17) shows the resulting level structure. We write $|m_S\rangle$ for the eigenstates of the Hamiltonian, where m_S is the eigenvalue of S_z.

In the following, we assume that the Rabi frequency is small compared with the frequency separation of the relevant transitions. We therefore can assume that the microwave field drives only one transition at a time [46, 47, 48]. If we scan from low to high frequency, we first excite the transition $|0\rangle \leftrightarrow |+1\rangle$ in the system shown in fig. 5. Starting from the initial state $\Psi_0 = |0\rangle$, the first passage through resonance converts it into

$$\begin{aligned}\Psi_1 &= U_{zy}(\varphi,\theta)\,|0\rangle \\ &= e^{i\varphi/2}\cos\frac{\theta}{2}\,|0\rangle - e^{-i\varphi/2}\sin\frac{\theta}{2}\,|+1\rangle\,,\end{aligned}$$

where θ is the effective flip-angle of the pulse. Passing through the second resonance, we obtain

$$\begin{aligned}\Psi_2 &= U_{zy}(\varphi,\theta)\,\Psi_1 \\ &= -\sin\frac{\theta}{2}\cos\frac{\theta}{2}\,|-1\rangle - e^{-i\varphi/2}\sin\frac{\theta}{2}\,|+1\rangle \\ &\quad + e^{i\varphi}\cos^2\frac{\theta}{2}\,|0\rangle\,.\end{aligned}$$

Here, we have assumed that the effect of the pulse on both transitions is the same. This is a good approximation if the scan rate and the transition strengths are the same.

During the subsequent free evolution period, the system evolves to

$$\begin{aligned}\Psi_3 &= U_z(t_1)\,\Psi_2 \\ &= -e^{-i(\Omega_{-1}t_1)}\sin\frac{\theta}{2}\cos\frac{\theta}{2}\,|-1\rangle \\ &\quad -e^{-i(\Omega_{+1}t_1+\varphi/2)}\sin\frac{\theta}{2}\,|+1\rangle + e^{i\varphi}\cos^2\frac{\theta}{2}\,|0\rangle\,,\end{aligned}$$

with $\Omega_{\pm1} = D \mp \Omega_0$ representing the resonance frequencies of the two transitions.

This free precession period is terminated by the readout pulse, which is identical to the excitation pulse (apart from an overall phase). It converts part of the coherences back to populations:

$$\begin{aligned}\Psi_4 &= U_{yz}(\theta,\varphi)\,\Psi_3 \\ &= B_{-1}\,|-1\rangle + B_{+1}\,|+1\rangle \\ &\quad + \left[-A_1\left(e^{-i\left(\Omega_{-1}t_1+\frac{\varphi}{2}\right)} + e^{-i\left(\Omega_{+1}t_1+\frac{\varphi}{2}\right)}\right) + A_2 e^{i2\varphi}\right]|0\rangle\ .\end{aligned}$$

The coefficients B_{-1} and B_{+1} are not given here since we are interested only in the population $P_0 = P(|0\rangle)$ of the bright state $|0\rangle$:

$$\begin{aligned} P_0 &= \left| A_1 \left(e^{-i\left(\Omega_{-1} t_1 + \frac{\varphi}{2}\right)} + e^{-i\left(\Omega_{+1} t_1 + \frac{\varphi}{2}\right)} \right) + A_2 e^{i2\varphi} \right|^2 \\ &= 2A_1^2 + A_2^2 \\ &+ 2A_1^2 \cos\left(\left[\Omega_{+1} - \Omega_{-1}\right] t_1\right) \\ &+ 2A_1 A_2 \left[\cos\left(\Omega_{+1} t_1 + \frac{5\varphi}{2}\right) + \cos\left(\Omega_{-1} t_1 + \frac{5\varphi}{2}\right) \right], \end{aligned}$$

with the amplitudes

$$A_1 = \sin^2 \frac{\theta}{2} \cos \frac{\theta}{2} \quad , \quad A_2 = \cos^4 \frac{\theta}{2}.$$

The first term in this expression is a constant offset. The second term oscillates at the frequency $2\Omega_0 = \Omega_{-1} - \Omega_{+1}$ of the $|-1\rangle \leftrightarrow |+1\rangle$ transition, while the third term contains the two single-quantum transition frequencies. Fourier transformation of this will therefore yield a spectrum with the two allowed single-quantum transitions and the 'forbidden' double-quantum transition frequency, as shown in figure 5. Note that the frequencies in the figure are not the true resonance frequencies. The relation between the apparent and the real frequencies will be discussed in section 4.2.

4.1.3 *Adiabatic Condition*

Adiabatic pulses can be used to invert the populations of two states (cf., e.g. [83]). Here, we use chirped pulses in the non-adiabatic regime to create coherences of many transitions distributed over a broad frequency range. The adiabaticity of a scan can be quantified by the adiabaticity parameter [84]

$$Q(t) = \frac{\omega_{eff}(t)}{|d\theta/dt|}.$$

Here, $\omega_{\mathrm{eff}}(t)$ is the effective magnetic field in the frame rotating with the frequency of the microwave field and $d\theta/dt$ indicates the rate of change of the instantaneous eigenstates. Close to resonance, $\omega_{eff}(t)$ is minimal and equal to the Rabi frequency while $d\theta/dt$ reaches a maximum. Hence the adiabaticity factor becomes minimal and can be written as: $Q_{min} = 2\pi\nu_1^2 t_p/\Delta f$ [85]. ν_1 is the Rabi frequency, t_p the duration of the chirp and Δf the chirp bandwidth. An adiabatic transfer is achieved if $Q_{min} \gg 1$. The condition for an adiabatic transfer is thus that the rate $d\theta/dt$ at which the eigenstates change be small compared to the Rabi frequency ν_1. In our experiments the transfer must be diabatic, which can be achieved by choosing $d\theta/dt > \nu_1$. We used Rabi frequencies < 30 MHz, pulse durations of $50 - 120$ ns and chirp bandwidths of 250 MHz - 500 MHz. The maximal value of the adiabaticity parameter used in the measurements was $Q_{min} < 0.5$. This underlines that the excitations within our experiments were non-adiabatic.

4.2 EXPERIMENTAL RESULTS

In this section we give a short introduction into the experimental procedure and the samples used. Then we present experimental results that demonstrate how the experimental parameters have to be chosen to optimize the information content of the resulting spectra. In addition, we present experimental data from a system that requires a large excitation bandwidth and contains a large number of resonance lines.

The experiments were carried out as follows: For each point of t_1 the frequency of the pulse was swept from ω_{start} up to the final frequency $\omega_{start} + \omega_{bdw}$. A free evolution period of duration t_1 followed the first MW-pulse. The second pulse was identical to the first up to a phase as discussed in section 3.2. As in conventional Ramsey experiments the time increment of the free evolution period t_1 defines the detection bandwidth and the total duration of the free evolution respectively the maximal value of t_1 defines the spectral resolution. To avoid aliasing effects, we chose the chirp and detection bandwidth equal. The measured time-domain signal was Fourier transformed to recover the spectrum.

We applied the chirped Ramsey sequence shown in figure 20 to the two diamond samples which were introduced in section 2.2 on page 6. The NV-center of the ^{12}C enriched diamond had a relaxation time of $T_2^* > 200\ \mu s$ and the natural abundance diamond $T_2^* \approx 1\ \mu s$. For the enriched sample the relaxation time was determined by a conventional Ramsey measurement, for the natural abundance T_2^* was taken from the chirped measurement.

We first present measurements of the enriched sample to illustrate different features of this experiment, in particular how the phases of the excitation pulses affect the observed frequency and phase of the different types of resonance lines. Since we discuss Fourier transformed time-domain signals of photon counts, we use arbitrary units and omit the y-axes in the spectra presented in the following. The pulse durations used in our experiments were chosen with respect to a series of measurements of different pulse lengths which were done for one of the NV-centers of the enriched sample. We chose the pulse duration that yielded the maximum signal for single as well as double-quantum coherence. For the other NV-centers the parameters were chosen accordingly to gain similar values for the adiabaticity factor Q_{min}.

4.2.1 *Optimization of Pulse Duration*

To optimize the duration of the chirp pulses, a series of chirped Ramsey experiments with increasing durations of the excitation and readout pulses were performed. As can be seen in fig. 21 for short pulse

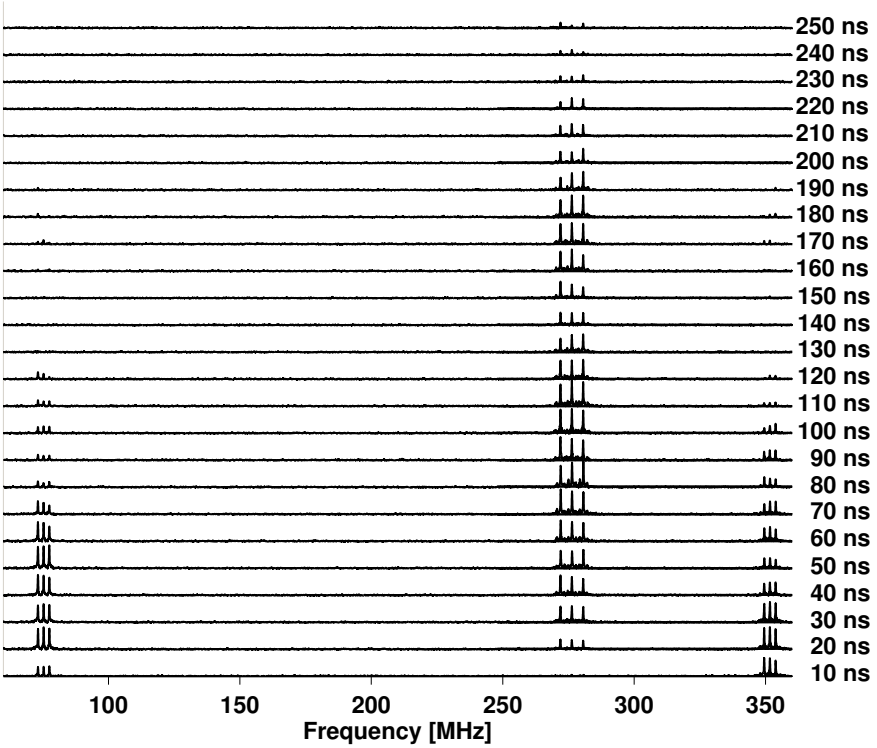

Figure 21: Optimization of pulse duration: Series of Ramsey measurements to find the optimal pulse duration which creates single as well as double-quantum coherences. The triplets to the left and right are single-quantum coherences and the central triplets are double-quantum coherences. The numbers on the right side are the pulse durations which have been used in the measurement of the corresponding spectra.

durations, mainly single-quantum coherences are created. With increasing pulse durations peaks, corresponding to single as well as double-quantum coherences, appear in the spectra. If the pulse durations are further increased, the intensities of single-quantum coherences start to decrease while the double-quantum coherences stay constant. For pulse durations $>$ 200 ns the double-quantum coherences decrease as well. The measurements were performed with a single NV-center in the enriched sample. The chirp bandwidth was $\omega_{bdw} = 500$ MHz and started at $\omega_{start} = 2650.8$ MHz. The detection bandwidth was equal to the chirp bandwidth and the maximal duration of the free evolution was $t_1 = 5\ \mu$s. The number of accumulations per trace was $2 \cdot 10^5$. The reference frequency was detuned by $+20$ MHz.

In the measurements presented in sections 4.2.4 and 4.2.3, which were performed on the same NV-center, we used a pulse duration of $\tau_p = 50$ ns since in this case the spectrum contains single as well as double-quantum coherences of reasonable intensities. The Rabi frequencies of the single-quantum transitions were 27.3 MHz (leftmost

triplet) and 21.7 MHz (rightmost triplet) thus the adiabaticity factor was $Q_{min} \approx 0.47$. We used this value as a guideline for the measurements with other NV-centers (cf. sections 4.2.2, 4.2.5 and 4.2.6).

The intensities of the single- and double-quantum coherences in fig. 21 show oscillations of small amplitude with minima at: 80 ns (left triplet), 140 ns (central triplet) and 50 ns (right triplet). Their origin is not clear.

4.2.2 *Reference Frequency*

In the experiments we are not interested in the dc component $2A_1^2 + A_2^2$, which we omit in the following. We now compare experiments where we change the phase of the second pulse with respect to that of the first one by an angle α. The resulting signal is then

$$\begin{aligned} s &= 2A_1^2 \cdot \cos\left(\left[\Omega_{+1} - \Omega_{-1}\right] t_1\right) \\ &\quad + 2A_1 A_2 \left[\sin\left(\Omega_{-1} t_1 + \frac{5}{2}\varphi - \alpha\right)\right. \\ &\quad \left. + \sin\left(\Omega_{+1} t_1 + \frac{5}{2}\varphi - \alpha\right)\right] \end{aligned} \tag{16}$$

We use this additional phase for two purposes: we increment it linearly with the free precession period t_1 to shift the effective precession frequency, and we use it to distinguish the double-quantum transitions, which do not depend on α, from the single-quantum transitions.

Looking first at the linear phase increments, we set $\alpha = \omega_0 t_1$. The resulting signal is then

$$\begin{aligned} s_1 &= 2A_1^2 \cdot \cos\left(\left[\Omega_{+1} - \Omega_{-1}\right] t_1\right) \\ &\quad + 2A_1 A_2 \left[\sin\left(\left(\Omega_{-1} - \omega_0\right) t_1 + \frac{5}{2}\varphi\right)\right. \\ &\quad \left. + \sin\left(\left(\Omega_{+1} - \omega_0\right) t_1 + \frac{5}{2}\varphi\right)\right]. \end{aligned}$$

We therefore expect that the single-quantum transitions appear shifted to the frequencies $(\Omega_{\pm 1} - \omega_0)$, while the double-quantum transitions remain at the natural frequency $2\Omega_0 = \Omega_{+1} - \Omega_{-1}$. This is clearly borne out in figure 22, where we compare spectra obtained with the same excitation scheme, but different reference frequencies. The three groups of lines appear centered around $\Omega_{+1} - \omega_0$, $2\Omega_0 = \Omega_{+1} - \Omega_{-1}$, and $\Omega_{-1} - \omega_0$. For these experiments, we chose ω_0 such that the resulting frequencies fall into a frequency window that is easily accessible. In the case of the spectra shown here, we incremented t_1 by 2 ns between scans, which yields, according to the Nyquist theorem, a 250 MHz frequency window. The maximum value of t_1 was

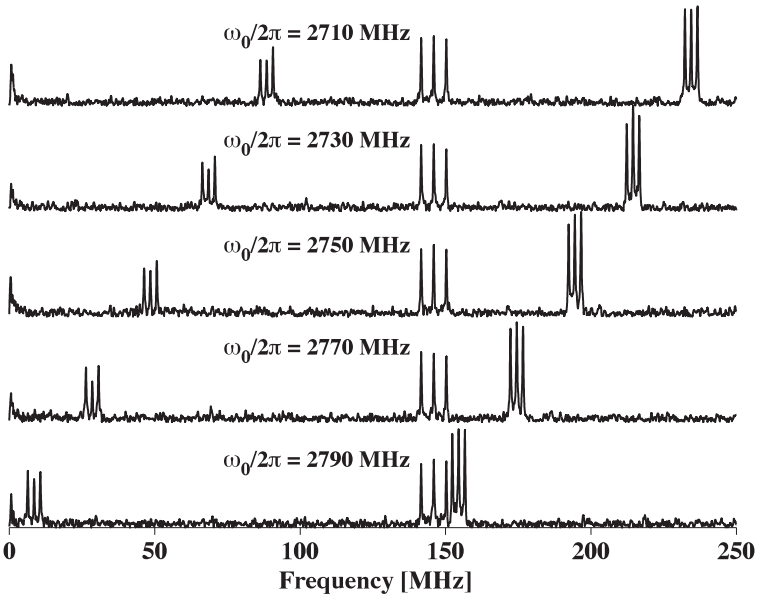

Figure 22: Ramsey spectra measured with different reference frequencies. The actual transition frequencies are: $\Omega_{+1}/2\pi = 2798.5$ MHz, $\Omega_{-1}/2\pi = 2944.5$ MHz and $2\Omega_0/2\pi = 146$ MHz. The reference frequencies are given in the figure. For all spectra, the start frequency of the chirp was $\omega_{start} = 2770$ MHz and the chirp bandwidth $\omega_{bdw} = 250$ MHz.

5 μs. The Rabi frequencies of the single-quantum transitions were 10.5 MHz (leftmost triplet) and 11.1 MHz (rightmost triplet). The number of accumulations was $2 \cdot 10^5$. The data were recorded in the same magnetic field, which splits the $|m_s = \pm 1\rangle$ lines by 146 MHz. All measurements were done with frequency chirps starting at 2770 MHz and the pulse lengths were τ_p = 120 ns. It is clearly seen that the single-quantum transitions are shifted in the opposite direction from the reference frequency, while the double-quantum transitions (at 146 MHz) are not affected by the detuning.

4.2.3 *Phase Shifts*

Instead of incrementing the phase proportionally with t_1, we can also compare two spectra with different constant phase shifts of the readout pulse. The two traces of figure 23.b show an example: the spectra were obtained with phase shifts of 0 and π between the two pulses; only expanded regions of the full spectrum shown in figure 23 .a are shown. These data were recorded with a different NV-center in a higher magnetic field strength. The Rabi frequencies of the single-quantum transitions were 27.3 MHz (leftmost triplet) and 21.7 MHz (rightmost triplet). The number of accumulations was $4 \cdot 10^5$. The differences in intensity of the single-quantum coherences might be due to a frequency dependence of the pulse power. The chirp bandwidth

was 500 MHz and the pulse duration $\tau_p = 50$ ns. The detection bandwidth was 500 MHz and the maximum value of t_1 was 5 μs.

According to equation (16), we expect that the phase of the single-quantum transitions $|0\rangle \leftrightarrow |\pm 1\rangle$ should change with α, while the double-quantum transition $|+1\rangle \leftrightarrow |-1\rangle$ should not change. Inspection of the experimental data shows that the spectral lines close to 60 and 375 MHz are inverted between the two spectra, while the signals close to 315 MHz do not change. We therefore interpret the outer lines as single-quantum transitions, the inner ones as double-quantum transitions. This assignment is also consistent with the splittings due to the hyperfine interaction with the ^{14}N nuclear spin, which is 2.15 MHz for the single-quantum transitions and 4.3 MHz for the double-quantum transition.

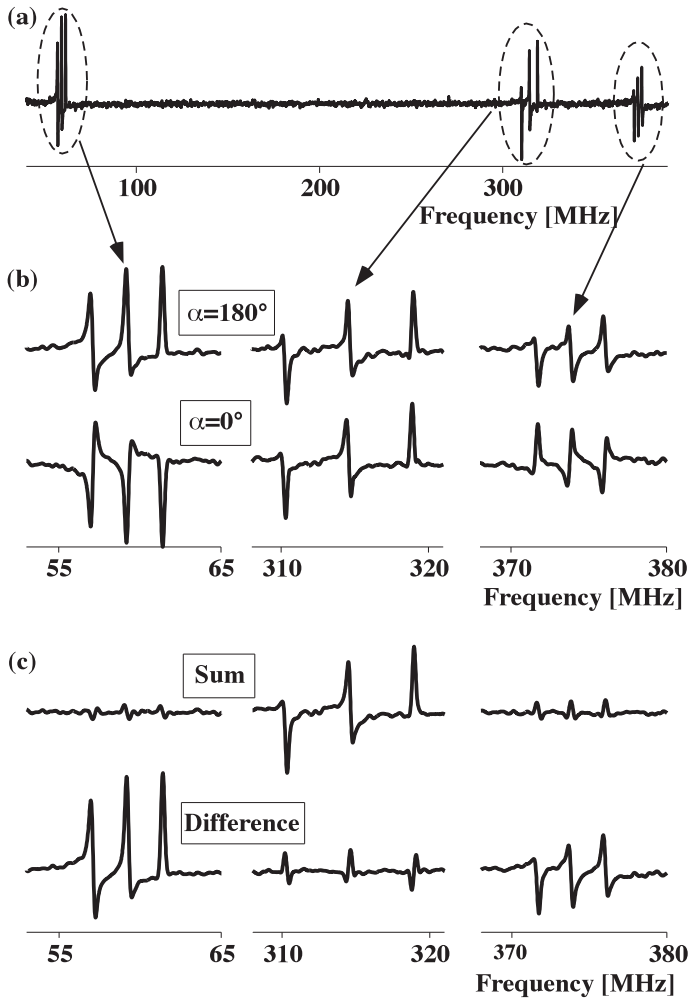

Figure 23: Phase-sensitive spectra of two chirped Ramsey measurements. (a) Full spectrum. (b) Real parts of spectra obtained with phase shifts $\alpha = 180°$ (top) and $\alpha = 0°$ (bottom). (c) Sum (top) and difference (bottom) of the spectra in (b).

Using this phase dependence, we can also separate the two types of transitions by calculating the sum and difference of the two spectra. According to Eq. (16) the difference of the two spectra should be

$$\begin{aligned} s_{\alpha=0^\circ} - s_{\alpha=180^\circ} &= 4A_1A_2 \left[\sin\left(\Omega_{-1}t_1 + \frac{5}{2}\varphi\right) \right. \\ &\quad \left. + \sin\left(\Omega_{+1}t_1 + \frac{5}{2}\varphi\right) \right], \end{aligned} \tag{17}$$

and the sum

$$s_{\alpha=0^\circ} + s_{\alpha=180^\circ} = 4A_1^2 \cdot \cos\left(2\Omega_0 t_1\right). \tag{18}$$

The lower part of fig. 23 shows the result of this operation: The sum (upper trace) contains mostly the double-quantum signals, while the difference is dominated by the single-quantum transitions which corresponds to the results of Eq. (17) and (18). The incomplete suppression of the other signals can be attributed to instabilities in the experimental setup, which result in thermal frequency shifts and changing amplitudes.

4.2.4 *B-Field Dependence*

Figure 24 shows spectra of the ^{12}C enriched crystal for different magnetic field strengths. For these measurements the reference frequency was $\omega_0 = 2670.8$ MHz. The start frequency of the chirp was $\omega_{start} = 2650.8$ MHz, the chirp bandwidth $\omega_{bdw} = 500$ MHz and the pulse duration $\tau_p = 50$ ns. The sampling interval of 1 ns results in a detection bandwidth of 500 MHz and maximum value of t_1 of 5 μs yields a digital frequency resolution of 100 kHz.

In each spectrum of the figure we list the splitting between the single-quantum transitions, which corresponds to the magnetic field component along the symmetry axis of the center, measured in frequency units. The outer triplets correspond to the single-quantum transitions ($|0\rangle \leftrightarrow |\pm 1\rangle$), the inner lines to the double-quantum transition ($|+1\rangle \leftrightarrow |-1\rangle$). With increasing magnetic field strength, the splitting between the single-quantum transitions increases proportionally and is always equal to the frequency of the double-quantum transition. The frequencies of the single-quantum transitions do not change symmetrically. The mean values of the central lines of the single-quantum transitions are: $(\Omega_+ + \Omega_-)/2 = 205$, 213 and 216 MHz. This variation is due to non-secular terms of the Zeeman interaction (i.e. $S_xB_x + S_yB_y$) which we have neglected in the Hamiltonian in Eq. (15).

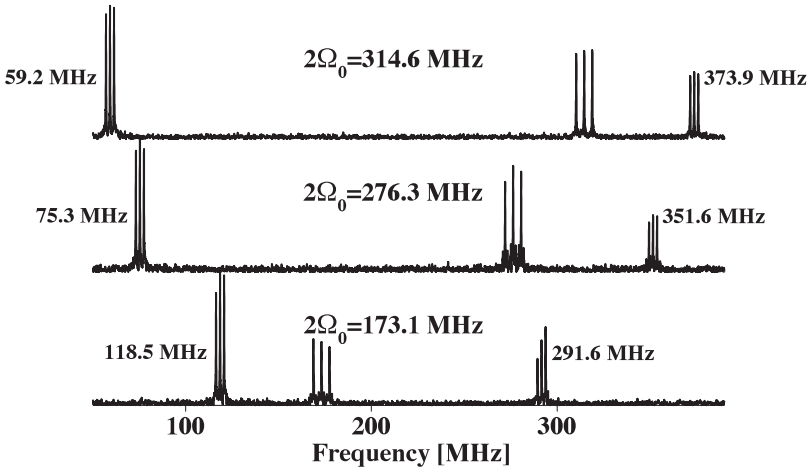

Figure 24: Absolute value spectra for different magnetic field strengths. $2\Omega_0$ corresponds to the separation of the $|+1\rangle$, $|-1\rangle$ levels and therefore to the separation between the two single-quantum transitions and to the center frequency of the double-quantum transitions (inner line of the triplet). The frequency values give the positions of the central line of the respective triplet. The Rabi frequencies and number of accumulations are identical to those in section 4.2.3.

4.2.5 *Multi-Line Broadband Spectrum ('low-field')*

The chirped excitation scheme is particularly useful when the spectra cover a broad frequency range with many resonance lines. Such a situation exists in NV-centers with a ^{13}C nuclear spin in the first coordination shell.

Figure 25 shows the spectrum of such a center. In this particular center, the electron spin is coupled to a nearest-neighbor ^{13}C nuclear spin with a hyperfine coupling constant $A_{\parallel} \approx 126.5$ MHz as well as to an additional ^{13}C with a coupling constant of $A_{\parallel} \approx 6.55$ MHz. For this measurement we used a type IIa natural abundance diamond and applied a magnetic field of $\approx$ 9 G. The field was not aligned and had an angle of $\approx 65°$ with respect to the symmetry axis of the NV-center, which corresponded to a projected field strength of 3.7 G. The chirp bandwidth was $\omega_{bdw} = 250$ MHz, starting from $\omega_{start} = 2750.3$ MHz and the pulse-duration was $\tau_p = 60$ ns. The detection bandwidth was 250 MHz and the maximum value of $t_1 = 3\ \mu$s. The number of accumulations was $2.36 \cdot 10^7$.

The top graph of figure 25 shows the absolute value of a chirped Ramsey spectrum. The center graph shows the sum and the lower the difference of two phase-shifted spectra, which correspond to the double- and single-quantum transitions, respectively. The line at 126.5 MHz in b) is a zero-quantum transition. Its transition frequency matches the hyperfine coupling constant of the nearest-neighbor ^{13}C. In the

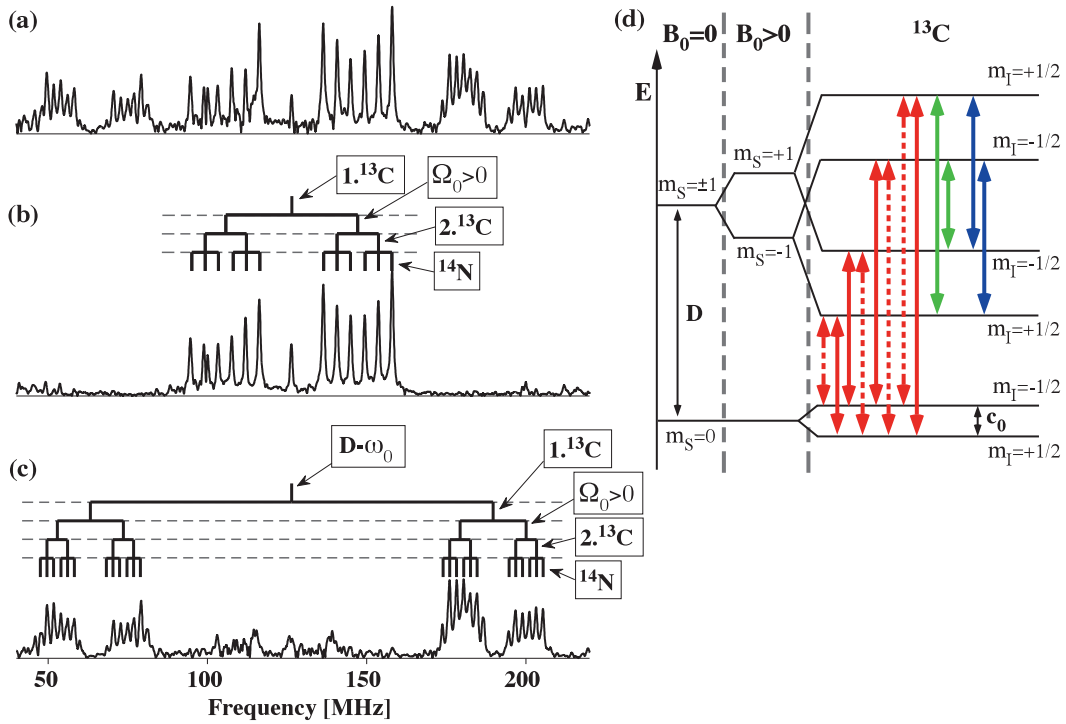

Figure 25: Spectra of NV-center in natural abundance diamond with two adjacent ^{13}C nuclear spins. One strongly coupled with $A_{\parallel} \approx 126.5$ MHz (nearest-neighbor) and one with $A_{\parallel} \approx 6.55$ MHz [42]. $\Omega_0 \approx 10$ MHz is the Zeeman interaction, D the zero-field splitting and ω_0 the reference frequency. (a) Absolute value spectrum. (b) Sum and (c) difference of the spectra obtained with phase shifts $\alpha = 0°$ and $\alpha = 180°$. (d) Energy level scheme of the NV electron spin coupled to a nearest-neighbor ^{13}C within a small external magnetic field $B_0 > 0$. c_0 indicates a splitting of the electron spin ground state due to the coupling to the ^{13}C nuclear spin. For the sake of simplicity we have omitted the couplings to the ^{14}N nuclear spin and the additional ^{13}C.

spectra, we also indicate how the spectral lines can be assigned to transitions of the electron spin with different configurations of the three coupled nuclear spins. If we consider only the Hamiltonian of Eq. (15) for the electron spin and the hyperfine interactions with the nuclear spins, the single-quantum spectrum (bottom of figure 25) should consist of 4 groups of six lines. In the experimental spectrum the four groups contain more than six lines. This difference can be attributed to the splitting of the $|m_S = 0\rangle$ ground state due to the interaction with the transverse components of the magnetic field and the nonsecular hyperfine interaction. Figure 25.d shows a level scheme, which takes into account that the nonsecular terms of the hyperfine interaction lift the degeneracy of the two spin states of the ^{13}C nuclear spin associated with the $|m_S = 0\rangle$ state [41]. The solid *red* arrows indicate allowed single-quantum transitions and the dashed red

arrows indicate 'forbidden' single-quantum transitions, where both spins, the nuclear *and* electron, flip. The *green* arrows indicate double-quantum transitions and the *blue* arrows zero-quantum transitions.

As a result of the nonsecular terms in the hyperfine interaction, the electronic and nuclear spin degrees of freedom do not factorize and a microwave field can drive transitions between any pair of states whose energy difference matches the resonance condition, including 'forbidden' transitions. Throughout the scan, the resonance condition becomes fulfilled for different connected transitions and the field thereby generates also coherences between states whose energy difference does not match the microwave frequency. As discussed in section 4.1.2, this leads to the excitation of double-quantum coherence and in a similar way to the excitation of zero-quantum coherence between the $|m_S = \pm 1, \uparrow\rangle$ and $|m_S = \pm 1, \downarrow\rangle$ states (cf. fig. 25.b).

4.2.6 *Multi-Line Broadband Spectrum ('high-field')*

We performed an additional chirped Ramsey measurement with the strongly coupled NV-center for a higher external magnetic field strength. Figure 26 shows the corresponding sum and difference spectra. The chirp and detection bandwidths were 500 MHz and the maximal value of $t_1 = 3$ μs. The start frequency of the chirp was $\omega_{start} = 2650$ MHz, the pulse duration τ_p = 60 ns and the number of accumulations $12 \cdot 10^6$. The absolute strength of the external magnetic field was ≈ 129 **G** which was measured with a 3-axis Hall sensor. The projected field strength was taken from the splitting of the single-quantum transitions indicated by the *blue* arrow in fig. 26 which was ≈ 51.4 G. Thus the field tilt, with respect to the symmetry axis of the NV-center, was $\approx 66.5°$.

The interpretation of the result of the high-field measurement is not as straightforward as in the case of the low-field. A numerical analysis of the eigenvalue problem, using the Hamiltonian given by Eq. (5), suggests that 8 bundles of multiple single-quantum transitions should be obtainable in the spectrum above 2.6 GHz. Neglecting the lines encircled in *magenta* the chirped spectrum shows only 5 clearly visible multi-line bundles (see fig. 26.b). The *green* circles mark the expected location of the remaining multi-line bundles. The *black* arrows indicate the hyperfine splitting due to the nearest-neighbor ^{13}C (≈ 126.5 MHz). The *red* arrows indicate a splitting (≈ 19 MHz) due to a lifting of the degeneracy of the electron spin ground state $|m_S = 0\rangle$ with respect to the ^{13}C nuclear spin states which has already been mentioned in section 4.2.5 (see also fig. 25.d). Compared to the low-field spectrum, shown in fig. 25.a-c, the signal intensities of the single- and double-quantum coherences have been decreased while the intensities of the zero-quantum transitions (≈ 126.5 MHz and ≈ 19 MHz) have been increased. This could be explained by a growing differ-

ence between the nuclear spin states for the electron spin ground ($|m_S = 0\rangle$) and excited states ($|m_S = \pm 1\rangle$), for rising magnetic field strengths. This corresponds to an increased mixing of the nuclear spin states at the $|m_S = 0\rangle$ state with respect to the $|m_S = \pm 1\rangle$ states. As was explained in the prior section, this state mixing causes the creation of zero- and double-quantum coherences during the excitation with a chirped microwave pulse. Due to the increased state mixing, it is reasonable that contributions of the zero- and double-quantum coherences to the spectrum increase as well.

Most of the lines in the sum- and difference spectra in fig. 26.a can be explained, if we consider the 'missing' line bundles. The origin of the lines marked by solid *magenta* ellipsoids in the difference spectrum (at 129 MHz) and sum-spectrum (at 100 MHz) remains unclear. The frequencies of the multi-line bundle marked by the *green* dashed ellipsoid are equal to the frequencies of the double-quantum coherences (marked by the *blue* dashed ellipsoid) and the hyperfine coupling constant of the nearest-neighbor ^{13}C (here $\approx$ 125.4 MHz). We observed an additional splitting of the zero-quantum coherences shown by the insets in fig. 26.a. The origin of these splittings, which are 0.64 MHz for the peaks at 19 MHz (*red* dashed ellipsoid) and 1.6 MHz for the peaks at 126 MHz (*black* dashed ellipsoid), will be explained in the subsequent section.

Figure 26.c and 26.d show for a comparison the simulated spectrum of the Hamiltonian given by Eq. (19). We yield this spectrum by diagonalizing the Hamiltonian and calculating the transition frequencies between all energy eigenvalues. From the set of eigenvectors we gained the transition probabilities which give the amplitudes of the peaks shown in the spectra. Figure 26.c shows the lower end of the spectrum from 0 MHz to 500 MHz. Figure 26.d shows the upper end of the spectrum from 2650 MHz to 3150 MHz which is equal to the chirp of the pulse. For the sake of simplicity the starting point of the spectrum (2650 MHz) was shifted to the zero point. The low frequency end of the simulated spectrum (fig. 26.c) shows almost the same features as the measured spectrum (fig. 26.a). Thus the simulated spectrum contains zero-quantum coherences (*black* dashed ellipsoids) at 19 MHz and at 126 MHz, with both showing splittings, and also the coherences marked by the *blue* dashed ellipsoid, which are double-quantum coherences, and the *green* dashed ellipsoid. The frequencies of the lines enclosed by the *magenta* dashed ellipsoid are equal to the difference frequencies of the double-quantum coherences and the hyperfine coupling constant of the strongly coupled ^{13}C, while the *green* dashed ellipsoid is given by the sum of the frequencies. It is not clear why the sum-frequencies are experimentally observable while the difference-frequencies are not. For a frequency of $>$ 2650 MHz the simulated spectrum (fig. 26.d) corresponds almost entirely to the experimental one (fig. 26.b). Thus we obtain 8 multi-

line bundles in both spectra, if we include the weak bundles in the experimental difference-spectrum which are marked by *green* solid ellipsoids. The additional feature in fig. 26.b, which is marked by the solid *magenta* ellipsoid, does not appear in the simulated spectrum.

4.2.7 *Simulation of 'High-Field' Spectrum*

To clarify the high-field spectrum presented in fig. 26 of the prior section, we performed a simulation using the Hamiltonian:

$$\begin{aligned} H_{tot} &= H_e + \left(H_{^{14}N} + H_{HF_{^{14}N}}\right) + \\ &\quad \left(H^{(1)}_{^{13}C} + H^{(1)}_{HF_{^{13}C}}\right) + \left(H^{(2)}_{^{13}C} + H^{(2)}_{HF_{^{13}C}}\right) . \end{aligned} \tag{19}$$

The Hamiltonians H_e, $H_{^{14}N}$ and $H_{HF_{^{14}N}}$ are described by Eq. (6), (7) and (3). The last four terms are the Hamiltonians of the two ^{13}C's which are in the proximity of the NV-center. The first two Hamiltonians in the second line of Eq. (19) are assigned to the strongly coupled and the last two to the weakly coupled ^{13}C. The nuclear Zeeman terms $H^{(1)}_{^{13}C}$ and $H^{(2)}_{^{13}C}$ are given by Eq. (8). Since the measured spectra are of low quality, the hyperfine parameters were manually selected to optimize the consistency of simulation and measurement. The hyperfine coupling of the strongly coupled ^{13}C is assumed to be:

$$\begin{aligned} H^{(1)}_{HF_{^{13}C}} &= A^{(1)}_{||_{^{13}C}} S_z I_{z,^{13}C} + A^{(1)}_{\perp_{^{13}C}} \left(S_x I_{x,^{13}C} + S_y I_{y,^{13}C}\right) + \\ &\quad A^{(1)}_{\mathrm{ps}_{^{13}C}} \left(S_z I_{x,^{13}C} + S_z I_{y,^{13}C} + S_x I_{z,^{13}C} + S_y I_{z,^{13}C}\right) , \end{aligned}$$

with $A^{(1)}_{||_{^{13}C}} = 123.5$ MHz, $A^{(1)}_{\perp_{^{13}C}} = 127$ MHz and $A^{(1)}_{\mathrm{ps}_{^{13}C}} = -4$ MHz. For the weakly coupled ^{13}C we assumed a hyperfine interaction of:

$$H^{(2)}_{HF_{^{13}C}} = A^{(2)}_{||_{^{13}C}} S_z I_{z,^{13}C} + A^{(2)}_{\perp_{^{13}C}} \left(S_x I_{x,^{13}C} + S_y I_{y,^{13}C}\right) ,$$

with $A^{(2)}_{||_{^{13}C}} = A^{(2)}_{\perp_{^{13}C}} = 6.85$ MHz. Because the simulations did not give reasonable spectra at the measured value of the absolute field strength, we used the NV-center as a 2-D *magnetic field sensor* and determined the magnetic field strength and orientation from the spectra. We performed simulations for various absolute field strengths and orientations with the aim to fit the frequencies for the first and fifth multi-line bundle to the experimentally obtained values of 2.68 GHz and 2.968 GHz (marked by vertical dashed *gray* lines in fig. 26.b). We used the first and fifth multi-line bundle to determine the field parameters because they belong to the electron spin transitions $|0\rangle \leftrightarrow |+1\rangle$ and $|0\rangle \leftrightarrow |-1\rangle$ which were split by the Zeeman interaction. Thus they are proportional to the strength and orientation of the external magnetic field. The simulations yielded an absolute field strength of

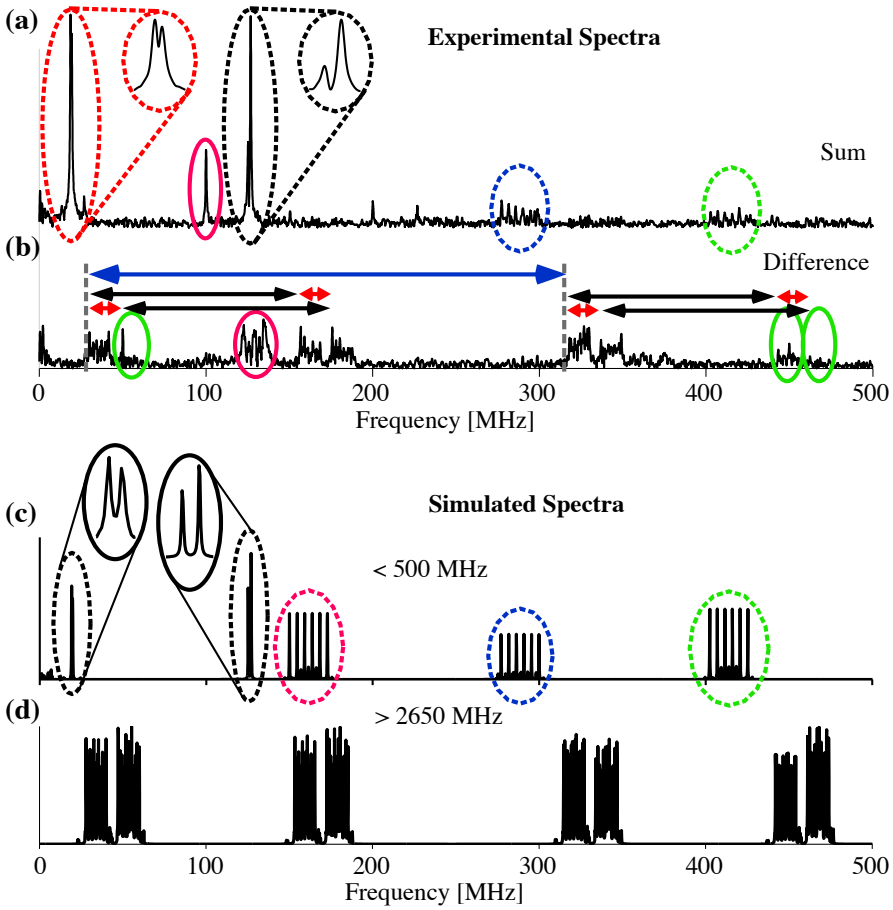

Figure 26: Chirped Ramsey Measurement at higher external field strength. The sum-spectrum (a) shows the zero- and double-quantum coherences and the difference-spectrum (b) shows the single-quantum coherences. The colors of the arrows, which point out the separations of the line bundles in the difference-spectrum, correspond to the colors of the dashed ellipsoids shown in a). The frequencies of the multi-line bundle marked by the *green* dashed ellipsoid are equal to the double-quantum frequencies plus the hyperfine splitting of the strongly coupled ^{13}C, which here is $\approx$ 125.4 MHz. The insets show magnifications of the zero-quantum coherences which are split into two lines with the frequencies: 126.8 MHz, 125.2 MHz (*black* dashed ellipsoid) and 19.41 MHz, 18.77 MHz (*red* dashed ellipsoid). For comparison, a simulated spectrum is shown in (c) and (d). An detailed explanation is given in the text. The intensities of the lines are normalized to the strongest line observed in the corresponding frequency range. On an absolute scale the intensity of the strongest line in c) is $\approx 1/4$ of the intensities of the lines in d). The *blue* dashed ellipsoid in c) marks the double-quantum coherences. The *red* dashed ellipsoid corresponds to the difference-frequency and the *green* dashed ellipsoid to the sum-frequency of double-quantum coherences and the hyperfine coupling constant of the strongly coupled ^{13}C.

95 G and an angle between the field and the NV symmetry axis of $\approx \pm 57.25°$.

The simulations showed that the frequency of the peak, which is in fig. 26.c at 19 MHz, depends on the size of the non-secular hyperfine component $A^{(1)}_{\perp_{13C}}$ of the strongly coupled ^{13}C. The splitting of the peak at 126 MHz seems to depend on the pseudo-secular hyperfine component $A^{(1)}_{ps_{13C}}$ of the strongly coupled ^{13}C. If $A^{(1)}_{\perp_{13C}}$ becomes bigger than $A^{(1)}_{||_{13C}}$, the frequency of the peak at 126 MHz shifts to higher frequencies but also the transition probabilities of the peaks at 19 MHz and 126 MHz raise compared to the double-quantum coherences (marked by the *magenta*, *blue* and *green* dashed ellipsoid). For increasing values of $A^{(1)}_{ps_{13C}}$ the splitting of the line at 126 MHz grows. The splitting of the peak at 19 MHz seems to be caused by the non-secular component $A^{(2)}_{\perp_{13C}}$ of the weakly coupled ^{13}C. Thus the splitting grows, if $A^{(2)}_{\perp_{13C}}$ is increased. Since the quality of the measured spectrum is poor, more measurements with better signal-to-noise ratio and with different orientations of the magnetic field as well as different field strengths should be performed to clarify the spectra and the parameters of the Hamiltonians.

4.3 CONCLUSIONS

We have introduced a new experimental technique for measuring broad spectra of electron spins. This approach does not require high microwave power. The precession frequency of the spins is measured in the absence of microwave irradiation, in the form of Ramsey fringes, which results in high resolution spectra. The resulting spectra contain not only the dipole-allowed single-quantum transitions, but also multiple quantum transitions that can only be excited by multiple absorption/emission processes. We have shown broadband spectra of single NV-centers without and with adjacent ^{13}C. We investigated the behavior of the spectra under variation of external magnetic field and phase differences between excitation of readout pulses. We verified that a discrimination of single- and zero- respectively double-quantum coherences is possible by subtracting respectively adding two phase-sensitive spectra where the phases of the readout pulse differed by 180°. This technique is particularly useful in the case of electron spins coupled to multiple nuclear spins. Such clusters of spins may be important for quantum computing applications [11, 12, 79, 13]. The chirped Ramsey sequence can be a useful tool in seeking for precise data concerning the shape of the hyperfine coupling between ^{13}C and NV-centers. Thus we have shown a simulated spectrum, which fits quite well to the measured spectrum, by adding a pseudo-secular contribution to the hyperfine interaction tensor which was not taken into account by the NV-center community before. Further analysis

of a series of chirped Ramsey measurements with different orientations of the external magnetic field as well as different field strengths should clarify the origin of some unexplained peaks in the measured spectrum as discussed above (cf. fig. 26).

Here, we have demonstrated the chirped Ramsey technique on the example of single electron spins in the diamond NV-center, but the same approach should also be applicable to other systems where the excitation bandwidth can be sufficiently large.

5 DYNAMICAL DECOUPLING

In this chapter we present the results of the application of dynamical decoupling (DD) sequences which we applied to diamond NV-centers. In section 5.1 the effect of DD sequences is shown, which are applied to a single transition of the NV-center electron spin. In this case the NV-electron spin can be handled as a pseudo-spin 1/2. The performance of different DD sequences (CPMG, XY-4 and KDD) was studied with respect to pulse imperfections and arbitrary phases of the initial states which was published in [23]. In section 5.2 we present the results of the application of the CPMG sequence to a double-quantum coherence, where both transitions of the NV election spin have been excited by composite microwave pulses.

5.1 ROBUST DYNAMICAL DECOUPLING OF SINGLE QUANTUM COHERENCE

For quantum computing it is important to have sufficiently long transverse coherence times T_2 to implement quantum algorithms. It is well known that by application of DD sequences T_2 of a spin system can be extended. But the usefulness of these sequences for practical applications depends on the robustness of the performance with respect to experimental imperfections, such as finite precision of control field amplitudes. Since the number of control operations required for effective DD can be very large, it is essential that the errors from the individual control operations do not accumulate. This goal can be achieved by fault-tolerant DD sequences. In such sequences the errors due to individual pulses respectively control operation imperfections are compensated by the other control operations over the whole cycle of the sequence [72, 86, 71].

Here, we test this approach on a single NV-center in diamond. The effectiveness of the DD technique has been tested with different types of diamond; de Lange, et al.[53] used a diamond with a relatively high concentration of nitrogen impurities, which generates a strong electron-spin bath. Other studies employed CVD grown diamond crystals with reduced nitrogen concentrations, in which the nuclear spin bath of the ^{13}C nuclear spins is the major source of decoherence [72, 87, 49].

This work differs from earlier studies by extending the dephasing time T_2 to nearly the value of the spin-relaxation time T_1 by applying hundreds of refocusing pulses. With such a large number of pulses, the unavoidable imperfections of the individual gate op-

erations would usually destroy the coherence of the qubits, thus we used robust DD sequences to overcome this issue. Additionally we investigated the robustness of DD sequences by applying pulses with artificially inserted imperfections as flip angle errors and frequency offsets.

In actual quantum computer schemes, quantum data, which for example is stored in a spin state vector in the xy-plane, will have an arbitrary orientation with respect to the irradiation direction of the inversion pulses of the DD sequence. Thus, because a robust DD sequence should show a high performance for any quantum state, it is necessary to perform appropriate verifications about the sequence's overall robustness. We therefore present here a study in which we compare the performance of different DD sequences for arbitrary initial quantum states.

5.1.1 *Experimental Results*

The pulses for the DD sequences in this section were generated with an AWG with a sampling rate of 2 GS/s. The generated pulses had a frequency of 250 MHz, which was up-converted with a carrier frequency to match the resonance frequency of the NV electron spin. A permanent magnet was used to apply a static magnetic field, which was roughly aligned with the direction of the principal axis of the NV-center. The investigations were performed with NV-centers of the natural abundance diamond sample (see sec.2.2). All the measured curves in the present work are normalized in order to indicate the probability $P_0 = P(|0\rangle)$ of the bright state $|m_S = 0\rangle$. As a reference for the normalization, maximum and minimum values from the Rabi oscillation curve were taken for $P_0 = 1$ and $P_0 = 0$ respectively. To determine the efficiency of the DD sequences, we measured the survival probability which is given by:

$$\rho_0 = |\langle \psi_F | \psi_I \rangle|^2 \,. \tag{20}$$

$|\psi_I\rangle$ represents the initial state before the application of the DD sequence and $|\psi_F\rangle$ the state at the end of the sequence. As described in section 2.8 the final state is transferred back to population by an additional MW readout pulse. Here, the readout pulse is equal to the first MW pulse, which creates the initial state, except for the inverted rotation direction.

5.1.1.1 *Spin system*

In the natural abundance diamond crystal with reduced nitrogen concentration, the ^{13}C nuclear spins form a spin bath that induces decoherence on the NV-center [55, 79]. In the case of Hahn echoes, the decoherence due to the ^{13}C nuclear spins can be reduced signif-

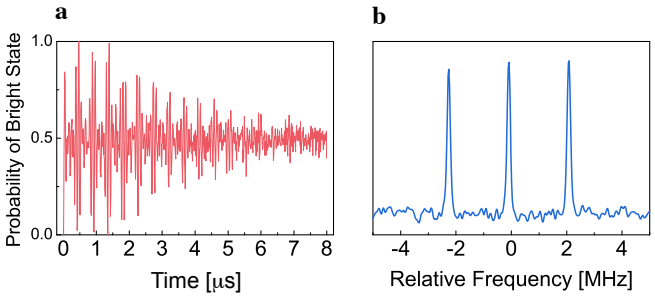

Figure 27: (a) Ramsey fringe; (b) Fourier transformation of Ramsey fringe curve shows only three peaks due to hyperfine interaction with ^{14}N nuclear spin of the NV-center.

icantly when the free precession period between the excitation and refocusing pulse is a multiple of the nuclear spin Larmor precession period [57]. For the present study, we selected an NV-center that had no ^{13}C nuclear spins in its immediate vicinity, so the coupling to the nuclear spin bath is relatively weak and the time scales for decoherence are correspondingly larger. Figure 27.a shows the Ramsey fringe signal measured from this center and fig. 27.b its spectrum yielded by Fourier transformation. We applied a magnetic field of 6.8 mT along the direction of the symmetry axis and excited the transition at 2.68 GHz with resonant microwave pulses. The Rabi frequency used in our measurements was 12.5 MHz. The number of accumulations for the presented data was $2 \cdot 10^6$.

5.1.1.2 *Dynamical decoupling*

One of the simplest pulse sequences for dynamical decoupling is the CPMG sequence - a train of equidistant π-pulses around the same axis. The performance of a DD sequence can be verified by keeping the number of pulses fixed and successively increasing the delay time between the pulses. For rising delay times the received signal usually decays and yields a time constant which depends on the applied DD sequence. In fig. 28, we compare the signal decays for different CPMG sequences, starting with the Hahn echo at the bottom and experiments with increasing numbers of refocusing pulses towards the top. In each curve, we observe an initial fast decay, which is followed by a series of revivals. The revivals are separated by $2N\tau_L$, where N is the number of π pulses in the sequence and $\tau_L \approx 73$ μs is the Larmor period of the ^{13}C nuclear spins. This implies that the refocusing is most effective when the nuclear spins constituting the environment have completed an integral number of Larmor precessions between the pulses. The dashed curves in fig. 28 represent fits with the function:

$$f(t) = \exp(-(\frac{t}{T_2})^n) \; . \tag{21}$$

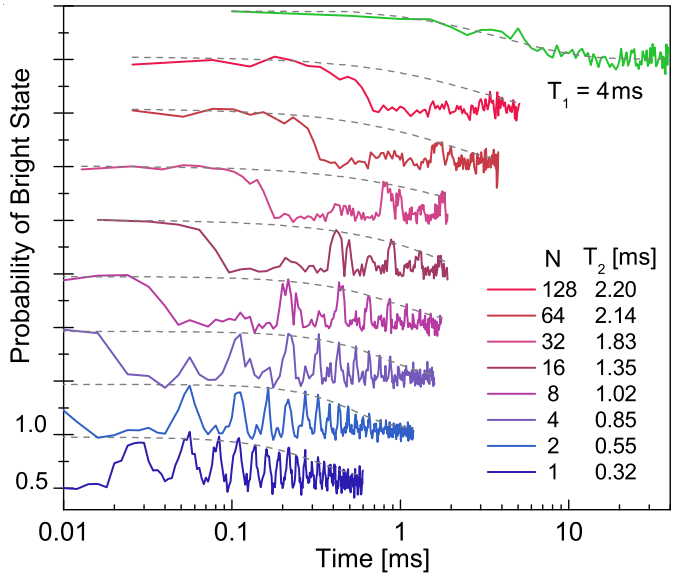

Figure 28: Coherence decay curves for different dynamical decoupling sequences. The bottom curve shows the result from the Hahn echo, the upper curves correspond to the CPMG sequences with increasing number of refocusing pulses. The gray dashed lines represent fits to the function given by Eq. (21). The initial state was chosen along the rotation axis of the refocusing pulses. The top curve shows the longitudinal relaxation of the bright state with $T_1 \approx 4$ ms.

The decay times T_2 and exponents n are fitted to the maxima of the Larmor revivals in the experimental data. The coherence times T_2 are given in the figure legend.

Figure 29 summarizes the increase of the coherence time with the number of refocusing pulses. The coherence times resulting from the CPMG measurements are shown as black squares. The filled squares represent the values obtained by fitting the decay of the Larmor revivals (see dashed curves in fig. 28) which yields T_2. The open squares represent the initial decay time constants which are denoted as T_2^0. In both cases, the decay time increases with the number of pulses in the DD sequence. If we take the values from the maxima of the Larmor revivals, they increase from ≈ 0.3 ms (for the Hahn echo) up to ≈ 2.2 ms (for CPMG with $N = 128$).

Apart from the increase of the coherence time with the number of pulses, we find that also the shape of the decay curve given by Eq. (21) changes. In fig.29, we quantify this by the exponent n, which changes from ≈ 3 (for the Hahn echo) to ≈ 1 (for CPMG with $N = 128$). This result indicates that different processes are responsible for the observed decoherence. For relatively long pulse separations, as in the case of the Hahn echo, the dominant environmental interaction is the hyperfine coupling to the nuclear spins. The shortest relevant timescale for the nuclear spins is the Larmor precession of the ^{13}C's,

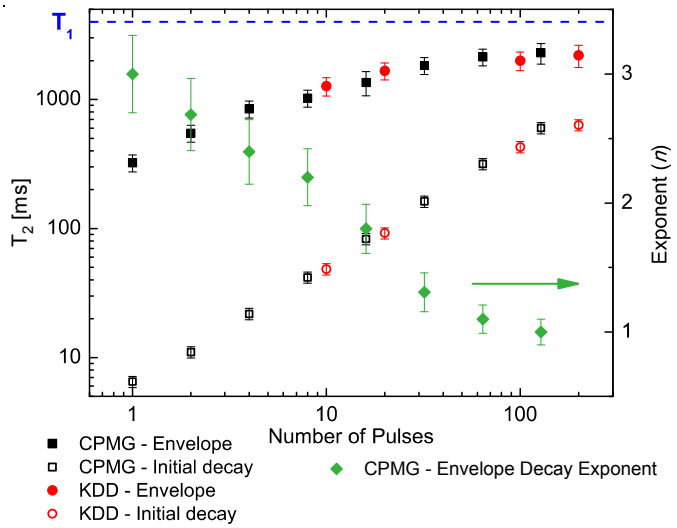

Figure 29: T_2 and T_2^0 as a function of the number of pulses in the CPMG and KDD sequences. Black symbols show CPMG and red KDD data. Solid symbols represent T_2 values obtained from the envelope of the revivals, and open symbols are T_2^0 values from the initial decay. Green symbols represent the exponent n in the decay function of Eq. (21). The initial state was pointing along the irradiation axis of the CPMG pulses in the rotating frame. The dashed blue line shows the value of T_1.

which has a period of $\tau_L \approx 73\ \mu$s. Since this evolution is coherent, the associated decay is refocused at specific times, giving rise to the Larmor revivals [88]. On a slower timescale, the nuclear spins undergo mutual spin flips, which also contribute to the decoherence of the electron spin.

When the spacing between the pulses is short compared to the Larmor period, the decoupling of the NV electron spin from the ^{13}C nuclear spin bath is almost perfect. This is demonstrated in fig. 29 by the convergence of the curves from the decay time of the envelope with that of the initial decay. Both time scales converge to a limiting value of ≈ 2.2 ms, which is only slightly shorter than the longitudinal relaxation time $T_1 \approx 4$ ms for this spin. Apparently, the remaining decoherence arises from processes with significantly shorter correlation times, which cannot be refocused by dynamical decoupling. Possible candidates for these processes could be interactions with electric fields [17] or phononic processes. This interpretation is compatible with the observation of a purely exponential decay, which is expected if the correlation time of the environment is shorter than the interpulse delay of the dynamical decoupling.

5.1.1.3 *Parallel and orthogonal initial states*

The above experiments were performed with one specific initial condition, for which the CPMG sequence is optimized. However, in quan-

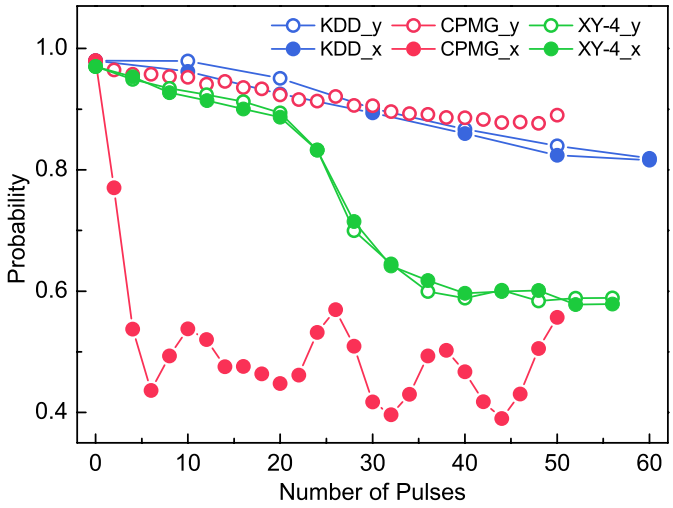

Figure 30: Survival probabilities of two orthogonal initial states, $|x\rangle$ (solid symbols) and $|y\rangle$ (empty) during different sequences of equidistant refocusing pulses for CPMG (red), KDD (blue), and XY-4 (green). The time interval between the refocusing pulses was fixed to 0.8 μs.

tum information processing, DD sequences will probably be applied in parallel to the control operations of a quantum algorithm and thus the conditions of the state which is to be decoupled from the environment are not known. To evaluate the effectiveness for arbitrary initial conditions, we now consider the effect of the DD sequence on two orthogonal initial conditions $|x\rangle = (|0\rangle + |1\rangle)/\sqrt{2}$ and $|y\rangle = (|0\rangle + i|1\rangle)/\sqrt{2}$. Figure 30 shows the decay of these states for the DD sequences CPMG, KDD, and XY-4 as a function of the number of refocusing pulses. In the case of the CPMG sequence, we observe a strong asymmetry between the two initial condition: If the initial spin polarization is oriented along the rotation axis of the refocusing pulses, the state preservation is very effective. If the initial state is perpendicular to the direction of the pulses, the first ≈ 10 pulses destroy the coherence almost completely. This effect is expected if the rotation angle of the pulses deviates from the ideal value of π. Such a flip angle error compensates over one cycle of the CPMG sequence if the state is polarized along the rotation axis, but for orthogonal orientations, the flip angle errors of the individual pulses accumulate and cause an unwanted evolution of the system [69, 89, 64].

Such a strong dependence on the initial state of the system is not practical for the application in quantum information processing. Universal DD sequences must be effective for arbitrary quantum states and they have to be robust against pulse errors. The earliest sequence that was designed to meet this requirements is the XY-4 sequence [89, 70, 90] and its derivatives that increase the robustness by combining different versions of the basic XY-4 cycle into longer cycles with better compensation of pulse imperfections [70, 91]. A more recent

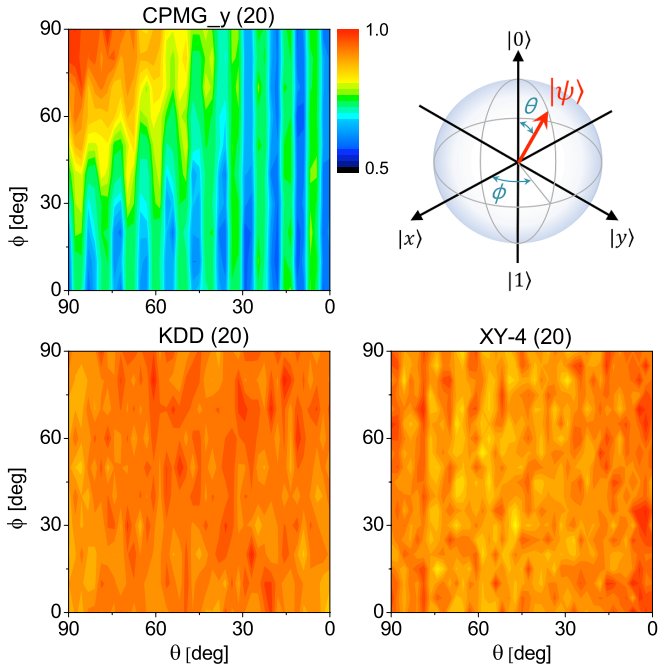

Figure 31: Experimental results of the survival probability $|\langle\psi_F|\psi_I\rangle|^2$ for the sequences CPMG, KDD and XY-4 after 20 DD pulses as a function of the parameters θ and ϕ that define the initial state of Eq. (22). The top left corner illustrates the Bloch sphere representation of arbitrary state of the NV-center. The time interval between the refocusing pulses was fixed to 1 μs.

sequence that shows even better performance is the KDD sequence [71], which is based on an expansion scheme developed by *Cho* et al. [92]. As shown in fig. 30, the performance of KDD and XY-4 does not depend on the initial state, within the experimental uncertainties. The performance of the XY-4 sequence is comparable to that of CPMG_y for < 20 pulses but deteriorates for longer sequences, while the KDD sequence matches the performance of CPMG_y for both initial conditions, indicating that this sequence largely compensates the flip angle errors of the individual pulses.

5.1.1.4 *Arbitrary initial states*

To perform measurements with arbitrary initial conditions, we prepared initial states which are expressed by

$$|\psi_I\rangle = \cos(\frac{\theta}{2})|0\rangle + \sin(\frac{\theta}{2})e^{i\phi}|1\rangle, \tag{22}$$

where the angles θ and ϕ, which parametrize the state, correspond to spherical coordinates on the Bloch sphere. Figure 31 shows the observed survival probability of the final state after 20 refocusing pulses. The three panels represent the survival probability as a function of θ and ϕ for the three DD sequences CPMG, XY-4 and KDD.

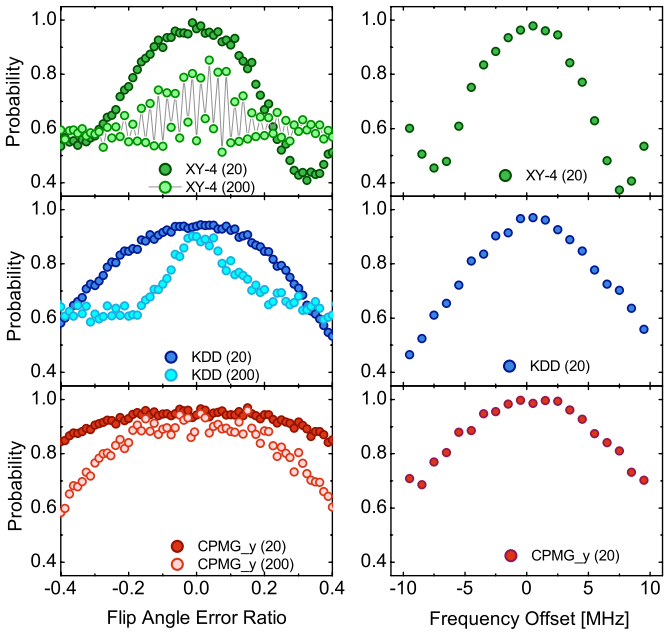

Figure 32: Left column: Survival probability of the electron spin state as a function of the fractional flip angle error with respect to a 180° flip angle. The initial state was chosen along the rotation axis of the CPMG pulses. The numbers in the parentheses represent the number of refocusing pulses in the DD sequence. Right column: Variation of survival probability as a function of the frequency offset errors of the pulses. The numbers in the parentheses represent the number of refocusing pulses in the DD sequence. The time interval between the refocusing pulses was fixed to 1 μs.

All three sequences reach almost perfect survival probabilities for $\theta = \phi = 90°$, which corresponds to the y initial condition where the spins are aligned with the rotation axis of the CPMG pulses. In the case of CPMG, the performance deteriorates when the initial condition deviates significantly from this situation. This behavior is an indication that the decay of the system fidelity is dominated not by the environment, but rather by pulse imperfections [64, 71].

5.1.1.5 *Effect of pulse imperfections*

Apart from finite pulse durations, the two dominant experimental imperfections that limit the performance of experimental dynamical decoupling are flip angle errors and frequency offset errors. In fig. 32, we experimentally investigate the effect of these imperfections on the performance of different dynamical decoupling sequences. In the left hand columns, we measured the remaining spin polarization after 20 and 200 pulses as a function of the actual flip angle of each pulse. For 20 refocusing pulses and longitudinal initial conditions, flip angle errors of up to ± 10 % do not reduce the fidelity. For the robust sequences, whose performance does not depend significantly on the

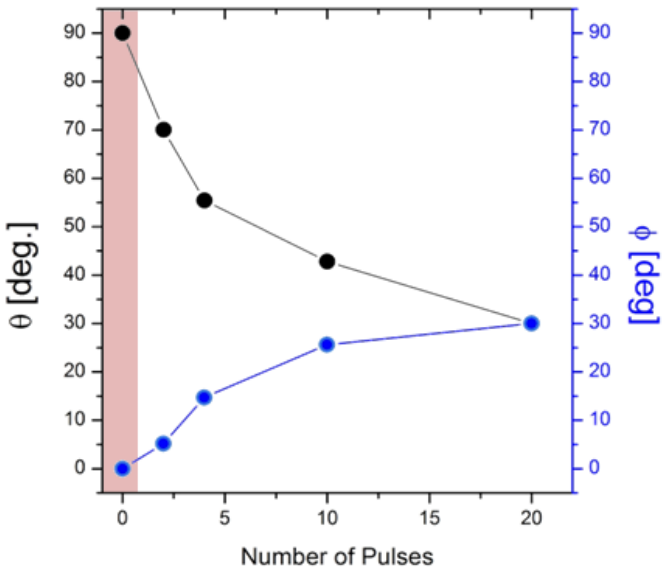

Figure 33: Tomography of the final spin state with respect to the initial state after the application of the CPMG sequence. The x-axis gives the number of refocusing pulses of the sequence. The angles θ and ϕ parametrize the state vector given by Eq. (22). The initial state was oriented along the x-axis with $\theta = 90°$ and $\phi = 0$. In this case CPMG acts like the CP sequence which very is sensitive to pulse imperfections. The decay of the spin coherence during the application of the DD sequence was negligible.

initial condition, KDD clearly outperforms XY-4. This is particularly well visible for 200 pulses. Interestingly, XY-4 shows strong oscillations as a function of the flip angle error. This implies that XY-4 becomes very sensitive to flip angle errors if more than 100 refocusing pulses are used, which limits its usability. The right hand column shows the measured behavior as a function of the offset error for 20 refocusing pulses. For all three sequences, we observe significant reductions of the fidelity if the offset exceeds $\approx$ 2 MHz. This is significantly less than the Rabi frequency (12.5 MHz) of the pulses used for these experiments and comparable to inherent offsets like the hyperfine interaction with the ^{14}N nuclear spin.

In order to better understand the processes that reduce the process fidelity, we performed state tomography after the application of the CPMG sequence with 20 inversion pulses to an initial state which was orientated along the x-axis ($\theta = 90°$, $\phi = 0$). Figure 33 shows an increasing deviation of the state orientation of the final state from the initial state with increasing number of refocusing pulses. After the 20 refocusing pulses the angles θ and ϕ reached both a value of $\approx 30°$. From the change of θ we estimate from the state tomography a pulse flip angle error of $\approx 9°$, which corresponds to a 5 % deviation from the targeted 180° rotation. This value is close to the achievable resolution of the pulse duration in our setup, which is limited to 0.5 ns

due to the sampling rate of 2 GS/s of our AWG. From the change of ϕ we estimate additionally a frequency offset of $\approx$ 1.9 MHz. This level of error is supported by the results of the frequency offset errors in fig. 32 (diagrams on the right side). The central positions of all three curves are slightly shifted to positive frequencies by 0.5 MHz to 1.5 MHz. The origin of this frequency offset error is unclear, because we tuned the excitation frequency of the microwave pulses as precisely as possible to the frequency of the central line of the hyperfine split electron spin transitions (see fig. 27.b), thus any off-resonance effect of the two outer hyperfine lines will appear symmetrical around the central line but should not cause a frequency offset. To confirm whether the off-resonance effect is responsible for the frequency offset errors measured in fig. 32, experiments at the excited state level anti-crossing point (514 G) could be performed. Thus only one of the ^{14}N nuclear spin states will be populated [80] and the off-resonance effect will be removed completely.

5.1.2 *Conclusions*

Dynamical decoupling is an effective method for increasing the coherence time of quantum bits, such as spin qubits in solids. As long as the fluctuations of the noise sources are comparable to or slower than the system's coherence time, DD can increase the survival time of the quantum information. The main contribution to the decoherence in natural abundance diamond is due to the ^{13}C nuclear spin bath. We have shown that the decoupling of a single NV electron spin from the spin bath by CPMG and KDD sequences performs well and yields a T_2 of up to 2.2 ms. This is very close to the T_1 limit of $\approx$ 4 ms, which is determined by different, more rapidly fluctuating processes. We found that the recently introduced DD sequence KDD is remarkably robust and performs well for arbitrary initial conditions. It is much less susceptible to experimental uncertainties, such as flip-angle errors and frequency offsets, than the simpler sequences CPMG and XY-4. We expect that the KDD sequence will be used for many other purposes requiring long coherence time, such as ac-magnetometry or to increase the lifetime of multipartite systems, including entangled states.

5.2 DYNAMICAL DECOUPLING OF DOUBLE-QUANTUM COHERENCE

In the case of a diamond NV-center noise acting on a *double-quantum coherence* (DQC) behaves essentially in the same way as on a *single-quantum coherence* (SQC) but the sources and the strength of the influence might differ. Because the two electron spin states $|\pm 1\rangle$ are involved in a DQC, its sensitivity to magnetic field fluctuations is

doubled compared to a SQC. On the other hand, a DQC is less sensitive to temperature fluctuations since the splitting of the states $|\pm 1\rangle$ is only given by an external magnetic field. For a SQC however the level splitting is given by a magnetic field and the zero-field splitting which shows a temperature dependency [19, 20, 21]. This temperature dependency opens a possibility for a practical application of the NV-centers as atomic scaled temperature sensors. In this case, DQCs might play a roll to determine the contribution of the external magnetic field to the Larmor frequency of a SQC.

5.2.1 *Experimental Results*

For the measurements presented in this section we used the same setup as described in the the prior section 5.1 and also the natural abundance diamond. The external magnetic field was not aligned to the symmetry axis of the NV-center and had a projected field strength of $\approx$ 34 G. All measured curves are normalized in order to indicate the probability $P_0 = P(|0\rangle)$ of the bright state $|m_S = 0\rangle$. For the normalization we used again the maximum ($P_0 = 1$) and minimum ($P_0 = 0$) values from the Rabi oscillation curve.

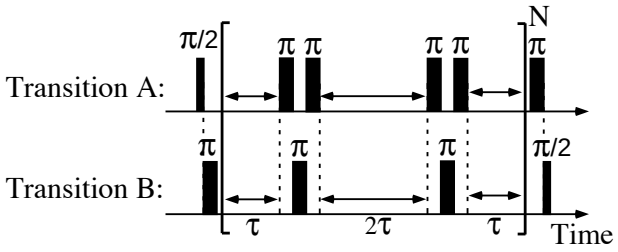

Figure 34: CPMG sequence for double-quantum coherences: Transitions A and B denote the two electron spin transitions (cf. fig. 8.a). The first and last pulses are composite $\pi/2$-pulses and two pulses inside the brackets are composite π-pulses as given in fig. 8.b. N represents the number of cycles of the enclosed sub-sequence. For both transitions the durations of the $\pi/2$-pulses were $\approx$ 25 ns and of the π-pulses $\approx$ 50 ns.

To gain some insights about the noise sources, which act on SQCs as well on DQC, we applied the CPMG sequence to a DQC of a single NV-center. Figure 34 shows a scheme of the applied CPMG sequence. The DQC was created by a composite pulse consisting of a $\pi/2$-pulse and the transition A and a π-pulse on transition B to create the DQC. For definitions of the transition designation see fig. 8.b in section 2.6.2. The inversion pulses of the CPMG sequence that is applied to the DQC is composite of three SQC-pulses: a π-pulse on transition A, a π-pulse on transition B and a second π-pulse on transition A. The Rabi frequencies of both transitions were $\approx$ 10 MHz. Thus all three

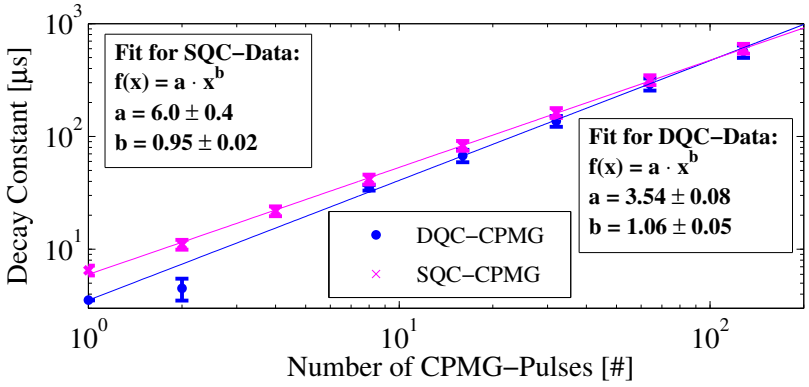

Figure 35: Comparison of T_2 of SQCs (blue circles) and DQCs (magenta squares) under application of dynamical decoupling (CPMG). The number of refocusing pulses was increased in multiples of 2^N where N is given by the number of CPMG cycles.

hyperfine split electron spin transitions were excited by the applied pulses.

Figure 35 shows the resulting coherence times of the DQCs using the CPMG sequence and a comparison with the SQC coherence times of the initial decays. The results are plotted on a double logarithmic scale. Exponential functions $f(x) = a \cdot x^b$ are fitted to the data sets. The fits were weighted with respect to the uncertainties of the data points. As can be seen the coherence times of the DQCs are smaller for lower number of pulses. The number of pulses is increased in multiples of 2^N, with N denoting the number of cycles. In case of single-quantum coherences the increment with the number of pulses is approximately $N^{0.95}$, for double-quantum coherences it is approximately $N^{1.06}$. Overall both coherences converge to the same time, limited by $T_1 \approx 4$ ms of the bright state for the sample used in this measurements (cf. fig.9.c).

5.2.2 *Discussion*

Figure 36.a shows the DQC Hahn echo decay and fig. 36.b the DQC CPMG echo decay with 4 cycles (more data are shown in section A.3). It is interesting to note that the amplitudes of the DQC CPMG echos did not reach as large values as the DQC Hahn echo or the SQC CPMG echos. It seems that the refocusing of the DQC CPMG echo of the shown measurement data is less effective for short evolution times but reaches a maximum at around 15 μs.

The decay constants of the DQC measurements, which are shown in fig. 35, are yielded by fitting the function:

$$f(t) = a \cdot \exp\left(-t/dt\right)^4 + b \,,$$

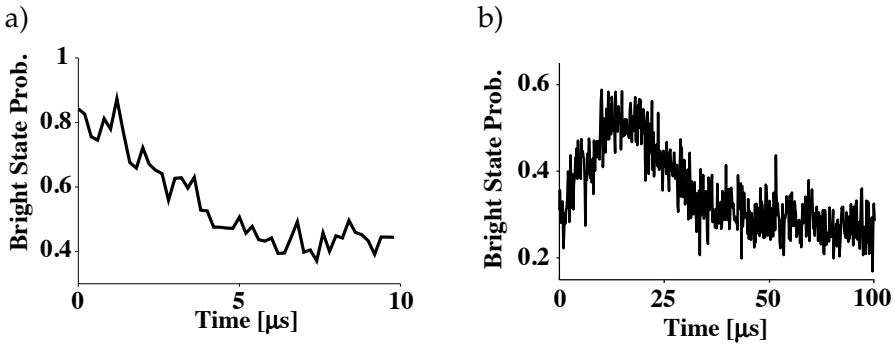

Figure 36: a) DQC Hahn Echo measurement and b) DQC CPMG measurement with 4 cycles.

to the data sets [93]. a is the amplitude, b the offset and dt the decay constant. The fractions of the decay data sets, which contain the rising of the DQC CPMG echos, were ignored during the fitting procedure. The measurements of the offsets b ranged between 0.26 and 0.33 and the values for the amplitudes a ranged between 0.16 and 0.24.

Additionally, we performed measurements to verify the refocusing positions of the Hahn and CPMG echos. The results are shown in fig. 37. The refocusing of the Hahn echo works well, while on the other hand the CPMG echo is time shifted and the refocusing takes place $\approx$ 20 μs earlier as expected. We performed numerical simulations (not shown) which indicated that the shift of the echo position is related to the large durations of the composite pulses and that the position shift would vanish for larger Rabi frequencies.

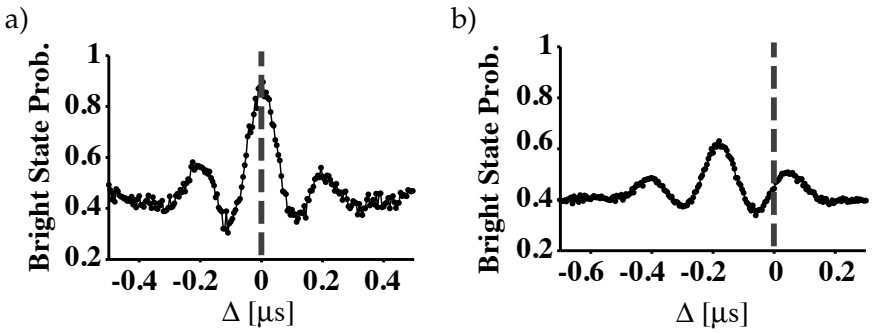

Figure 37: Echo refocusing positions: a) Position of Hahn echo and b) of the CPMG echo for double-quantum coherences. The DQC Hahn echo refocuses as expected at $\Delta = 0$ while the CPMG echo refocuses before the expected echo position and shows a time shift of $\Delta \approx -20$ μs. Numerical simulations indicate that this is related to the long durations of the composite pulses which were approximately 75 ns for a $\pi/2$ and 150 ns for a π-pulse.

5.2.3 *Conclusion*

Our measurements showed that T_2 for the DQC is smaller compared to those of the SQC which indicates that the main source of decoherence is due to magnetic field fluctuations respectively distortions coupling to the $|\pm 1\rangle$ states. *Zhao* et al. [94] performed a theoretical analysis and predicted that the coherence time of the DQC can be longer than for the SQC and called it an *anomalous decoherence effect*. *Huang* et al. [95] performed measurements on single NV-centers in diamond and verified the results of *Zhao* et al.. They performed their measurements at weak magnetic fields (< 20 G) and used selective microwave pulses to excite one of the three hyperfine split electron spin transitions. They used the CP sequence to decouple the NV electron spin and the environment. The measurements we carried out and presented in this section did not reveal an anomalous decoherence effect even if the used sample was also a type-IIa diamond with nitrogen concentrations < 1 ppb. A difference between our excitation scheme and the one of Ref. [95] is that we used non-selective excitation pulses and excited all three hyperfine lines. It is unclear whether this has an influence on the decoherence process and the difference between our result and that of Ref. [95] can be attributed to it.

6 ELECTRON SPIN ECHO ENVELOPE MODULATION

The hyperfine coupling between a ^{13}C nuclear spin and a NV electron spin can have an influence on the Hahn echo decay of the electron spin and can cause modulations in the signal. The modulations are called *electron spin echo envelope modulation* (ESEEM) and can be used to investigate the hyperfine coupling between the spins [96, 97]. We applied the *two-pulse* ESEEM sequence to NV-centers coupled by hyperfine interaction to ^{13}C's in the immediate vicinity. The two-pulse ESEEM sequence is identical to the Hahn echo sequence which was introduced in section 2.8.1. The two pulse ESEEM was already measured with NV bulk samples in Ref. [98], but there, only the nuclear Zeeman interaction of the ^{13}C atoms was observable in the ESEEM spectrum. In bulk measurements the contributions of the ^{13}C hyperfine interactions to the ESEEM cancel, because of the large number of coupled ^{13}C's and the variance of the hyperfine coupling strength, which is related to the distance between the NV-center and the ^{13}C's. Here, we present ESEEM measurements of two single NV-centers in a natural abundance diamond sample, each coupled to a ^{13}C in the close proximity. The ESEEM spectra show relations to the secular hyperfine components which were confirmed by Ramsey measurements. In section 6.1.1 we show the relationship between the spectrum of the Ramsey measurement and the ESEEM spectrum. In section 6.1.2 we show the dependency of the ESEEM modulation frequency and amplitude under application of the CPMG sequence with increasing number of refocusing pulses.

6.1 EXPERIMENTAL RESULTS

All measured curves in this section are normalized in order to indicate the probability $P_0 = P(|0\rangle)$ of the bright state $|m_S = 0\rangle$. For the normalization we used the maximum ($P_0 = 1$) and minimum ($P_0 = 0$) values from Rabi oscillation measurements. For the presented measurements we used an AWG with a sampling rate of 2 GS/s and generated pulses with a frequency of 250 MHz, which was up-converted with a carrier frequency to match the resonance frequency of the corresponding electron spin transitions. A permanent magnet was used to apply a magnetic field to the NV-centers. The field was not aligned with the NV symmetry axis and had a projected field strength of ≈ 61 G for both measurements presented in the following.

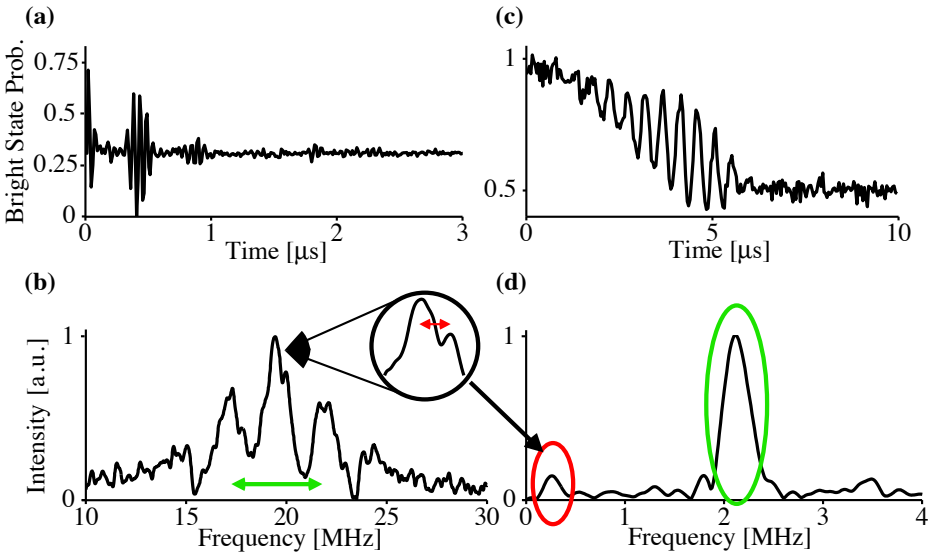

Figure 38: Ramsey fringe and two-pulse ESEEM modulation of the first NV-center: In a) the Ramsey fringes and in b) the corresponding spectrum are shown. c) shows modulations in the Hahn echo decay whose spectrum is given in d). The *green* and *red* arrows in b) indicate a splittings due to couplings to ^{13}C's. The spectrum of the ESEEM in d) shows two peaks, marked by the *green* and *red* ellipsoids, whose frequencies correspond to half of the splittings observed in b). The number of accumulations of the Ramsey measurement was $4.7 \cdot 10^6$ and for the Hahn echo $1.2 \cdot 10^6$. The Rabi frequency was 10.62 MHz and the spectrum is shifted due to a detuning of the reference frequency by 20 MHz.

6.1.1 *ESEEM of NV-center coupled to ^{13}C*

Utilizing the Ramsey fringe spectrum (see fig. 38.b) we identified a single NV-center coupled to two ^{13}C nuclear spins, to which we applied the Hahn echo sequence in the following. Figure 38.a shows the time domain signal of the Ramsey measurement. In fig. 38.b the relevant range of the spectrum of the Ramsey fringes is shown. The *green* arrow indicates a splitting of $\approx$ 4.34 MHz which is caused by an adjacent ^{13}C. The inset in fig. 38.b shows a zoom of the central peak to improve the visibility of an additional splitting of $\approx$ 0.5 MHz, due to a second ^{13}C, which is indicated by the *red* arrow[1]. The Hahn echo in fig. 38.c shows the ESEEM signal caused by the hyperfine couplings of the two carbons. To get the spectrum of the ESEEM, an exponential decay was subtracted from the Hahn echo time domain signal and a Gaussian damping was applied. The spectrum, shown in fig. 38.d., contains peaks at $\approx$ 0.26 MHz (*red* ellipsoid) and $\approx$ 2.1 MHz (*green* ellipsoid) which is approximately half of the splittings shown in the spectrum of fig. 38.b.

1 An overview of the hyperfine coupling values for ^{13}C atoms located at different lattice sites in the proximity of a NV-center is given in Ref. [42, 43].

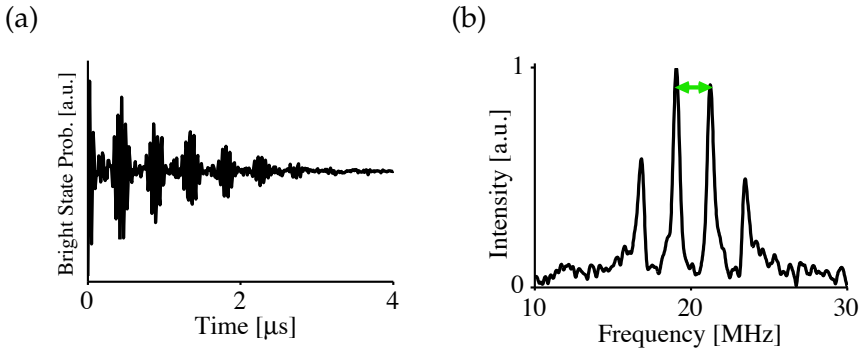

Figure 39: Ramsey fringe of the second NV-center: In a) Ramsey fringes and in b) the spectrum are shown. The spectrum is the result of two superposed triplets that are split by a frequency of $\approx$ 2.18 MHz. The *green* arrow denotes the splitting. We used a Rabi frequency of 10.74 MHz and a detuning of the reference frequency of 20 MHz. The number of accumulations was 10^6 and the increment for the free evolution time t_1 was 12 ns.

6.1.2 *ESEEM in CPMG Signal*

In this section we present the results of the ESEEM measurements using the CPMG sequence which was introduced in section 2.8.2. The time domain signal and the relevant range of the corresponding spectrum of the Ramsey measurement for the NV-center used here is shown in fig. 39.a and fig. 39.b. The spectrum shows four lines whose occurrence is explained by a coupling to an adjacent ^{13}C which causes a splitting of $\approx$ 2.18 MHz. Thus the spectrum is the result of a superposition of two triplets. One was shifted to lower and the other to higher frequencies by $\approx$ 1.09 MHz. Since the hyperfine splitting due to the ^{13}C almost equals the splitting due to the ^{14}N, two lines of each triplet overlap, giving rise to the four lines in the spectrum. This is underlined by the intensities of the two central lines which are approximately of double height compared to the outer two lines.

In fig. 40.a the time domain signal of the Hahn echo and the CPMG sequences, with: 2, 4, 6 and 8 pulses, are shown. The number of accumulations were (with increasing number of refocusing pulses): 10^7, 10^6, $4 \cdot 10^5$, $4 \cdot 10^5$ and 10^6. The spectra are given in fig. 40.b. Exponential decays were subtracted from the time domain data before the spectra were calculated. The spectra show an increasing number of higher order peaks with increasing number of refocusing pulses. For CPMG-4 and -6 the higher order peaks appear at frequencies, which are integer multiples of the corresponding second peak (main peak). Additionally, a peak to the left of the main peak is observed which rises with increasing number of pulses. The origin of this peak is not clear.

The frequencies of the main (respectively the second) peaks are given in fig. 41 marked by *magenta* ellipsoids. A value at zero refo-

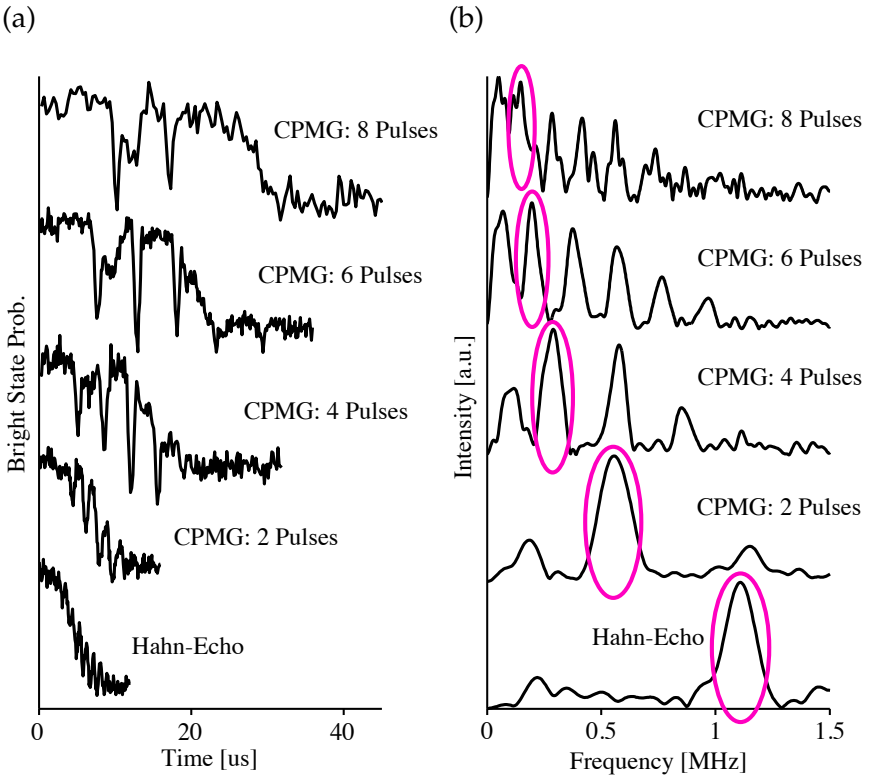

Figure 40: ESEEM of Hahn echo and CPMG decay. The ESEEM of the initial decays (cf. fig. 28) were measured and are shown in a). The spectra of the modulations are shown in b). The main peaks (respectively the second peaks) are marked by the *magenta* ellipsoids.

cusing pulses is included in the diagram which is given by the half of the ^{13}C hyperfine coupling obtained by the Ramsey measurement. The dashed line is a plot of the function:

$$f(x) = \frac{A_{\parallel}}{2 \cdot x}, \tag{23}$$

with the hyperfine interaction constant $A_{\parallel} = 2.18\,\text{MHz}$ and x the number of refocusing pulses. Thus the frequency of the main peak is reciprocally proportional to the number of pulses of the CPMG sequence. In fig. 42 the time constants of the first decays (*black* squares) and the modulation amplitudes (*magenta* asterisks) are shown. Analogous to the data presented in fig. 28 on page 66 the decay constants increase linearly with increasing number of refocusing pulses. The amplitude of the modulations also increases but saturates for more than 4 pulses.

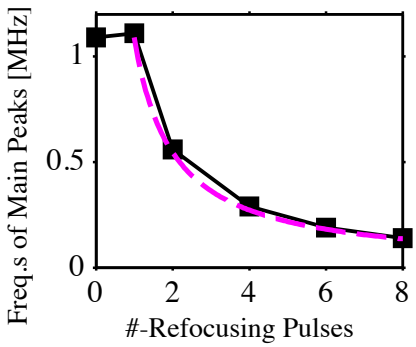

Figure 41: Frequencies of main maxima (resp. the second peaks) of fig. 40.b. The first data point is equal to the half of the hyperfine splitting which was obtained by the Ramsey measurement. The dashed line (*magenta*) is given by Ep. (23). Details are given in the text.

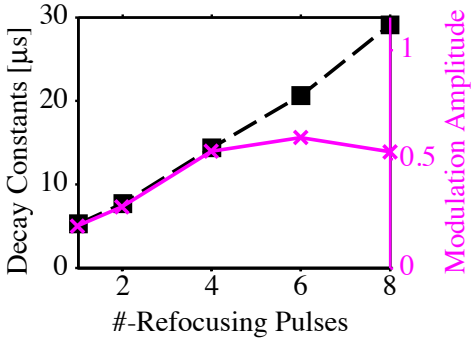

Figure 42: Decay constants (left axis, *black* squares) and modulation amplitudes (right axis, *magenta* asterisks) as function of the number of refocusing pulses.

6.2 CONCLUSIONS

We presented in this section ESEEM measurements obtained from single NV-centers. The modulations are caused by adjacent ^{13}C's which were coupled via hyperfine interaction to the NV-centers. The obtained ESEEM spectra show relations to the carbon hyperfine interaction constants, which we obtained from Ramsey spectra, with a proportionality factor of $\approx 1/2$. We showed that the CPMG sequence can be used as well to obtain ESEEM signals. The modulation frequencies and amplitudes showed a dependency on the number of refocusing pulses. While the modulation amplitudes saturate for more than 4 refocusing pulses, the main peaks of the modulation spectra had a dependency inversely proportional to the number of refocusing pulses. The spectra of the ESEEM signals in fig. 40 showed additionally higher order (> 2) peaks whose separations are equal to the frequency of the corresponding main peak. However, the origin of the peaks is not clear as well as the rising of the peaks to the left side of the main peaks. Further investigations e.g. with different orientations and strengths of the external magnetic field might help to clarify the shape of the ESEEM spectra. Hereby, ESEEM could become a useful tool to precisely determine the form of the hyperfine interaction between NV-centers and adjacent ^{13}C's.

7 FUTURE PROSPECTS

7.1 CONTROL OF NV NUCLEAR SPIN VIA ELECTRON SPIN

In order to implement complex quantum algorithms in quantum computers, long coherence times of the data stored in the qubits are very important. Because coherence times of nuclear spins are usually longer than those for electron spins, it might be advantageous to use hybrid systems consisting of electron and nuclear spins for qubit registers. In these systems the electron spins would be the actual qubits while the nuclear spins would act as a buffer to store the electron quantum states temporarily. It is essential to control the nuclear spin state to use it in a hybrid system. Usually, the dipole moments of nuclear spins are smaller by three orders of magnitude compared to electron spins. Thus usually radio frequency fields of high power are needed to reach sufficiently high Rabi frequencies which allow e.g. the transfer of the electron spin state to the nuclear spin within T_2^* of the electron spin. Besides the high radio frequency power a separate setup for the application of the radio frequency field is needed as well. For cases where high power is not desirable or not feasible, the nuclear spin could be controlled under certain circumstances via the manipulation of the electron spin state.

It is known that for spin systems where the electron and nuclear spins are coupled by a hyperfine tensor containing pseudo-secular terms, control of a nuclear spin via a electron spin is possible [99, 100]. The pseudo-secular terms of the hyperfine coupling are responsible for a dependency of the nuclear spin quantization axis on the electron spin state. Thus, the nuclear spin can be transferred into an arbitrary state by modifying the nuclear spin quantization axes through the electron spin. As shown in section 3 the hyperfine coupling between the electron and nuclear spin of the ^{14}NV-center does not contain pseudo-secular but non-secular terms because of its axial symmetry. But by exposing an axial symmetric hyperfine tensor to a magnetic field, which is tilted with respect to the symmetry axis, pseudo-secular hyperfine terms are obtained [101].

In this section an analytical derivation will be given that shows how a tilted magnetic field will affect the coupling between an electron $S = 1/2$ and a nuclear spin $I = 1$. Next the coupling between an electron spin $S = 1$ and nuclear spin $I = 1$ is analyzed numerically. In this case the entire Hamiltonian of the NV-center given in section 2.4.4 will be used. In the last subsection the controllability of the nuclear spin via the electron spin is shown by numerical simulations.

7.1.1 *Analytical Analysis: Spin S=1/2 with Nuclear Spin I=1*

In the following the NV electron spin is simplified by a pseudo-spin $S = 1/2$ which is coupled to a nuclear spin $I = 1$ via a hyperfine tensor of a diagonal form. Because of the reduction of the electron spin to a spin 1/2, the analysis can be done by geometric means. It is assumed that both spins are exposed to a tilted magnetic field. The tilt is with respect to the principal axis of the hyperfine tensor. The analytical derivations in this section are based on an example calculation of Ref. [101] (chapter 11.3, p. 521) which was given for an electron spin $S = 1/2$ and a nuclear spin $I = 1/2$.

The Hamiltonian for the coupled spin system is given by:

$$\begin{aligned} H &= g_e \mu_B B_z S_z + P I_z^2 - g_{14N} \mu_{14N} B_z I_z + \\ &\quad A_{xx} I_x S_x + A_{yy} I_y S_y + A_{zz} I_z S_z \,. \end{aligned} \tag{24}$$

The first term is the electron Zeeman interaction, the second and third terms are the nuclear quadrupole and Zeeman interactions. The last three terms are the components of the hyperfine interaction. The quantization axis of the nuclear spin is predominantly defined by the quadrupole interaction. For example for a field strength of 100 G the addition due to the nuclear-Zeeman interaction to the quadrupole splitting is in the order of 0.1%. Thus it is assumed that the magnetic field has no influence on the quantization axis of the nuclear spin and the non-secular terms of the nuclear Zeeman interaction will be neglected hereinafter. On the other hand, the electron-spin and its quantization axis are influenced by the magnetic field. It is further assumed that the external field seen by the electron is bigger than the hyperfine interaction field, thus its quantization axis coincides with the direction of the external field. The relation of the electron and nuclear spin operators for the aligned and tilted cases are given by:

$$\begin{aligned} S_x &= S_{x'} \cos\theta + S_{z'} \sin\theta \\ S_y &= S_{y'} \\ S_z &= S_{z'} \cos\theta - S_{x'} \sin\theta \\ \\ I_x &= I_{x'} \\ I_y &= I_{y'} \\ I_z &= I_{z'} \,. \end{aligned} \tag{25}$$

Here, it is assumed that the magnetic field has no components in y direction just along x and z. S_x, S_y and S_z are the electron spin operators in the principal coordinate system defined by the hyperfine tensor. $S_{x'}$, $S_{y'}$ and $S_{z'}$ are the electron spin operators in the tilted frame

defined by the magnetic field. θ is the angle between the magnetic field and the z axis of the hyperfine tensor. As already mentioned, it is assumed that the nuclear spin quantization axis does not change due to the magnetic field. Inserting the principal axes transformation of Ep. (25) into Eq. (24) yields the new Hamiltonian for the tilted case:

$$\begin{aligned} H(\theta) &= g_e \mu_B B_{z'}(S_{z'}\cos\theta - S_{x'}\sin\theta) + PI_{z'}^2 - g_{14N}\mu_{14N}B_{z'}I_{z'}\cos\theta \\ &\quad + A_{xx}I_{x'}(S_{x'}\cos\theta + S_{z'}\sin\theta) + A_{yy}I_{y'}S_{y'} \\ &\quad + A_{zz}I_{z'}(S_{z'}\cos\theta - S_{x'}\sin\theta) \\ &= g_e \mu_B B_{z'}S_{z'} + PI_{z'}^2 - g_{14N}\mu_{14N}B_{z'}I_{z'}\cos\theta \\ &\quad + A_{xx}I_{x'}S_{x'}\cos\theta + A_{xx}I_{x'}S_{z'}\sin\theta + A_{yy}I_{y'}S_{y'} \\ &\quad + A_{zz}I_{z'}S_{z'}\cos\theta - A_{zz}I_{z'}S_{x'}\sin\theta\,. \end{aligned}$$

For the nuclear Zeeman interaction only the component of the external magnetic field projected onto the z-axis of the nuclear spin principle coordinate system was taken into account. Non-secular terms containing $S_{x'}$ and $S_{y'}$ will be neglected because they do not contribute to electron spin dependent field changes of the nuclear spin:

$$\begin{aligned} H(\theta) &= g_e \mu_B B_{z'}S_{z'}\cos\theta + PI_{z'}^2 - g_{14N}\mu_{14N}B_{z'}I_{z'}\cos\theta \\ &\quad + A_{xx}I_{x'}S_{z'}\sin\theta + A_{zz}I_{z'}S_{z'}\cos\theta\,. \end{aligned}$$

The last two terms represent an electron spin depended field acting additionally to the external magnetic field on the nuclear spin which can thus be expressed as:

$$\begin{aligned} B_{x'}(m_s) &= A_{xx}\sin\theta \cdot m_s \\ B_{y'}(m_s) &= 0 \\ B_{z'}(m_s) &= P - g_{14N}\mu_{14N}B_{z'}\cos\theta + A_{zz}\cos\theta \cdot m_s\,. \end{aligned}$$

For a precise analysis the zero-field splitting of the electron has to be taken into account. Of course, this reduces the influence of the external magnetic field on the quantization axis of the electron. But still, because the electron spin reacts more sensitive on the external magnetic field than the nuclear spin (if the zero-field and quadrupole splittings are taken into account), the fundamental behavior is equal to the case without the zero field splitting.

7.1.2 *Numerical Analysis*

Due to an external magnetic field, which is not aligned with the principal axis of the hyperfine tensor resp. the NV-center's symmetry axis, the eigenstates of a spin are given by superpositions of the unperturbed eigenstates. Hence, it is possible to excite transitions which

would be 'forbidden' in the case of an aligned field. By diagonalizing the Hamiltonian of the spin system and calculating the corresponding eigenstates the transition probability between different states can be given quantitatively by using Eq. (12) of sec. 2.5.3. In the following this analysis was done numerically by using the NV Hamiltonian introduced in section 2.4:

$$H_{tot} = H_e + H_{14N} + H_{HF_{14N}} \,. \tag{26}$$

The first term H_e is the electron Hamiltonian including the zero-field splitting and Zeeman interaction. The second term H_{14N} is the nuclear Hamiltonian including the quadrupole splitting and the Zeeman interaction. The last term $H_{HF_{14N}}$ is the hyperfine interaction Hamiltonian. The terms are specified by:

$$\begin{aligned} H_e &= D\left[S_z^2 - \frac{1}{3}S\left(S+1\right)\right] + \\ &\quad g_e\mu_B\left(B_xS_x + B_yS_y + B_zS_z\right) \\ H_{14N} &= P\left[I_{z,14N}^2 - \frac{1}{3}I_{14N}\left(I_{14N}+1\right)\right] - \\ &\quad g_{14N}\mu_{14N}\left(B_xI_{x,14N} + B_yI_{y,14N} + B_zI_{z,14N}\right) \\ H_{HF_{14N}} &= A_{||_{14N}}S_zI_{z,14N} + A_{\perp_{14N}}\left(S_xI_{x,14N} + S_yI_{y,14N}\right) \,. \end{aligned}$$

The unperturbed eigenvalues of the Hamiltonian H_{tot} (Eq. 26), neglecting the non-secular contribution of the hyperfine interaction and of the Zeeman interactions, are given in section 2.5.1 by Eq. (10). With respect to the size, we rewrite the eigenvalues (for a magnetic field of 70 G) in ascending order denoted by $E_i^{'}$ in units of frequency (E_i denotes the prior order).

$$|+1,\ 0\rangle: \quad E_1^{'} = E_8 = \frac{D-2P}{3} + c_eB_z \tag{27}$$

$$|+1,+1\rangle: \quad E_2^{'} = E_9 = \frac{D+P}{3} + A_{\|_{14N}} + \left(c_e - c_{14N}\right)B_z \tag{28}$$

$$|+1,-1\rangle: \quad E_3^{'} = E_7 = \frac{D+P}{3} - A_{\|_{14N}} + \left(c_e + c_{14N}\right)B_z \tag{29}$$

$$|-1,\ 0\rangle: \quad E_4^{'} = E_2 = \frac{D-2P}{3} - c_eB_z \tag{30}$$

$$|-1,-1\rangle: \quad E_5^{'} = E_1 = \frac{D+P}{3} + A_{\|_{14N}} - \left(c_e - c_{14N}\right)B_z \tag{31}$$

$$|-1,+1\rangle: \quad E_6^{'} = E_3 = \frac{D+P}{3} - A_{\|_{14N}} - \left(c_e + c_{14N}\right)B_z \tag{32}$$

$$|\ 0,\ \ 0\rangle : \quad E_7^{'} = \quad E_5 = \quad -\frac{2}{3}(D+P) \tag{33}$$

$$|\ 0,-1\rangle : \quad E_8^{'} = \quad E_4 = \quad -\frac{2D-P}{3} + c_{14N}B_z \tag{34}$$

$$|\ 0,+1\rangle : \quad E_9^{'} = \quad E_6 = \quad -\frac{2D-P}{3} - c_{14N}B_z \tag{35}$$

The analysis of the entire Hamiltonian is done numerically. The obtained eigenvalues are sorted and assigned to the non-perturbed eigenvalues to figure out which quantum states correspond to the transitions. In the following the numbers (i,j) indicate the indices of the non-perturbed eigenvalues $E_i^{'} \leftrightarrow E_j^{'}$.

For the analysis the numerical computing software MATLAB[1] was used. As mentioned above, first the Hamiltonian was numerically diagonalized and the transition frequencies between all energy levels were calculated. This was done for multiple orientations of the magnetic field with respect to the NV symmetry axis. The field was rotated in the zx-plane alone since the Hamiltonian Eq. (26) is of axial symmetry. Subsequently the corresponding probabilities of the transitions were calculated using Eq. (12). The results for the transition matrix elements were plotted into a 3D graph which is shown in fig. 43. The x-axis gives the field tilt θ, the y-axis the transition frequency and the z-axis the absolute value of the transition matrix element. In this figure only transitions with frequencies above 2.6 GHz are shown. The *black* lines show the transition matrix elements of the electron spin transitions $|m_s = +1\rangle \leftrightarrow |m_s = 0\rangle$ and the transition $|m_s = -1\rangle \leftrightarrow |m_s = 0\rangle$ are given by the *blue* lines. For the chosen field orientation the first (*black* lines) are higher in frequency. The transition frequencies and matrix elements for three excitations matrices are shown in the figure. Figure 43.a shows the results for an excitation with $\left(S_x + S_y\right)/2$, fig. 43.b with S_x and fig. 43.c with S_y.

An excitation due to a field $\left(S_x + S_y\right)/2$ has similar results on both electron spin transitions $|m_s = +1\rangle \leftrightarrow |m_s = 0\rangle$ (*black* lines) and $|m_s = -1\rangle \leftrightarrow |m_s = 0\rangle$ (*blue* lines). All three excitation fields have in common that the transition matrix elements of $(4,8)$, $(4,9)$, $(5,7)$, $(6,7)$ and $(1,8)$, $(1,9)$, $(2,7)$, $(3,7)$ are barely affected due to the tilted field. For these transitions the quantum numbers change by $\Delta m_S = \pm 1$ and $\Delta m_I = \pm 1$ (cf. tab. 2).

For an excitation with S_x the transitions $(5,8)$ and $(6,9)$ reach a maximum for a tilt angle of $\approx 83°$ but than start to decrease and reach a minimum at 90° (see fig. 43.b). The values of the transition matrix elements for $(2,9)$ and $(3,8)$ continuously increase. For these transitions the quantum numbers change by $\Delta m_S = \pm 1$ and $\Delta m_I = \pm 2$. The transition matrix elements of $(1,7)$ increases while $(2,8)$ and $(3,9)$

1 MATLAB R2010a, Trademark of The MathWorks, Inc.

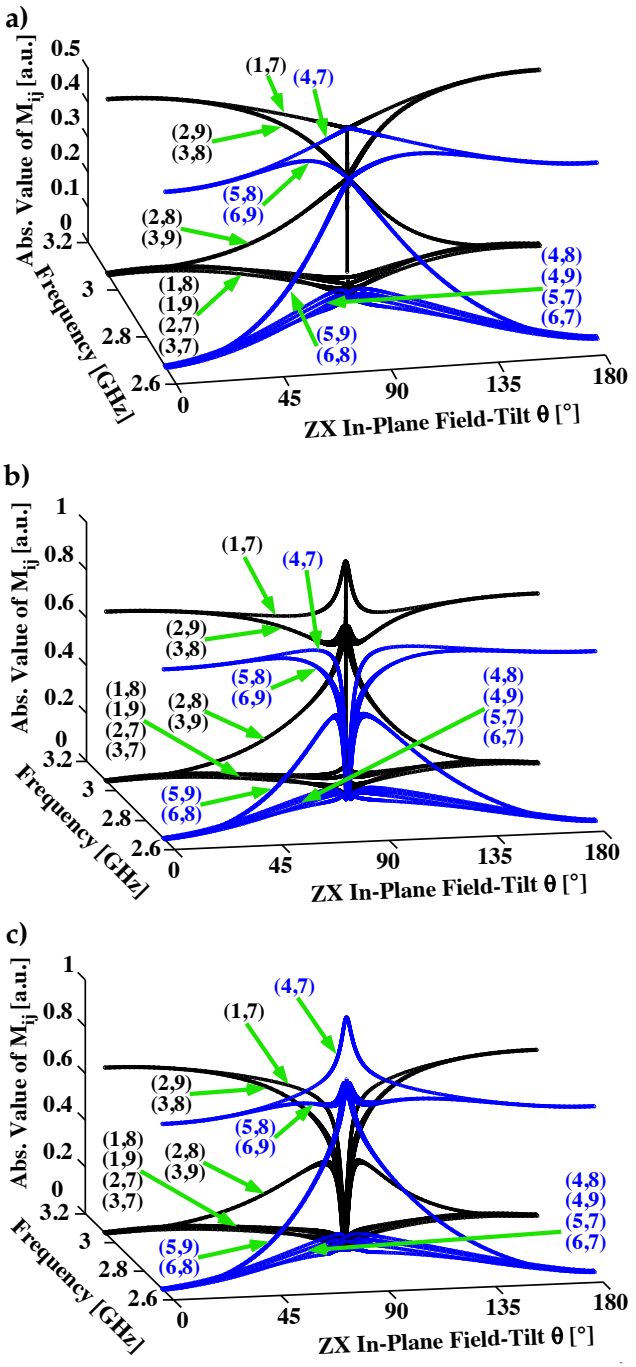

Figure 43: Simulation of transition frequencies and absolute values of transition matrix elements $M_{ij} = \langle e_i|M|e_j\rangle$ for the NV electron spin for different magnetic field tilts. The magnetic field had a constant absolute strength of 70 G and was tilted in the zx-plane with tilt angles θ ranging from 0° to 180°. No field was applied along the y-axis. Only transitions above 2.6 GHz are shown. The numbers in the brackets (i,j) assign the transitions to the corresponding non-perturbed energy levels $E_i' \leftrightarrow E_j'$. Analytical expressions for these are given by Eq. (27) to (35). The transition matrix elements are given for different excitation matrices: in (a) for $\left(S_x + S_y\right)/2$, in (b) for S_x and in (c) for S_y.

first decrease slightly but reach a maximum for both at $\theta = 90°$. The matrix elements of $(4,7)$, $(6,8)$ and $(5,9)$ decrease with increasing tilt

Transition	Quantum states	Change of Quantum numbers
Allowed Transitions:		
(1, 7)	$\|+1, \quad 0\rangle \leftrightarrow \|\quad 0, \quad 0\rangle$	$\Delta m_S = \pm 1, \Delta m_I = 0$
(4, 7)	$\|-1, \quad 0\rangle \leftrightarrow \|\quad 0, \quad 0\rangle$	$\Delta m_S = \pm 1, \Delta m_I = 0$
(2, 9)	$\|+1, +1\rangle \leftrightarrow \|\quad 0, +1\rangle$	$\Delta m_S = \pm 1, \Delta m_I = 0$
(3, 8)	$\|+1, -1\rangle \leftrightarrow \|\quad 0, -1\rangle$	$\Delta m_S = \pm 1, \Delta m_I = 0$
(5, 8)	$\|-1, -1\rangle \leftrightarrow \|\quad 0, -1\rangle$	$\Delta m_S = \pm 1, \Delta m_I = 0$
(6, 9)	$\|-1, +1\rangle \leftrightarrow \|\quad 0, +1\rangle$	$\Delta m_S = \pm 1, \Delta m_I = 0$
Forbidden Transitions with strongly increasing probability:		
(3, 9)	$\|+1, -1\rangle \leftrightarrow \|\quad 0, +1\rangle$	$\Delta m_S = \pm 1, \Delta m_I = \pm 2$
(2, 8)	$\|+1, +1\rangle \leftrightarrow \|\quad 0, -1\rangle$	$\Delta m_S = \pm 1, \Delta m_I = \pm 2$
(5, 9)	$\|-1, -1\rangle \leftrightarrow \|\quad 0, +1\rangle$	$\Delta m_S = \pm 1, \Delta m_I = \pm 2$
(6, 8)	$\|-1, +1\rangle \leftrightarrow \|\quad 0, -1\rangle$	$\Delta m_S = \pm 1, \Delta m_I = \pm 2$
Forbidden Transitions with weakly increasing probability:		
(4, 8)	$\|-1, \quad 0\rangle \leftrightarrow \|\quad 0, -1\rangle$	$\Delta m_S = \pm 1, \Delta m_I = \pm 1$
(4, 9)	$\|-1, \quad 0\rangle \leftrightarrow \|\quad 0, +1\rangle$	$\Delta m_S = \pm 1, \Delta m_I = \pm 1$
(5, 7)	$\|-1, -1\rangle \leftrightarrow \|\quad 0, \quad 0\rangle$	$\Delta m_S = \pm 1, \Delta m_I = \pm 1$
(6, 7)	$\|-1, +1\rangle \leftrightarrow \|\quad 0, \quad 0\rangle$	$\Delta m_S = \pm 1, \Delta m_I = \pm 1$
(1, 8)	$\|+1, \quad 0\rangle \leftrightarrow \|\quad 0, -1\rangle$	$\Delta m_S = \pm 1, \Delta m_I = \pm 1$
(1, 9)	$\|+1, \quad 0\rangle \leftrightarrow \|\quad 0, +1\rangle$	$\Delta m_S = \pm 1, \Delta m_I = \pm 1$
(2, 7)	$\|+1, +1\rangle \leftrightarrow \|\quad 0, \quad 0\rangle$	$\Delta m_S = \pm 1, \Delta m_I = \pm 1$
(3, 7)	$\|+1, -1\rangle \leftrightarrow \|\quad 0, \quad 0\rangle$	$\Delta m_S = \pm 1, \Delta m_I = \pm 1$

Table 2: Level indices, quantum states and the change of quantum numbers. The left column shows the indices of the non-perturbed eigenvalues given by Eq. (27) to (35). The center column shows the quantum numbers belonging the corresponding state. The column to the right shows the change of quantum numbers of the transitions.

angle and reach a minimum for $\theta = 90°$. For these transitions the quantum numbers change by $\Delta m_S = \pm 1$ and $\Delta m_I = 0$. For an excitation with S_y the overall behavior of the transition matrix elements is similar to the case described above but the transitions $|m_S = +1\rangle \leftrightarrow |m_S = 0\rangle$ and $|m_S = -1\rangle \leftrightarrow |m_S = 0\rangle$ are interchanged (cf. fig. 43.b and fig. 43.c).

The simulation results indicate that the number of transitions with absolute values > 0 of the transition matrix elements increases if the NV-center is exposed to a tilted magnetic field. As was shown the

values of the matrix elements differ depending on the quantum numbers which flip during the the excitation process. This points out that a control of the nuclear spin of the NV-center via its electron spin is feasible as will be underlined by the simulation results which are presented in the next section.

7.1.3 *NV Nuclear Spin Control via Electron Spin*

Previous sections have shown that for an tilted external magnetic field the effective field acting on the NV nuclear spin depends on the electron spin. In this case the control of the nuclear spin via the electron spin is feasible as was shown by *Hodges* et al. [99] and *Zhang* et al. [100]. Since the order of the control time depends on the size of the hyperfine interaction terms (for the case of the NV-center, they are in the range of a few MHz) this is a suitable technique. Thus, additional equipment and high power in the radio frequency range, which is necessary to control the nuclear spin sufficiently fast but is not always feasible, is not needed. We show simulation results which emphasize the controllability of the ^{14}N nuclear spin via the NV electron spin where the spin population of one nuclear spin sub-state will be increased.

The time window of the simulation, which corresponds to the duration of the pulse, was segmented and a set of density matrices ρ_n^i for each pulse segment was generated. The index n indicates the n-th pulse segment and i indicates the i-th configuration of frequency ω and phase φ of the excitation field. The density matrices were calculated using:

$$\rho_n^i(t) = e^{-i\int(H+H_1)dt/\hbar}\rho_{n-1}e^{i\int(H+H_1)dt/\hbar} ,$$

which follows from the *von Neumann equation*. H is the entire Hamiltonian of the NV-center given by Eq. (26) without using the *rotating wave approximation*. The excitation field is given by:

$$H_1 = \frac{1}{\sqrt{2}} 2\pi\nu_1 \cos(\omega t + \varphi) S_x .$$

ν_1 is the Rabi frequency and determines the field strength. For the n-th pulse segment, one density matrix of the generated set was chosen for generating the set of density matrices for the next pulse segment $(n+1)$. The selection criterion for the density matrices was to reach a rising of the population of the $|m_I = 0\rangle$ nuclear sub-state. Figure 44 shows the results of two simulations. We used the following parameter settings for the simulations:

- the magnetic field tilt with respect to the NV symmetry axis was 45°,
- two frequencies were used, one was resonant with the $|0\rangle \leftrightarrow |-1\rangle$ transition the other with the $|0\rangle \leftrightarrow |+1\rangle$ transition,

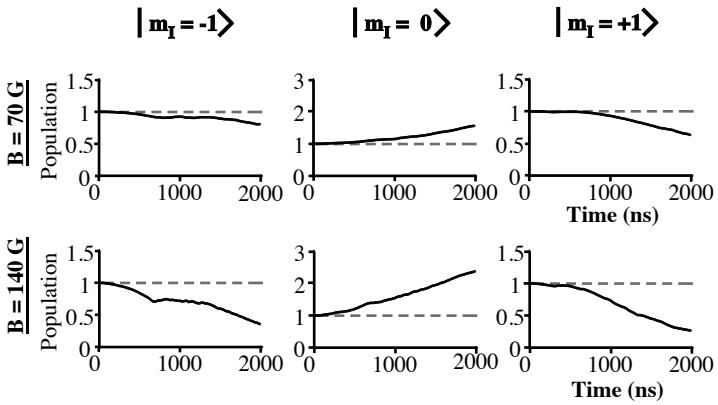

Figure 44: Simulation results of polarizing the ^{14}N nuclear spin of a NV-center by strongly modulating the electron spin state. The upper row shows results of a simulation for a magnetic field strength of $B = 70$ G, the lower row for $B = 140$ G. The columns show the populations of the different nuclear spin sub-states. The dotted line marks the initial equilibrium population. A population of 1 was assumed for the nuclear spin sub-states of the initial density matrix.

- for each frequency a set of 20 pulses with different phases (equally distributed from 0 to 2π) were applied,
- Hyperfine couplings of $A_{\parallel} = 2.15$ MHz and $A_{\perp} = 2.3$ MHz were assumed,
- a Rabi frequency of 40 MHz was assumed.

It is further assumed that the electron spin is fully polarized in the bright state with a population of $|0\rangle\langle 0| = 1$ and that the nuclear spin is depolarized. For the sake of simplicity the nuclear spin sub-state populations are given by 1 (instead of 1/3). Thus in case of a polarized nuclear spin a maximal state population of 3 can be reached. The initial density matrix is given by:

$$\rho_0 = \underbrace{\begin{pmatrix} 0 & 0 & 0 \\ 0 & 1 & 0 \\ 0 & 0 & 0 \end{pmatrix}}_{\rho_0^e} \otimes \underbrace{\begin{pmatrix} 1 & 0 & 0 \\ 0 & 1 & 0 \\ 0 & 0 & 1 \end{pmatrix}}_{\rho_0^n}.$$

Here, the first matrix is the electron spin density and the second the nuclear spin density matrix. The ordering of the quantum numbers of the density matrices is given in section A.2.

Figure 44 presents the results of two simulations which were aimed to increase the polarization of the nuclear spin sub-state $|m_I = 0\rangle$. The simulations were done for two different magnetic field strengths. The curves in the upper row show the nuclear spin population for an absolute field strength of 70 G and the lower row for 140 G. The

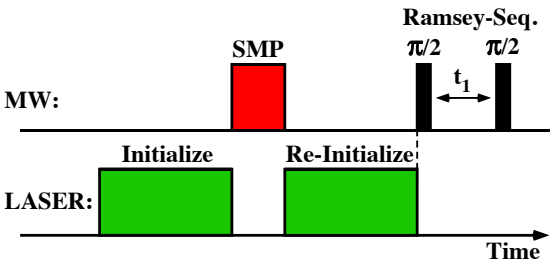

Figure 45: Proposal of a sequence to measure the nuclear spin polarization after application of a SMP. The *red* rectangle indicates the application of the strongly modulating pulse and the *green* rectangles indicate pulses of the laser to polarize the electron spin system. To verify the polarization of the ^{14}N nuclear spin, a Ramsey sequence could be used.

columns indicate the populations for the nuclear spin states. As can be seen the rate of population change depends on the strength of the external magnetic field and increases with it.

7.1.4 *Discussion and Conclusion*

It has been shown that the effective magnetic field, which acts on the nuclear spin, depends on the electron spin state, if both spins are exposed to an external magnetic field which is tilted with respect to the NV symmetry axis. It was also shown by numerical simulations, using the entire time-dependent Hamiltonian of the NV-center, that it is possible to polarize the ^{14}N nuclear spin if a strongly modulating pulse (SMP) is used. The simulation results for two different field strengths were shown which indicate that the rate of change of population increases with the strength of the magnetic field. With the parameters used in the simulations the partial polarization of the nuclear spin was achieved on a time scale of 2 μs which would be in the range of the T_2^* time of NV-centers in natural abundance diamond. The usage of more sophisticated algorithms from optimal control theory like GRAPE or KROTOV [102, 103] could probably generate faster resp. more powerful SMPs. With these algorithms implementation of an arbitrary control operations would be feasible.

To verify the polarization of the nuclear spin, we propose to use the Ramsey sequence which follows the SMP and a laser pulse which is needed to reinitialize the electron spin. A scheme of the proposed sequence is given in fig. 45.

A

APPENDIX

A.1 ORIENTATION DEPENDENT ODMR SPECTRA

One of the most basic measurements with microwave excitation which can be performed on a NV electron spin is the continuous-wave (CW-) ODMR experiment. Here, the frequency of the microwave excitation is swept continuously through a frequency range, and the NV center is irradiated simultaneously by laser light. This sequence is easy to implement and returns quickly information on e.g. the magnetic field strength which is projected to the NV-symmetry axis and the presence or absence of strongly coupled ^{13}C. The advantage of the sequence is that it is fast, so it does take a minute or less to measure a plot as shown in figure 46. The disadvantage of this sequence is that the spectral resolution is limited due to power broadening of the continuous microwave excitation and laser illumination. Higher resolution is possible by reducing the excitation powers but this is at the cost of an increased measurement time due to the reduced signal intensity. Figure 46 shows the CW-ODMR spectra of two differently orientated NV-centers which were located in the same spot of the confocal setup.

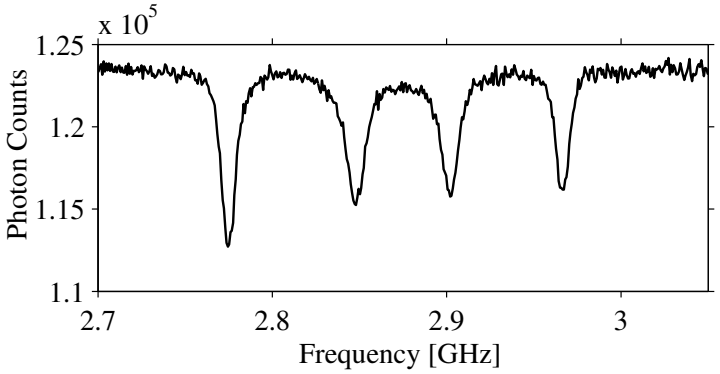

Figure 46: CW-ODMR spectrum of two single NV-centers possessing different orientations with respect to an external magnetic field. Both NV-centers were located within the diffraction limited focal spot of the confocal setup.

A.2 DENSITY MATRIX

The *density matrix formalism* is a convenient way to describe the state of an ensemble of identical quantum systems. But it can also be used to describe the state and evolution of a single quantum system as will be done here. For a single quantum system which is in a state given by the state vector $|\Phi\rangle = \sum_i a_i |\psi_i\rangle$ the density matrix ρ is obtained by:

$$\begin{aligned} \rho &= |\Phi\rangle \langle\Phi| \\ &= \sum_{i,j} a_i a_j^* |\psi_i\rangle \langle\psi_j| \\ &= \sum_{i,j} c_{ij} |\psi_i\rangle \langle\psi_j| \ . \end{aligned}$$

Here, $|\psi_i\rangle$ are the i-th eigenstates of the quantum system. For $i = j$ the coefficients c_{ii} are called *populations* and describe the probability of the system of being in the corresponding eigenstate. The total population is normalized i.e. $\sum_i c_{ii} = 1$. For $i \neq j$ the coefficients are called *coherences* and describe a superposition of eigenstates.

Within this thesis we use the density matrix with the following notation for the NV electron as well as ^{14}N nuclear spin:

$$\rho^{e,n} = \begin{pmatrix} |-1\rangle \\ |\ 0\rangle \\ |+1\rangle \end{pmatrix} \cdot \begin{pmatrix} \langle -1| & \langle\ 0| & \langle +1| \end{pmatrix}$$

A.3 DQC-CPMG DATA

The decay constants of the CPMG measurement for the DQC shown in fig. 35 are gained by fitting the function:

$$f(t) = a \cdot \exp\left(-t/dt\right)^4 + c \ ,$$

to the data sets. a is the amplitude, c the offset and dt the decay constant. The raising parts of the data sets were ignored during the fitting procedure. All measurements showed offsets in the range of 0.26 to 0.33 and amplitudes in the range of 0.15 to 0.25. The decay curves and the fitting results for every data set are shown in fig. 47. The fitted functions are given by the *red* curves.

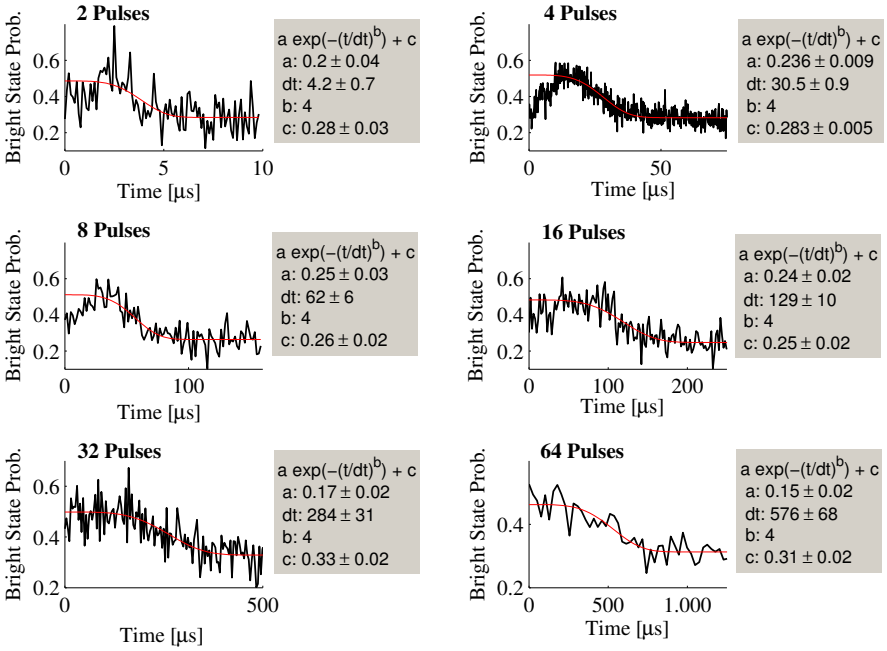

Figure 47: Decay curves of the CPMG measurements of the double quantum coherences. The insets show the functions, which were fitted to the data sets, and the parameters following from the fittings. The *red* curves show the fitted functions. The value of the exponent 'b' of the exponential function was fixed for all the fits.

BIBLIOGRAPHY

[1] R. P. Feynman. Simulating physics with computers. *International Journal of Theoretical Physics*, 21(6-7):467–488, 1982.

[2] L. M. K. Vandersypen, M. Steffen, G. Breyta, C. S. Yannoni, M. H. Sherwood, and I. L. Chuang. Experimental realization of shor's quantum factoring algorithm using nuclear magnetic resonance. *Nature*, 414(6866):883–887, December 2001.

[3] E. Lucero, R. Barends, Y. Chen, J. Kelly, M. Mariantoni, A. Megrant, P. O'Malley, D. Sank, A. Vainsencher, J. Wenner, T. White, Y. Yin, A. N. Cleland, and J. M. Martinis. Computing prime factors with a josephson phase qubit quantum processor. *Nat. Phys.*, 8(10):719–723, October 2012.

[4] E. Martin-Lopez, A. Laing, T. Lawson, R. Alvarez, X.-Q. Zhou, and J. L. O'Brien. Experimental realization of shor's quantum factoring algorithm using qubit recycling. *Nat. Photon.*, 6(11):773–776, November 2012.

[5] D. P. DiVincenzo. The physical implementation of quantum computation. *Fortschr. Phys.*, 48(9-11):771–783, September 2000.

[6] D. D. Awschalom, L. C. Bassett, A. S. Dzurak, E. L. Hu, and J. R. Petta. Quantum spintronics: Engineering and manipulating atom-like spins in semiconductors. *Science*, 339(6124):1174–1179, March 2013.

[7] F. Jelezko and J. Wrachtrup. Single defect centres in diamond: A review. *Physica Status Solidi (a)*, 203(13):3207–3225, 2006.

[8] J. Meijer, B. Burchard, M. Domhan, C. Wittmann, T. Gaebel, I. Popa, F. Jelezko, and J. Wrachtrup. Generation of single color centers by focused nitrogen implantation. *Appl. Phys. Lett.*, 87(26):261909–3, December 2005.

[9] D. M. Toyli, C. D. Weis, G. D. Fuchs, T. Schenkel, and D. D. Awschalom. Chip-scale nanofabrication of single spins and spin arrays in diamond. *Nano Lett.*, 10(8):3168–3172, July 2010.

[10] R. P. Mildren, J. E. Downes, J. D. Brown, B. F. Johnston, E. Granados, D. J. Spence, A. Lehmann, L. Weston, and A. Bramble. Characteristics of 2-photon ultraviolet laser etching of diamond. *Opt. Mater. Express*, 1(4):576–585, August 2011.

[11] M. V. Gurudev Dutt, L. Childress, L. Jiang, E. Togan, J. Maze, F. Jelezko, A. S. Zibrov, P. R. Hemmer, and M. D. Lukin. Quantum register based on individual electronic and nuclear spin qubits in diamond. *Science*, 316(5829):1312–1316, June 2007.

[12] P. Cappellaro, L. Jiang, J. S. Hodges, and M. D. Lukin. Coherence and control of quantum registers based on electronic spin in a nuclear spin bath. *Phys. Rev. Lett.*, 102(21):210502, May 2009.

[13] P. Neumann, R. Kolesov, B. Naydenov, J. Beck, F. Rempp, M. Steiner, V. Jacques, G. Balasubramanian, M. L. Markham, D. J. Twitchen, S. Pezzagna, J. Meijer, J. Twamley, F. Jelezko, and J. Wrachtrup. Quantum register based on coupled electron spins in a room-temperature solid. *Nat. Phys.*, 6(4):249–253, April 2010.

[14] J. R. Maze, P. L. Stanwix, J. S. Hodges, S. Hong, J. M. Taylor, P. Cappellaro, L. Jiang, M. V. Gurudev Dutt, E. Togan, A. S. Zibrov, A. Yacoby, R. L. Walsworth, and M. D. Lukin. Nanoscale magnetic sensing with an individual electronic spin in diamond. *Nature*, 455(7213):644–647, October 2008.

[15] P. Maletinsky, S. Hong, M. S. Grinolds, B. Hausmann, M. D. Lukin, R. L. Walsworth, M. Loncar, and A. Yacoby. A robust scanning diamond sensor for nanoscale imaging with single nitrogen-vacancy centres. *Nat. Nano.*, 7(5):320–324, May 2012.

[16] L. Rondin, J.-P. Tetienne, P. Spinicelli, C. Dal Savio, K. Karrai, G. Dantelle, A. Thiaville, S. Rohart, J.-F. Roch, and V. Jacques. Nanoscale magnetic field mapping with a single spin scanning probe magnetometer. *Appl. Phys. Lett.*, 100(15):153118–4, April 2012.

[17] F. Dolde, H. Fedder, M. W. Doherty, T. Nobauer, F. Rempp, G. Balasubramanian, T. Wolf, F. Reinhard, L. C. L. Hollenberg, F. Jelezko, and J. Wrachtrup. Electric-field sensing using single diamond spins. *Nat. Phys.*, 7(6):459–463, June 2011.

[18] S. Hong, M. S. Grinolds, L. M. Pham, D. Le Sage, L. Luan, R. L. Walsworth, and A. Yacoby. Nanoscale magnetometry with nv centers in diamond. *MRS Bulletin*, 38(02):155–161, 2013.

[19] V. M. Acosta, E. Bauch, M. P. Ledbetter, A. Waxman, L.-S. Bouchard, and D. Budker. Temperature dependence of the nitrogen-vacancy magnetic resonance in diamond. *Phys. Rev. Lett.*, 104(7):070801, February 2010.

[20] X.-D. Chen, C.-H. Dong, F.-W. Sun, C.-L. Zou, J.-M. Cui, Z.-F. Han, and G.-C. Guo. Temperature dependent energy level shifts of nitrogen-vacancy centers in diamond. *Appl. Phys. Lett.*, 99(16):161903–3, October 2011.

[21] D. M. Toyli, D. J. Christle, A. Alkauskas, B. B. Buckley, C. G. Van de Walle, and D. D. Awschalom. Measurement and control of single nitrogen-vacancy center spins above 600 k. *Phys. Rev. X*, 2(3):031001, July 2012.

[22] I. Niemeyer, J. H. Shim, J. Zhang, D. Suter, T. Taniguchi, T. Teraji, H. Abe, S. Onoda, T. Yamamoto, T. Ohshima, J. Isoya, and F. Jelezko. Broadband excitation by chirped pulses: application to single electron spins in diamond. *New Journal of Physics*, 15(3):033027, 2013.

[23] J. H. Shim, I. Niemeyer, J. Zhang, and D. Suter. Robust dynamical decoupling for arbitrary quantum states of a single nv center in diamond. *Europhys. Lett.*, 99:40004, 2012.

[24] H. B. Dyer, F. A. Raal, L. Du Preez, and J. H. N. Loubser. Optical absorption features associated with paramagnetic nitrogen in diamond. *Philos. Mag.*, 11(112):763–774, April 1965.

[25] J. Walker. Optical absorption and luminescence in diamond. *Reports on Progress in Physics*, 42(10):1605, 1979.

[26] T. Teraji, T. Taniguchi, S. Koizumi, K. Watanabe, M. Liao, Y. Koide, and J. Isoya. Chemical vapor deposition of ^{12}c isotopically enriched polycrystalline diamond. *Jpn. J. Appl. Phys.*, 51:090104, 2012.

[27] A. Gali, M. Fyta, and E. Kaxiras. Ab initio supercell calculations on nitrogen-vacancy center in diamond: Electronic structure and hyperfine tensors. *Phys. Rev. B*, 77(15):155206, April 2008.

[28] K. Beha, A. Batalov, N. B. Manson, R. Bratschitsch, and A. Leitenstorfer. Optimum photoluminescence excitation and recharging cycle of single nitrogen-vacancy centers in ultrapure diamond. *Phys. Rev. Lett.*, 109(9):097404, August 2012.

[29] N. Aslam, G. Waldherr, P. Neumann, F. Jelezko, and J. Wrachtrup. Photo-induced ionization dynamics of the nitrogen vacancy defect in diamond investigated by single-shot charge state detection. *New Journal of Physics*, 15(1):013064, 2013.

[30] L. Rondin, G. Dantelle, A. Slablab, F. Grosshans, F. Treussart, P. Bergonzo, S. Perruchas, T. Gacoin, M. Chaigneau, H.-C. Chang, V. Jacques, and J.-F. Roch. Surface-induced charge state conversion of nitrogen-vacancy defects in nanodiamonds. *Phys. Rev. B*, 82(11):115449, September 2010.

[31] Y. Ma, M. Rohlfing, and A. Gali. Excited states of the negatively charged nitrogen-vacancy color center in diamond. *Phys. Rev. B*, 81(4):041204, January 2010.

[32] L. J. Rogers, S. Armstrong, M. J. Sellars, and N. B. Manson. Infrared emission of the nv centre in diamond: Zeeman and uniaxial stress studies. *New Journal of Physics*, 10(10):103024, 2008.

[33] V. M. Acosta, A. Jarmola, E. Bauch, and D. Budker. Optical properties of the nitrogen-vacancy singlet levels in diamond. *Phys. Rev. B*, 82(20):201202, November 2010.

[34] J. Harrison, M. J. Sellars, and N. B. Manson. Measurement of the optically induced spin polarisation of n-v centres in diamond. *Diamond Relat. Mater.*, 15:586–588, 2006.

[35] M. Steiner, P. Neumann, J. Beck, F. Jelezko, and J. Wrachtrup. Universal enhancement of the optical readout fidelity of single electron spins at nitrogen-vacancy centers in diamond. *Phys. Rev. B*, 81(3):035205, January 2010.

[36] R. J. Epstein, F. M. Mendoza, Y. K. Kato, and D. D. Awschalom. Anisotropic interactions of a single spin and dark-spin spectroscopy in diamond. *Nat. Phys.*, 1(2):94–98, November 2005.

[37] P. Neumann, R. Kolesov, V. Jacques, J. Beck, J. Tisler, A. Batalov, L. Rogers, N. B. Manson, G. Balasubramanian, F. Jelezko, and J. Wrachtrup. Excited-state spectroscopy of single nv defects in diamond using optically detected magnetic resonance. *New Journal of Physics*, 11(1):013017, 2009.

[38] M. W. Doherty, F. Dolde, H. Fedder, F. Jelezko, J. Wrachtrup, N. B. Manson, and L. C. L. Hollenberg. Theory of the ground-state spin of the nv- center in diamond. *Phys. Rev. B*, 85(20):205203, May 2012.

[39] S. Felton, A. M. Edmonds, M. E. Newton, P. M. Martineau, D. Fisher, D. J. Twitchen, and J. M. Baker. Hyperfine interaction in the ground state of the negatively charged nitrogen vacancy center in diamond. *Phys. Rev. B*, 79(7):075203, February 2009.

[40] X.-F. He, N. B. Manson, and P. T. H. Fisk. Paramagnetic resonance of photoexcited n-v defects in diamond. ii. hyperfine interaction with the ^{14}n nucleus. *Phys. Rev. B*, 47(14):8816–8822, April 1993.

[41] J. H. Shim et al., in preparation.

[42] B. Smeltzer, L. Childress, and A. Gali. ^{13}c hyperfine interactions in the nitrogen-vacancy centre in diamond. *New Journal of Physics*, 13(2):025021, 2011.

[43] A. Dréau, J.-R. Maze, M. Lesik, J.-F. Roch, and V. Jacques. High-resolution spectroscopy of single nv defects coupled with

nearby ^{13}c nuclear spins in diamond. *Phys. Rev. B*, 85(13):134107, April 2012.

[44] Prof. Dr. F. Schwabl. *Quantenmechanik (QM 1) Eine Einführung*. Springer, 2007.

[45] C. P. Poole and H. A. Farach. *The Theory of Magnetic Resonance.* Wiley-Interscience, 1972.

[46] J. A. Ferretti and R. R. Ernst. Interference effects in nmr correlation spectroscopy of coupled spin systems. *J. Chem. Phys.*, 65(10):4283–4293, November 1976.

[47] I. Burghardt, J.-M. Bohlen, and G. Bodenhausen. Broadband multiple-quantum nuclear magnetic resonance with frequency-modulated "chirp" pulses: Applications to pairs of scalar-coupled spin i=1/2 nuclei. *J. Chem. Phys.*, 93(11):7687–7697, December 1990.

[48] G. Jeschke and A. Schweiger. Time-domain chirp electron nuclear double resonance spectroscopy in one and two dimensions. *J. Chem. Phys.*, 103(19):8329–8337, November 1995.

[49] N. Bar-Gill, L. M. Pham, A. Jarmola, D. Budker, and R. L. Walsworth. Solid-state electronic spin coherence time approaching one second. *arXiv:1211.7094*, 2012.

[50] A. Schweiger and G. Jeschke. *Principles of Pulse Electron Paramagnetic Resonance*. Oxford University Press, 2001.

[51] D. A. Redman, S. Brown, R. H. Sands, and S. C. Rand. Spin dynamics and electronic states of n-v centers in diamond by epr and four-wave-mixing spectroscopy. *Phys. Rev. Lett.*, 67(24):3420–3423, December 1991.

[52] C. P. Poole and H. A. Farach. *Relaxation in Magnetic Resonance*. Academic Press Inc, 1971.

[53] G. de Lange, Z. H. Wang, D. Ristè, V. V. Dobrovitski, and R. Hanson. Universal dynamical decoupling of a single solid-state spin from a spin bath. *Science*, 330(6000):60–63, 2010.

[54] T. Gaebel, M. Domhan, I. Popa, C. Wittmann, P. Neumann, F. Jelezko, J. R. Rabeau, N. Stavrias, A. D. Greentree, S. Prawer, J. Meijer, J. Twamley, P. R. Hemmer, and J. Wrachtrup. Room-temperature coherent coupling of single spins in diamond. *Nat. Phys.*, 2(6):408–413, June 2006.

[55] G. Balasubramanian, P. Neumann, D. Twitchen, M. Markham, R. Kolesov, N. Mizuochi, J. Isoya, J. Achard, J. Beck, J. Tissler,

V. Jacques, P. R. Hemmer, F. Jelezko, and J. Wrachtrup. Ultralong spin coherence time in isotopically engineered diamond. *Nat. Mater.*, 8(5):383–387, May 2009.

[56] W. Yang and R.-B. Liu. Quantum many-body theory of qubit decoherence in a finite-size spin bath. *Phys. Rev. B*, 78(8):085315, August 2008.

[57] J. R. Maze, J. M. Taylor, and M. D. Lukin. Electron spin decoherence of single nitrogen-vacancy defects in diamond. *Phys. Rev. B*, 78(9):094303, September 2008.

[58] T. D. Ladd, F. Jelezko, R. Laflamme, Y. Nakamura, C. Monroe, and J. L. OBrien. Quantum computers. *Nature*, 464(7285):45–53, March 2010.

[59] A. M. Tyryshkin, S. Tojo, J. J. L. Morton, H. Riemann, N. V. Abrosimov, P. Becker, H.-J. Pohl, T. Schenkel, M. L. W. Thewalt, K. M. Itoh, and S. A. Lyon. Electron spin coherence exceeding seconds in high-purity silicon. *Nat. Mater.*, 11:143–147, 2012.

[60] J. Du, X. Rong, N. Zhao, Y. Wang, J. Yang, and R. B. Liu. Preserving electron spin coherence in solids by optimal dynamical decoupling. *Nature*, 461(7268):1265–1268, October 2009.

[61] M. J. Biercuk, H. Uys, A. P. Van Devender, N. Shiga, W. M. Itano, and J. J. Bollinger. Optimized dynamical decoupling in a model quantum memory. *Nature*, 458(7241):996–1000, April 2009.

[62] J. Bylander, S. Gustavsson, F. Yan, F. Yoshihara, K. Harrabi, G. Fitch, D. G. Cory, Y. Nakamura, J.-S. Tsai, and W. D. Oliver. Noise spectroscopy through dynamical decoupling with a superconducting flux qubit. *Nat. Phys.*, 7(7):565–570, July 2011.

[63] N. Bar-Gill, L. M. Pham, C. Belthangady, D. Le Sage, P. Cappellaro, M. D. Lukin, A. Yacoby, and R. Walsworth. Spectroscopy of composite solid-state spin environments for improved metrology with spin ensembles. *arXiv:1112.0667*, 2012.

[64] G. A. Álvarez, A. Ajoy, X. Peng, and D. Suter. Performance comparison of dynamical decoupling sequences for a qubit in a rapidly fluctuating spin bath. *Phys. Rev. A*, 82(4):042306, October 2010.

[65] G. de Lange, D. Ristè, V. V. Dobrovitski, and R. Hanson. Single-spin magnetometry with multipulse sensing sequences. *Phys. Rev. Lett.*, 106(8):080802, February 2011.

[66] R. Hanson, V. V. Dobrovitski, A. E. Feiguin, O. Gywat, and D. D. Awschalom. Coherent dynamics of a single spin interacting with an adjustable spin bath. *Science*, 320(5874):352–355, April 2008.

[67] E. L. Hahn. Spin echoes. *Phys. Rev.*, 80(4):580–594, November 1950.

[68] H. Y. Carr and E. M. Purcell. Effects of diffusion on free precession in nuclear magnetic resonance experiments. *Phys. Rev.*, 94:630, 1954.

[69] S. Meiboom and D. Gill. Modified spin-echo method for measuring nuclear relaxation times. *Rev. Sci. Instrum.*, 29(8):688–691, August 1958.

[70] T. Gullion, D. B. Baker, and M. S. Conradi. New, compensated carr-purcell sequences. *J. Magn. Reson. (1969)*, 89(3):479–484, October 1990.

[71] A. M. Souza, G. A. Álvarez, and D. Suter. Robust dynamical decoupling for quantum computing and quantum memory. *Phys. Rev. Lett.*, 106(24):240501, June 2011.

[72] C. A. Ryan, J. S. Hodges, and D. G. Cory. Robust decoupling techniques to extend quantum coherence in diamond. *Phys. Rev. Lett.*, 105(20):200402, November 2010.

[73] S. W. Hell and J. Wichmann. Breaking the diffraction resolution limit by stimulated emission: stimulated-emission-depletion fluorescence microscopy. *Opt. Lett.*, 19(11):780–782, June 1994.

[74] E. Rittweger, K. Y. Han, S. E. Irvine, C. Eggeling, and S. W. Hell. Sted microscopy reveals crystal colour centres with nanometric resolution. *Nat. Photon.*, 3(3):144–147, March 2009.

[75] R. Hanbury Brown and R. Q. Twiss. A test of a new type of stellar interferometer on sirius. *Nature*, 178(4541):1046–1048, November 1956.

[76] C. C. Gerry and P. L. Knight. *Introductory Quantum Optics*. Cambridge University Press, 2005.

[77] C. Kurtsiefer, S. Mayer, P. Zarda, and H. Weinfurter. Stable solid-state source of single photons. *Phys. Rev. Lett.*, 85(2):290–293, July 2000.

[78] D. Meschede. *Gerthsen Physik*. Springer, 23 edition, 2005.

[79] N. Mizuochi, P. Neumann, F. Rempp, J. Beck, V. Jacques, P. Siyushev, K. Nakamura, D. J. Twitchen, H. Watanabe, S. Yamasaki, F. Jelezko, and J. Wrachtrup. Coherence of single spins coupled to a nuclear spin bath of varying density. *Phys. Rev. B*, 80(4):041201, July 2009.

[80] A. Dréau, M. Lesik, L. Rondin, P. Spinicelli, O. Arcizet, J.-F. Roch, and V. Jacques. Avoiding power broadening in optically detected magnetic resonance of single nv defects for enhanced dc magnetic field sensitivity. *Phys. Rev. B*, 84(19):195204, November 2011.

[81] N. F. Ramsey. A molecular beam resonance method with separated oscillating fields. *Phys. Rev.*, 78(6):695–699, June 1950.

[82] D. Vion, A. Aassime, A. Cottet, P. Joyez, H. Pothier, C. Urbina, D. Esteve, and M.H. Devoret. Rabi oscillations, ramsey fringes and spin echoes in an electrical circuit. *Fortschr. Phys.*, 51(4-5):462–468, May 2003.

[83] G. D. Fuchs, V. V. Dobrovitski, D. M. Toyli, F. J. Heremans, and D. D. Awschalom. Gigahertz dynamics of a strongly driven single quantum spin. *Science*, 326(5959):1520–1522, December 2009.

[84] A. Messiah. *Quantum Mechanics*. North-Hooland Publishing Company, Amsterdam, 1970.

[85] A. Doll, S. Pribitzer, R. Tschaggelar, and G. Jeschke. Adiabatic and fast passage ultra-wideband inversion in pulsed epr. *J. Magn. Reson.*, 230(0):27–39, May 2013.

[86] J.-M. Cai, F. Jelezko, M. B. Plenio, and A. Retzker. Robust dynamical decoupling with concatenated continuous driving. *arXiv:1111.0930*, 2011.

[87] B. Naydenov, F. Dolde, L. T. Hall, C. Shin, H. Fedder, L. C. L. Hollenberg, F. Jelezko, and J. Wrachtrup. Dynamical decoupling of a single-electron spin at room temperature. *Phys. Rev. B*, 83(8):081201, February 2011.

[88] L. Childress, M. V. Gurudev Dutt, J. M. Taylor, A. S. Zibrov, F. Jelezko, J. Wrachtrup, P. R. Hemmer, and M. D. Lukin. Coherent dynamics of coupled electron and nuclear spin qubits in diamond. *Science*, 314(5797):281–285, October 2006.

[89] A. A. Maudsley. Modified carr-purcell-meiboom-gill sequence for nmr fourier imaging applications. *J. Magn. Reson. (1969)*, 69(3):488–491, 1986.

[90] L. Viola and E. Knill. Robust dynamical decoupling of quantum systems with bounded controls. *Phys. Rev. Lett.*, 90(3):037901, January 2003.

[91] K. Khodjasteh and D. A. Lidar. Fault-tolerant quantum dynamical decoupling. *Phys. Rev. Lett.*, 95(18):180501–4, 2005.

[92] H. M. Cho, R. Tycko, A. Pines, and J. Guckenheimer. Iterative maps for bistable excitation of two-level systems. *Phys. Rev. Lett.*, 56(18):1905–1908, May 1986.

[93] R. Sousa. Electron spin as a spectrometer of nuclear-spin noise and other fluctuations. In Marco Fanciulli, editor, *Topics in Applied Physics*, volume 115, pages 183–220. Springer Berlin Heidelberg, 2009.

[94] N. Zhao, Z.-Y. Wang, and R.-B. Liu. Anomalous decoherence effect in a quantum bath. *Phys. Rev. Lett.*, 106(21):217205, May 2011.

[95] P. Huang, X. Kong, N. Zhao, F. Shi, P. Wang, X. Rong, R.-B. Liu, and J. Du. Observation of an anomalous decoherence effect in a quantum bath at room temperature. *Nat. Commun.*, 2:570, December 2011.

[96] L. G. Rowan, E. L. Hahn, and W. B. Mims. Electron-spin-echo envelope modulation. *Phys. Rev.*, 137(1A):A61–A71, January 1965.

[97] Y. Deligiannakis, M. Louloudi, and N. Hadjiliadis. Electron spin echo envelope modulation (eseem) spectroscopy as a tool to investigate the coordination environment of metal centers. *Coord. Chem. Rev.*, 204(1):1–112, July 2000.

[98] E. Van Oort and M. Glasbeek. Optically detected low field electron spin echo envelope modulations of fluorescent n-v centers in diamond. *Chem. Phys.*, 143(1):131–140, May 1990.

[99] J. S. Hodges, J. C. Yang, C. Ramanathan, and D. G. Cory. Universal control of nuclear spins via anisotropic hyperfine interactions. *Phys. Rev. A*, 78(1):010303, July 2008.

[100] Y. Zhang, C. A. Ryan, R. Laflamme, and J. Baugh. Coherent control of two nuclear spins using the anisotropic hyperfine interaction. *Phys. Rev. Lett.*, 107(17):170503, October 2011.

[101] C. P. Slichter. *Principles of Magnetic Resonance*. Springer, 1996.

[102] N. Khaneja, T. Reiss, C. Kehlet, T. Schulte-Herbrüggen, and S. J. Glaser. Optimal control of coupled spin dynamics: design of nmr pulse sequences by gradient ascent algorithms. *J. Magn. Reson.*, 172(2):296–305, February 2005.

[103] I. I. Maximov, Z. Tosner, and N. C. Nielsen. Optimal control design of nmr and dynamic nuclear polarization experiments using monotonically convergent algorithms. *J. Chem. Phys.*, 128(18):184505–14, May 2008.

SUMMARY

In this thesis we have shown an experimental technique which we have introduced to the NV-center community. This approach allows the excitation of spins in a broad frequency bandwidth without the need of high excitation power. We demonstrated the usefulness of this approach by applying it to a single NV-center which was coupled to a nearest neighbor ^{13}C. Our measurements showed that the current assumptions regarding the hyperfine tensor of this ^{13}C are not sufficient to explain the obtained spectra. As an example we compared the spectra of a manually optimized Hamiltonian to the experimental spectra which indicated that at least pseudo-secular and non-secular hyperfine components have to be taken into account additionally. We have demonstrated the chirped Ramsey technique on the example of single electron spins in the diamond NV-center, but the same approach should also be applicable to other systems, where the excitation bandwidth can be sufficiently large.

The survival time of quantum information in a quantum register is a crucial issue. The coherence time of quantum information can be extended by application of dynamical decoupling sequences. We applied the CPMG DD sequence to the single quantum transition of a single NV electron spin in natural abundance diamond and yielded a T_2 relaxation time of up to 2.2 ms which is close the T_1 limit of $\approx$ 4 ms. Additionally, we have examined the robustness of several dynamical decoupling sequences with respect to pulse imperfections and their performance with respect to arbitrary spin states. We found that the recently introduced DD sequence, KDD, is remarkably robust and performs well for arbitrary spin states. It is much less susceptible to experimental uncertainties, such as flip-angle errors and frequency offsets, than the simpler sequences CPMG and XY-4. We expect that the KDD sequence will be used for many other purposes requiring long coherence time, such as ac-magnetometry or to increase the lifetime of multipartite systems, including entangled states.

We also examined the performance of CPMG sequence on the double quantum coherence of a single NV-center in a natural abundance diamond of type-IIa. A theoretical analysis predicted [94] that the coherence time of the DQC can be longer than for the SQC which was called *anomalous decoherence effect* and was experimentally verified [95]. However, our measurements, which were also performed on a single NV-center, did not show the anomalous decoherence effect. This discrepancy could arise from the simultaneous excitation of all three electron spin transitions by the microwave pulses in our experiment. Nonetheless the obtained relaxation of the double quantum

coherence showed the same behavior as of the single quantum coherence. Both increased linearly with increasing number of refocusing pulses and converged to the T_1 limit.

We presented measurements of the Hahn-echo sequence where we observed electron spin echo envelope modulations (ESEEM). The modulation frequencies showed relations to the hyperfine coupling strength of adjacent ^{13}C's, which were obtained from the corresponding Ramsey spectra. We examined the ESEEM signal by applying CPMG sequences with increasing number of refocusing pulses to the NV-centers and obtained modulations which showed a series of equidistant frequency peaks. The frequency of the main peak was inversely proportional and the modulation depth linearly proportional to the number of pulses. Further investigations e.g. for different orientations and strengths of the external magnetic field might help to clarify the shape of the ESEEM spectra. Hereby ESEEM could become a useful tool to precisely determine the hyperfine interaction between a NV electron spin and an adjacent ^{13}C nuclear spin.

In the last chapter of this thesis we have analyzed the controllability of the ^{14}N nuclear spin of the NV-center via its electron spin. We expect that the NV-nuclear spin can be of great importance in quantum processor architectures based on NV-centers. Thus the nuclear spin can be used e.g. as a cache for the quantum state of NV the electron spin. Controlling the nuclear spin via the electron spin does not require any additional technological equipment and the spin dynamics takes place on the time scale of the inverse of the hyperfine coupling which is in the order of ≈ 2 MHz. We have demonstrated that in a magnetic field, which is tilted with respect to the NV-center symmetry axis, its nuclear spin can be controlled by its electron spin. We performed numerical simulations, which were aimed to polarize the nuclear spin. With the parameters used in the presented simulations a partial polarization of the nuclear spin was achieved on a time scale of 2 μs. Our simulations showed that for higher field strengths the performance increases and we yielded a polarization on a shorter time scale. The usage of more sophisticated algorithms from optimal control theory like GRAPE or KROTOV [102, 103] could probably generate faster and more powerful SMPs. With these algorithms implementations of arbitrary control operations would be feasible.

LIST OF PUBLICATIONS

1. R. Narkowicz, D. Suter, and I. Niemeyer. Scaling of sensitivity and efficiency in planar microresonators for electron spin resonance. *Rev. Sci. Instrum.*, 79(8):084702–8, August 2008.

2. J. H. Shim, I. Niemeyer, J. Zhang, and D. Suter. Robust dynamical decoupling for arbitrary quantum states of a single nv center in diamond. *EPL (Europhysics Letters)*, 99(4):40004, 2012.

3. J. H. Shim, I. Niemeyer, J. Zhang, and D. Suter. Room-temperature high-speed nuclear-spin quantum memory in diamond. *Phys. Rev. A*, 87(1):012301, January 2013.

4. I. Niemeyer, J. H. Shim, J. Zhang, D. Suter, T. Taniguchi, T. Teraji, H. Abe, S. Onoda, T. Yamamoto, T. Ohshima, J. Isoya, and F. Jelezko. Broadband excitation by chirped pulses: application to single electron spins in diamond. New Journal of Physics, 15(3):033027, 2013.

5. J. Zhang, J. H. Shim, I. Niemeyer, T. Taniguchi, T. Teraji, H. Abe, S. Onoda, T. Yamamoto, T. Ohshima, J. Isoya, and D. Suter. Experimental implementation of assisted quantum adiabatic passage in a single spin. *arxiv.org*, 2013.

ACKNOWLEDGMENTS

Ich bedanke mich/ I want to thank:

- bei meinem Doktorvater Prof. Dr. Dieter Suter. Für die Möglichkeit an diesem spannenden Projekt mitgewirkt haben zu können. Ich bedanke mich für die vielfältigen Erfahrungen, die ich in den Bereichen der Programmierung, Konstruktion, Elektronik, Optik, Magnetischen Resonanz und Quanten-Mechanik sammeln konnte und für die Antworten auf unzählige meiner Fragen.
- bei Prof. Dr. Fedor Jelezko für die Unterstützung beim Aufbau des Experimentes, die Diamantproben und die überaus interessanten und spannenden Projekttreffen.
- Prof. Dr. Junichi Isoya for the ^{12}C enriched diamond sample.
- in gleichen Maße bei meinen Freunden und Kollegen: Dr. Marko Lovric, Mirjam Holbach, Dr. Wieland Worthoff, Dr. Rysard Narcovic und Dr. Andre Nowaczyk für die Momente, in denen wir diskutiert, gegrübelt, geflucht und gelacht haben und natürlich für die vielen Kaffeepausen. Ich bedanke mich für die Möglichkeit von und mit euch gelernt zu haben!
- Dr. Jeong Hyun Shim for the strong collaboration, for all the discussions and the coffee-breaks. I am thankful for the chance to have learned from and with you!
- in gleichem Maße bei Dr. Ingo Steiner, Sebastian Schulz, Andreas Schacht und Dennis Kaiser für die vielfältigen Unternehmungen, Partys, den Spaß und die vielen Zerstreuungsmöglichkeiten.
- bei allen Kollegen und Angestellten des Lehrstuhls Exp. Physik 3A für die Unterstützung und freundschaftliche Atmosphäre. Insbesondere bedanke ich mich hierbei bei: Dr. Reiner Küchler für die vielen Gelegenheiten, mein Wissen im Bereich der analogen Elektronik zu erweitern und zu vertiefen und bei Frau Sommer, ohne deren freundliches und ruhiges Gemüt die Bestellung von so manchem Gerät aufgrund der sich immer wieder ändernden Verwaltungsrichtlinien vermutlich im einem Desaster geendet hätte.
- bei Anja Sapsford, Walerian Goralczyk und Horst Rombeck bedanke ich mich für die Bewältigung technischer Probleme, für die Gespräche, die Instandhaltung so machen Gerätes und die

Gelegenheiten eines netten Beisammenseins, z.B. durch die Ausrichtung der Osterfrühstücke (dieser Dank geht auch an Frau Sommer).

- bei allen Mitarbeitern der Werkstätten des Fachbereiches Physik. Hierbei bedanke mich insbesondere bei Frau Susanne Kralemann, Mirko Schier und Norbert Koch für die intensive und erfolgreiche Zusammenarbeit, durch die viele mechanische und elektronische Komponenten für meinen Versuchsaufbau entstanden sind und ich viel gelernt habe. Ebenso geht mein Dank an die Mitarbeiter und besonders an Herrn Klaus Rudloff aus dem Konstruktionsbüro, für die viele mechanische Komponenten, die für meinen Aufbau entworfen wurden.

Ganz besonders möchte ich mich bei meiner Familie bedanken:

- bei meiner Mutter, Annette Honsel, für die jahrelange finanzielle Unterstützung, Beratung in allen Lebenslagen und frühe Unterstützung und Förderung meiner Interessen.
- bei meinem Vater, Heinrich Niemeyer, für die Möglichkeit auf einem landwirtschaftlichen Betrieb aufgewachsen zu sein und praktische Lebenserfahrungen neben dem Hochschulleben gesammelt zu haben.
- bei meinem Bruder, Frederik Niemeyer, für die kostenfreien Trainingsstunden.
- bei meinem Onkel, Dr. Bert Honsel, für die Unterstützung in juristischen Fragen.
- bei meinen Großeltern, die mich während meines Studiums unterstützt habe.
- und ganz besonders bei bei meiner Freundin, Hanja Schmidt, für ihre Geduld, Unterstützung, Liebe, ihren Optimismus und die Zerstreuungsmöglichkeiten und eine alternative Sichtweise. Ich liebe dich!